Remote Sensing Observations of Seismotectonics

Marcello de Michele

THESE DE DOCTORAT DE

L'UNIVERSITE PIERRE ET MARIE CURIE

Geosciénces et Ressources Naturelles (Ecole Doctorale 398)

Présentée par

Marcello de Michele

Pour obtenir le grade de

DOCTEUR de l'UNIVERSITÉ PIERRE ET MARIE CURIE

Sujet de la thèse:

Remote Sensing Observations of Seismotectonics

soutenue le 08 novembre 2010 devant le jury composé de :

Directeur de thèse: M. Pierre Briole, Directeur de Recherche, CNRS, Paris, France

Rapporteurs: M. Rémi Michel, Chercheur, Commissariat à l'Energie Atomique et aux Energies Alternatives -Siège-Saclay, France
M. Nicola D'Agostino, Chercheur, INGV, Rome, Italie

Examinateurs: M. Bertrand Meyer, Professeur, UPMC, Paris, France
M. Raucoules Daniel,Chercheur, BRGM, Orléans, France
Mme Frederique Rolandone, Maître de Conference, UPMC, Paris, France
M. Aochi Hideo, Chercheur, BRGM, Orléans, France

Université Pierre & Marie Curie - Paris 6
Bureau d'accueil, inscription des doctorants
Esc G, 2ème étage
15 rue de l'école de médecine

75270-PARIS CEDEX 06 Tél. Secrétariat : 01 44 27 28 10
Fax : 01 44 27 23 95
Tél. pour les étudiants de A à EL : 01 44 27 28 07
Tél. pour les étudiants de EM à MON : 01 44 27 28 05
Tél. pour les étudiants de MOO à Z : 01 44 27 28 02
E-mail : scolarite.doctorat@upmc.fr

Las ideas no se matan

Ce travail et le parcours qui est derrière, n'aurait pas pu être réalisé sans la contribution physique et spirituelle de nombreuses personnes, qui directement ou indirectement, ont stimulé ma curiosité scientifique et m'ont encouragé dans la démanche.

Je devrais commencer ce paragraphe en remerciant Bruno Messiga, Maria-Pia Riccardi, Fiorenzo Mazzi, Ugo Zezza, Benito Galbiati et le profresseur Vanossi, les professeurs de pétrographie, minéralogie, géologie et géologie structurale à l'Université de Pavia, en Italie ; ensuite, je devrais continuer en remerciant le Docteur Liu et Philippa Mason de l'équipe de télédétection spatiale à l'Imperial College London, où j'ai fait mon (deuxième !) master en 2001/2002. Mais tout cela remonte à avant le Doctorat et donc risque d'être anachronique.

Donc, je souhaiterais d'abord remercier Pierre Briole, qui avant d'être mon directeur de thèse à l'ENS m'a accueilli, fin 2002 –sans vraiment me connaitre- dans le laboratoire de Sismologie de l'IPGP comme ingénieur CNRS. Je suis très reconnaissant envers Antonio Avallone, qui, dans ce même labo, m'a montré des franges ! Antonio m'a appris à utiliser DIAPASON pour construire mes premiers interférogrammes. Nicolas Houlié et Anne-Sophie Boris se sont occupés de moi et de mon séjour à Paris de 2002 à 2004 (merci !). Dans cette période, de nombreuses discussions avec Remi Michel et Helen Vadon entre l'IPGP et le CNES m'ont permis d'approfondir mes connaissances sur la corrélation d'images optiques et ses applications.

Je tiens à remercier Alessandro Ferretti et toute l'équipe de TRE (Telerilevamento Europa) pour l'accueil chaleureux dans leur bureau de Milan et de m'avoir donné la possibilité d'utiliser leur matériel (secret !) pour mieux me former en InSAR pendant quelques mois entre 2004 et 2005. Tout cela m'a motivé à continuer.

Je tiens à remercier toute l'équipe du BRGM, en particulier Claudie Carnec, Hideo Aochi et mon co-auteur préféré Daniel Raucoules qui ont fortement contribué et encouragé les études de recherche et développement en InSAR et en corrélation

d’images optiques et radar au sein du BRGM. Dans ce contexte, je tiens à remercier Charles Werner et Urs Wegmueller pour la semaine passée à Gümligen en formation sur les outils GAMMA et leurs encouragements à poursuivre mes études.

Je souhaite remercier le laboratoire de Géologie de l’Ecole Normale Supérieure de Paris, en particulier Manuel Pubellier, Julia de Sigoyer, Nicolas Chamot-Rooke et Alexandra Robert avec qui j’ai eu l’honneur et le plaisir de travailler au labo et sur le terrain dans le Longmen Shan. Je tiens aussi à remercier Frédérique Rolandone, dont la contribution à l’encadrement de ma thèse notamment sur les études liées à la faille de San Andreas a été très appréciée.

Me remerciements vont en fin à ma famille et, en particulier, à ma compagne Carole qui m’ont encouragé et soutenu tout le long de mon parcours.

Abstract

In the last 20 years, the knowledge of how the Earth deforms has been completely modified by the introduction of two new space techniques. On the one hand, point positioning not only from GPS (Global Positioning System) but also from other systems such as DORIS (Doppler Orbitography and Radio-positioning Integrated from Space). On the other hand, we find space-borne imagery and correlation of images both from multi-interferogram SAR (Synthetic Aperture Radar) techniques and high resolution optical imagery. Those new techniques have allowed to provide a number of scientific advances in terms of confirmation and improvement of the theory of plate tectonics, in terms of better mapping of both the seismic/aseismic displacement fields and the deformation distribution pattern at the plate boundaries, in terms of acquiring more data for the understanding of the post-seismic relaxation, in terms of detect the existence of silent earthquakes and detect pre-seismic signals. At present time, several key questions remain unanswered, such as how much deformation is accommodated by earthquakes at the plate boundaries in comparison to the total amount of strain; how much deformation is accommodated by seismic deformation or by silent creep on discontinuities; whether or not it is possible to detect pre-seismic changes before earthquakes and whether we can propose models for the earthquake precursors. In the present Ph.D. thesis we tried to investigate the potential, limitations, and complementarities of Earth Observation data in the quest for addressing some of the above scientific questions. We concentrate in a limited number of areas of interest such as Bam (Iran), Parkfield (USA) and the Longmen Shan (China). Data processing is mainly based on L-C band Interferometric Synthetic Aperture Radar, subpixel correlation of radar amplitude images and sub-pixel correlation of High Resolution Visible (HRV) satellite images such as Quickbird and Spot-5 data. Our research try to involve the development of innovative approaches to data processing (such as sub-pixel correlation of air-photos and HRV Quickbird images); we focus particularly on the modelling and removal of topographic component to the range sub-pixel offset field and we investigate the ionospheric contribution to the interferometric phase on L-

Band SAR data. In conclusion, our work mainly focuses on two domains. On the one hand, we focus on scientific advances in terms of new approach for data processing and methodological developments. On the other hand, we focus on scientific advances in terms of understanding of neotectonic processes: the surface deformation/ displacement field, accommodation and strain partitioning during the interseismic and co-seismic phase of the earthquake cycle on major faults at plate boundaries (i. e. San Andreas Fault) or intra-plate (e. g. the Longmen Shan). Even though I am formally a Ph.D. student at the Ecole Doctorale at the Université Pierre et Marie Curie de Paris since January 2009, I consider this Ph.D. Thesis as the results of a path that I started earlier. Here, I resume the researches in remote sensing applied to seismotectonics that I, as part of a team, carried out since 2003. Each chapter of this manuscript is a dedicated study. Each study represents a paper that has either been published or is under consideration for publication or has been presented at a conference during the thesis work.

Resumé

Pendant les 20 dernières années, notre connaissance de la déformation de la Terre a été complètement bouleversée par l'introduction de deux techniques de Géodésie spatiale. D'une part, ce que l'on appelle positionnement satellitaire ('point positioning') pas seulement à partir du système GPS (Global Positioning System) mais également à partir du système DORIS (Doppler Orbitography and Radio-positioning Integrated from Space). D'autre part, ont été développées des techniques d'imagerie satellitaire de corrélation d'images et d'interférométrie SAR (Synthetic Aperture Radar) ainsi que les méthodes de mesures de décalages sur des images panchromatiques à haute résolution spatiale. Ces nouvelles techniques, complémentaires de techniques plus classiques, ont permis une série d'avancées scientifiques notamment la confirmation et l'amélioration de la théorie de la tectonique de plaques, la cartographie fine de déplacements sismiques et asismiques, la cartographie de la distribution de la déformation en marges de plaques, l'amélioration de la compréhension des phénomènes de relaxation post sismiques, la détection de séismes lents et 'silencieux', la détection de signaux précurseurs de séismes ou d'éruptions volcaniques. Actuellement des nombreuses questions clés restent ouvertes. Notamment :

- l'importance relative de la déformation accommodée sismiquement en bords de plaques par rapport à la déformation totale et à la contrainte tectonique ;

- la contribution des séismes à la déformation par rapport au déplacement asismique sur les discontinuités (failles) ;

- la possibilité de proposer des modèles pour les précurseurs des séismes et leur pertinence.

Le but de la présente Thèse de Doctorat, est d'étudier le potentiel, les limitations et la complémentarité des données issues de l'Observation de la Terre pour prendre en compte et essayer de répondre à certains aspects des questions exposées ci-dessus. Nous avons concentré notre travail sur un nombre limité de zones telles que Bam (Iran), Parkfield (USA), et le Longmen Shan (China). Les travaux présentés se basent

sur le Radar à Synthèse d'Ouverture (RSO), les techniques de corrélation d'image radar d'amplitude ainsi que les images panchromatiques à haute résolution du type SPOT-5 ou Quickbird. Dans notre recherche, nous avons essayé de développer des approches techniques originales (comme la corrélation d'images aériennes et Quick-bird), nous avons étudié en particulier la modélisation et la suppression de la composante topographique (non désirée) des correlogrammes issus de l'imagerie optiques et radar et nous nous sommes également concentrés sur la contribution de la ionosphère au signal radar interférométrique en bande L.

Pour résumer, notre travail s'est focalisé sur deux axes ; d'une part, on s'intéresse aux approches techniques originales; de l'autre, nous concentrons nos efforts de recherche sur la compréhension des processus néotectoniques, notamment le champ de déplacement cosismique, la répartition de la déformation pendant la phase intersismique et cosismique du cycle sismique sur failles majeures en bord de plaques (p. e. la faille de San Andreas) ou intra plaque (p. e. le Longmen Shan).

Je suis inscrit à l'Ecole Doctorale de l'Université Pierre et Marie Curie de Paris depuis janvier 2009, mais je considère ce manuscrit de Thèse comme le résultat d'un chemin de travail qui a commencé bien avant. Dans ce manuscrit, je vous présente une synthèse des principaux résultats des recherches que j'ai menées depuis 2003. Chaque chapitre de ce manuscrit représente une étude dédiée et ciblée. Chaque étude a fait l'objet d'une publication scientifique ou a été présentée lors d'un congrès international.

Table of Contents

Chapter 1 ..... *13*

Introduction and background **13**

Context of the Thesis and structure of the manuscript **17**

Methods **21**

Synthetic Aperture Radar Interferometry *21*

Subpixel correlation technique *23*

Chapter 2 ..... *27*

Early detection of eruptive dykes revealed by normalized difference vegetation index (NDVI) on Mt. Etna and Mt. Nyiragongo **27**

Summary *28*

Introduction *28*

Analytical method *30*

Results *31*

Discussion *38*

Acknowledgements *42*

Chapter 3 ..... *43*

Deformation between 1989 and 1997 at Piton de la Fournaise volcano retrieved from correlation of panchromatic airborne images **43**

Summary *44*

Introduction *44*

Eruptive activity on Piton de la Fournaise (1989-1997) *46*

Data *47*

Data processing and accuracy assessment *49*

Quantification of displacement *51*

Mapping lava flows *56*

Discussion and conclusions *56*

Acknowledgements *60*

Chapter 4 ..... *61*

Measuring coseismic deformation on the northern segment of the Bam-Baravat escarpment associated with the 2003 Bam (Iran) earthquake, by correlation of very-high-resolution satellite imagery 61

Summary *62*

Introduction *62*

Data *65*

Methodology *66*

Results *69*

Discussion *72*

Acknowledgments *74*

Chapter 5 ..... *75*

Using InSAR for seismotectonic observations over the Mw 6.3 Parkfield earthquake (29/09/2004), California. 75

Summary *76*

Introduction *76*

InSAR evidence of pre-seismic strain accumulation *77*

InSAR evidences of co-seismic strain release *82*

Discussion and Conclusions *84*

Acknowledgements *85*

Chapter 6 ..... *87*

Spatiotemporal evolution of surface creep in the Parkfield region of the San Andreas Fault (1993-2004) from Synthetic Aperture Radar. 87

Introduction *88*

Methodology *90*

Results and discussion *94*

Conclusions *101*

Acknowledgements *103*

Chapter 7 ..... *105*

The Mw 7.9, 12 May 2008 Sichuan earthquake rupture measured by sub-pixel correlation of ALOS PALSAR amplitude images 105

Summary *106*

Introduction *107*

Data analysis *109*

Results *110*

Discussion and conclusion *111*

Acknowledgement *115*

Chapter 8 ..... *117*

Assessing ionospheric influence on L-band SAR data: Implications on co-seismic displacement measurements of the 2008 Sichuan Earthquake. 117

Summary *118*

Introduction *118*

Ionospheric effects on InSAR data *121*

Azimuth correction *122*

Computation of the phase derivative *127*

Integration of the azimuth correction: the IPS *128*

Discussion *130*

Conclusions *131*

Acknowledgement *132*

Chapter 9 ..... *133*

Three-dimensional surface displacement of the 12 May 2008 Sichuan earthquake (China) derived from Synthetic Aperture Radar: evidence for rupture on a blind thrust. **133**

Summary *134*

Introduction *134*

Methodology *137*

Results *141*

Interpretation and modelling *144*

Discussion and conclusions *146*

Acknowledgements *148*

Chapter 10 ..... *151*

Surface displacement of the Mw 7 Machaze earthquake (Mozambique): Complementary use of 2 multiband InSAR and radar amplitude image correlation with elastic modelling. **151**

Summary *152*

Introduction *153*

Data *154*

Data Processing *156*

Results *159*

Co-seismic deformation modelling *166*

Discussion and Conclusion *169*

Acknowledgements *170*

Chapter 11 ..... *171*

Conclusions and perspectives **171**

Chapter 1

Introduction and background

In the last 20 years, the knowledge of how the Earth deforms has been completely modified by the introduction of two new space techniques:

point positioning, not only from GPS (Global Positioning System) but also from other systems such as DORIS (Doppler Orbitography and Radio-positioning Integrated from Space); imagery, and correlation of images, from space. Both from multi-interferogram SAR (Synthetic Aperture Radar) techniques (in particular the Permanent Scatterers technique developed by Politecnico di Milano) and high resolution optical imagery (e.g. Massonnet et al., 1993; Massonnet et al., 1995; Van Puymbroeck et al., 2000; Ferretti et al., 2001; Miller et al., 2002; Ruegg et al., 2002; Lu et al., 2003; Puglisi et al., 2004; Avallone et al., 2004).

Those new techniques have allowed to:

❶ Confirm and improve the theory of plate tectonics: plate velocities estimated over 2-3 mm/yr from magnetic anomalies at the mid oceanic ridges and focal mechanisms of large earthquakes at the plates boundaries are close to those found over a period of 15 years with GPS. Where discrepancies exist between both determinations, one of the important questions is to determine whether they are due to errors (or lack of accuracy) in one of the two techniques or correspond to plate velocity changes at some boundaries in the last 2-3My. The latter corresponds to areas where relative plate motions are currently changing with time (either accelerating or decelerating).

❷ Better map the deformation distribution pattern at the plate boundaries. Although some plate boundaries (such as subduction areas and strike slip fault areas) often represent relatively sharp discontinuities, spatial deformation over extensive plate boundaries or compressive plate boundaries extends over broad areas. In the last 15

years, GPS has allowed to provide high details on several of those boundaries. In particular, the fastest ones (Basin and Range, Tibet, Greece). On the other hand, slower plate boundaries still need more data and more time for the deformation distribution field to be well mapped (Apennines, Alps, and areas of crustal extension such as the Eastern African Rift system).

❸ Accurately map deformation associated with earthquakes. Here the progresses are mainly coming from differential SAR interferometry (DInSAR). Starting with the Landers earthquake (1992) a number of large earthquakes have been studied with this technique, which is now a commonly used technique to map surface displacements fields. Among the main progresses in the knowledge of coseismic deformation, one of the most important was the first order demonstration that the hypothesis of elasticity of the Earth (deduced by Earth's response to earthquakes) was correct. Displacement field associated with earthquakes, even earthquakes involving the entire lithosphere such as subduction earthquakes, are correctly modeled with rather simple models of dislocation in simple elastic half spaces. Another InSAR advantage is to give one access to surface displacement due smaller earthquake (Mw 5 to 6), previously not accessible because of both the limited density of geodetic networks and the limited accuracy of the measurements on those networks. The capability to image and measure small earthquakes is very important. In this way, much larger number of events can be studied allowing the improvement of earthquake source models, which is of great importance for earthquake hazard assessment and risk mitigation.

❹ Acquire better data of the post-seismic relaxation. It was already known that after an earthquake had occurred, relatively fast relaxation involves the area during the following few years. Several models have been created for explaining this all-involving viscous process in the lower crust and upper mantle. The coming of GPS and InSAR techniques has boosted the studies in this field (e. g. Lu et al., 2001).

❺ Detect the existence of silent earthquakes occurring in several places of the Earth e.g. the Cascades or Mexico.

❻ Detect pre-seismic signals, such as in the case of the South Peru 2001 earthquake e. g. Ruegg et al., 2001).

❼ To start addressing the question of coupled events (triggering of an earthquake by another, triggering of a volcanic eruption by an earthquake, triggering of an earthquake by a volcanic eruption, triggering of eruptions or earthquake by a landslide).

❽ Retrieve the full 3D coseismic displacement field with a high spatial resolution in non-instrumented areas, which in some cases has allowed to address the riddle of the shallow slip deficit (Fialko, 2005), and in others has given evidences of seismic ruptures on blind structures (de Michele et al., 2010, this manuscript).

At present time, several key questions merit attention. Among the others:

How much deformation is accommodated by earthquakes at the plate boundaries in comparison to the total amount of strain? How much deformation is accommodated by seismic deformation in the volume or by silent creep on discontinuities (episodic or continuous creep)? How co-seismic strain is partitioned on faults during large earthquakes? How does surface fault creep evolve in space and time and can we measure its spatio-temporal evolution from space? How do events couple and does vegetation activity reacts to deep Earth phenomenon? Can we improve our knowledge about seismic hazard in a strong lithosphere context such as Mozambique? In general, what are the remote sensing strategies, observations and data processing that allow us to improve the understanding of the seismic cycle? What are the limitations imposed by ionospheric effects on SAR and InSAR data and how can we mitigate them? Can we use the SAR amplitude imagery to assess seismic deformation accomodated on blind structures? Which methodology can we propose to process very-high spatial resolution space-borne/airborne optical imagery to map volcano or earthquake displacement field?

Context of the Thesis and structure of the manuscript

The main objective of this Ph.D. thesis is the investigation of potential, limitations, and complementarities of Earth Observation data in the quest for addressing some of the above scientific questions. We present several key studies where remote sensing techniques have allowed us to:

- increase the resolution of existing co-seismic datasets (Bam, Iran; Sichuan, China);
- provide a rare example of co-seismic and post-seismic displacement field within a very strong lithosphere context (Mozambique);
- provide complementary measurements of interseismic and co-seismic displacement field (Parkfield, USA).

Data processing is based on L-C band Interferometric Synthetic Aperture Radar, sub-pixel correlation of radar amplitude images and sub-pixel correlation of Hight Resolution Visible (HRV) satellite images such as Quickbird and Spot-5 data. Our research try to involve the development of innovative approaches to data processing (such as sub-pixel correlation of air-photos and HRV Quickbird images); we focus particularly on the modeling and removal of topographic component to the range sub-pixel offset field and we investigate the ionospheric contribution to the interferometric phase on L-Band SAR data. The Ph.D. thesis focuses on two domains:

1) Scientific advances in terms of new approach for data processing and methodological developments;

2) Scientific advances in terms of understanding of neotectonic processes: the surface deformation/displacement field, accommodation and strain partitioning during the interseismic and co-seismic phase of the earthquake cycle on major faults at plate boundaries (i. e. San Andreas Fault) or intra-plate (e. g. the Longmen Shan).

Where possible, the remotely sensed observations are validated against ground measurements.

Even though I am formally a Ph.D. student at the Ecole Doctorale at the Université Pierre et Marie Curie de Paris since January 2009, I consider this Ph.D. Thesis as the results of a path that I started earlier. Here, I resume the researches in remote sensing applied to seismotectonics that I, as part of a team, carried out since 2003. Part of this work has matured at the Institut de Physique du Globe de Paris, part of it has originated and benefitted from the scientific environment at the Bureau de Recherches Géologiques et Minières (the French Geological Survey) and the stimulating environment at the Ecole Normale Supérieure de Paris. We concentrated our researches in various geodynamic contexts; we start by putting in evidence a possible relation between vegetation activity and fissure eruptions on Nyiragongo and Etna Volcano. Then we analyze inter-eruption volcano deformation at Piton de la Fournaise volcano by using airborne photos. We then focus on strike-slip geodynamic context during the co-seismic phase of the seismic cycle at Bam (Iran) and during the interseismic phase of the seismic cycle at Parkfield (USA). The Sichuan earthquake occurred in a compressional tectonic regime (even though the exhumation mechanism of the Longmen Shan is still under debate). There, we used SAR data to observe that tectonic stress is oblique to the seismogenic faults (that originated on preexisting structures) so that co-seismic strain is partitioned between thrust displacements and strike-slip displacements, part of which is accommodated on a blind structure at depth. Finally, we study the Machaze earthquake (Mozambique) that occurred in an extensional tectonic regime on what is considered as an embryonic structure belonging to the East African Rifting context.

Each chapter of this manuscript is a dedicated study (presented in chronological order). Each study represents a paper that has either been published or is under consideration for publication or has been presented at a conference during the thesis work:

Chapter 2. Houlié, N., J.C. Komorowski, M. de Michele, M. Kasereka, H. Ciraba, Early detection of eruptive dykes revealed by Normalized Difference Vegetation In-

dex (NDVI) on high-resolution satellite imagery, Earth and Planetary Science Letters, 246, 3-4, 231-240, 10.1016/j.epsl.2006.03.039, 2006.

Chapter 3. de Michele, M., and P. Briole, Deformation between 1989 and 1997 at Piton de la Fournaise volcano retrieved from correlation of panchromatic airborne images, Geophys. J. Int., v. 169(1), pp. 357-364, 2007.

Chapter 4. de Michele, M., Raucoules, D., Aochi, H., Baghdadi, N., Carnec, C., Measuring coseismic deformation on the northern segment of the Bam-Baravat escarpment associated with the 2003 Bam (Iran) earthquake, by correlation of very-high-resolution satellite imagery, Geophysical Journal International, 173, 2, 459–464, 2008.

Chapter 5. de Michele, M., Raucoules, D., Salichon, J., Lemoine, A., Aochi H., Using InSAR for seismotectonic observations over the 6,3 Parkfield earthquake (28/09/2004), California, The International Archives of the Photogrammetry, Remote Sensing and Spatial Information Sciences. Vol. XXXVII. Part B4. Beijing, 2008.

Chapter 6. de Michele, M., Raucoules, D., Rolandone, F., Briole. P., Salichon, J., Lemoine, A., Aochi H., Spatiotemporal evolution of surface creep in the Parkfield region of the San Andreas Fault (1993/2004) from Synthetic Aperture Radar. Manuscript in preparation (2010).

Chapter 7. de Michele, M., Raucoules, D., Lasserre, C., Pathier, E., Klinger, Y., Van Der Woerd, J., de Sigoyer, J., Xu, X., The Mw 7.9, 12 May 2008 Sichuan earthquake rupture measured by sub-pixel correlation of ALOS PALSAR amplitude images, Earth Planets and Space, accepted for publication, 2009.

Chapter 8. Raucoules D., de Michele, M., Assessing ionospheric influence on L-band SAR data: Implications on co-seismic displacement measurements of the 2008 Sichuan Earthquake, IEEE Geoscience and Remote Sensing Letters 7, 2, 286-290, 2010.

Chapter 9. de Michele, M., Raucoules, R., de Sigoyer, J., Pubellier, M., Chamot-Rooke N., Three-dimensional surface displacement of the 12 May 2008 Sichuan earthquake (China) derived from Synthetic Aperture Radar: evidence for rupture on a blind thrust, accepted to Geophysical Journal International, 2010.

Chapter 10. Raucoules, D., Ristori, B., de Michele, M., Briole, P., Surface displacement of the M_w 7 Machaze earthquake (Mozambique): Complementary use of multi-band InSAR and radar amplitude image correlation with elastic modelling, Remote Sensing of Environment / Remote Sensing of the Environment 114, 10, 2211-2218, 2010.

Methods

Synthetic Aperture Radar Interferometry

As a detailed technical review of InSAR concepts exceeds the scope of the present document, we suggest the reader to refer to specialised literature (e. g. Massonnet et al., 1993; Massonnet and Feigl, 1998; Hanssen, 2001; Hooper, 2006, Ferretti et al., 2001) for a technical review of the SAR instrument, systems, SAR interferometry algorithms and image formation concepts. We describe below just the few concepts, mainly borrowed from Hanssen (2001) and Hooper (2006) that would help the non-specialised reader to familiarise with the very basics of SAR and understand the findings described further in this manuscript.

The Radio Detection and Ranging (radar) techniques developed in the first half of the 20th century has evolved into the Synthetic Aperture Radar (SAR) techniques in the mid 70‘s. A SAR system can be seen as an extension of the classical radar systems; it employs both the pulse compression techniques and the synthetic aperture concept that enable the data spatial resolutions to be improved by the order of meters (instead of kilometres) with relatively small physical antennas. Compared to visible remote sensing, the radar has several advantages; it is an active system (so data acquisition does not depend on the daylight); radar waves pass through clouds, which makes the SAR a potentially «all weather» instrument. Space-borne SAR instruments were initially used for the investigation of planetary surfaces with the first Earth orbiting SAR instrument launched in 1978, aboard the NASA (National Aeronautics and Space Administration) SEASAT satellite. The launch of the ESA (European Space Agency) satellite ERS-1 in 1991, led to a large amount of SAR data available for InSAR and made InSAR widely applicable. SAR systems operate with a side-looking geometry and illuminate the Earth with a series of microwave pulses and record the phase and amplitude of echoes of previous pulses, scattered from the Earth. The raw data collected by the SAR is then focused to form an «image» or «scene». Each time the spacecraft passes over a specific area it can acquire a «scene». The data focusing is

achieved in the direction perpendicular to the flight direction (range direction) through knowledge of the time delay, and in the flight direction (azimuth direction) through combination of echoes from multiple locations to synthesise a large antenna aperture (the synthetic aperture concept). Focusing is based on the consideration (the compression process) of the frequency modulation in a given bandwidth both in range and azimuth directions. In range direction, both the bandwidth and the frequency variation that make compression possible are provided by the nature of the emitted pulse (i.e. the design of the instrument) and the frequency is linearly modulated. Whereas in azimuth direction, bandwidth and frequency variation are naturally provided by the Doppler effect associated with the movement of the sensor relative to the Earth.

The basic concept of differential SAR interferometry can be summarised as the phase differences of the radar waves between multiple radar scenes. For our researches, the main objective of SAR interferometry is to estimate the deformation field occurring on the surface of the Earth between two radar acquisitions. Given exactly the same data acquisition geometry (the orbital baselines are supposed to be very small respect to the satellite-earth distance), the phase differences between multiple radar scenes acquired over the same area is proportional to a number of physical phenomena such as ionospheric or tropospheric waves refraction (resulting in signal phase delay), random changes of the earth surface and ground surface movements and noise. In seismotectonics, we are interested in the InSAR signal due to ground surface movements. Therefore, we will try to model the undesired signals and remove them from the interferometric phase, after which we can use the SAR system to create maps and time series of surface displacements. Many algorithms have been proposed as each study area has to be treated as a case-study depending on the geographic area and local atmospheric properties and conditions. We propose some examples developed for our study areas in Chapter 6 and Chapter 8.

Subpixel correlation technique

Image correlation techniques represent a valuable complement to Differential Synthetic Aperture Radar Interferometry (DInSAR) for monitoring Earth surface displacements. In particular, near fault/fracture zones where large displacement results in poorly coherent SAR signal. This technique has been successfully applied using SAR amplitude images and satellite/airborne photos in different fields of study. In particular, in seismotectonics (e. g. Van Puymbroeck *et al.* 2000; Michel & Avouac 1999; Michel & Avouac 2002; Dominguez *et al.* 2003, Binet & Bollinger, 2005; Fialko *et al.* 2005, Klinger *et al.*, 2006; Michel & Avouac, 2006), on volcano deformation (Tobita *et al.* 2001) and gravitational movements assessment (*e.g.* Delacourt *et al*. 2004; Berthier *et al. 2005*). Subpixel correlation technique has also been applied on panchromatic airborne images to quantify volcano deformation (de Michele & Briole, 2007, this document). Image correlation technique relies on the statistical analyses of two sets of data (e.g. digital satellite imagery). This technique matches the 'before event' image and the 'after event' image at each point on a grid analysing the degrees of local correlation at each step. Differences in the local instantaneous frequency of the images result in sub-pixel spatial differences in ground patterns (Crippen, 1992). The results are an expression of both movements in the ground surface and image distortions. Sources of image distortions are discussed in Van Puymbroeck et al. (2000), Michel & Avouac (2006) and Leprince et al. (2007). They can be potentially modelled and removed so that ground surface displacements can be highlighted and measured with high precision. Measurements must be performed with subpixel accuracy, because the amplitude of the ground displacement -a few meters for large earthquakes- is typically lower than the resolution of the images except for new generation HRV sensors with improved spatial resolution and air-photos.

Optical domain

Sub-pixel image correlation technique for measuring ground surface displacements was firstly conceptualised by Robert Crippen (1992) and applied to satellite visible imagery. Crippen (1992) gave the technique the name of "imageodesy". The premise of the method is that extensive, sub-resolution spatial differences in ground patterns between images acquired at differing times can be measured accurately to high precision and also can be distinguished from systematic image differences, such as those due to sensing-system attitude variations. If each pixel value is a measure of radiance weighted at sub-resolution scales by the point-spread function that is imposed by the atmosphere and sensor optics, each pixel value is, therefore, variable in relation to its geographic position at sub-resolution scales and thereby indirectly measures geographic position.

The images should be previously resampled to the DEM geometry so that they are in a common cartographic projection but recently some other methodologies are being proposed if a precise DEM is not available, such as the three pass image correlation (de Michele et al., 2008, this manuscript) and the use of the perpendicular-to-the-epipolar-plane images (Renaud Binet, personal communication). Residual offsets remain that relate to residual uncertainty in estimates of satellite parameters, errors in DEM (if a DEM is used), and deformation induced by earthquakes. Those offsets are characterised by gradients typically lower than 0.1% except within a few tens of meters of faults (Michel & Avouac, 2006). For more technical details on the methodology we suggest the reader to refer to the pioneering work of Van Puymbroek et al., 2000 or Leprince et al., 2007. The latter, within the Californian Institute of Technology, develop and maintains a dedicated software for optical image correlation.

Radar domain

Sub-pixel image correlation technique for measuring ground surface displacements can be applied to SAR amplitude images. The main differences are due to the radar

acquisition geometry so that instead of having East-West and North-South offsets one have Slant range offsets and Azimuth offset. This is in a way intriguing as azimuth offset are «topography free» and slant range offsets are calculated in the Line Of Sight of the satellite and therefore contains a contribution from vertical offsets depending on the viewing angle. For details on this this methodology, also called "offset", we suggest the reader to look at Michel & Rignot (1999) and Michel et al., (1999), who used it with SIR-C (*L*-band; SIR is Shuttle Imaging Radar) and European Remote-Sensing Satellite (ERS) radar amplitude images. The technique of offsets provides a measurement of the ground displacement from the analysis of the geometrical deformation between the two SAR amplitude images. Usually SAR images with a small as possible baseline are chosen in order to reduce the stereoscopic effect and geometric decorrelation. In the studies presented in the present work, we estimate the range and azimuth offset fields using cross correlation optimisation of the input intensity images. This algorithm is implemented in the GAMMA software with the name of «offsets tracking» (Strozzi et al., 2002).

Chapter 2

Early detection of eruptive dykes revealed by normalized difference vegetation index (NDVI) on Mt. Etna and Mt. Nyiragongo

by Nicolas Houlié [a], Jean Christophe Komorowski [b], Marcello de Michele [c], Mahinda Kasereka [d], Matesco Ciraba [d]

[a] University of California – Berkeley Seismological Laboratory 217, Mc Cone Hall, 94720 Berkeley, USA

[b] Equipe de Volcanologie, Institut de Physique du Globe de Paris, CNRS, UMR 7154, 4 Place Jussieu, boite 89, 75252 Paris cedex 05, France

[c] Laboratoire de Sismologie – Institut de Physique du Globe de Paris, CNRS, 4, Place Jussieu, boite 89, 75252 Paris cedex 05, France

[d] Observatoire Volcanologique de Goma (OVG), Goma, Centre de recherches en Sciences Naturelles (CRSN), Democratic Republic of Congo (DRC)

Foreword - This chapter mainly describes the work that Nicolas Houlié and me have performed on the subject of vegetation on volcanoes, and that has been published as Houlié et al., 2006 on *Earth and Planetary Science Letters.* This study has actually been carried out at the *Institute de Physique du Globe de Paris* under a Un-OOCHA project on Nyiragongo volcano, lead by Jean Christophe Komorowski. For this study, I wish to acknowledge the help and the stimulating discussions that we had with Pierre Briole, in particular on the topic of Mount Etna.

Summary

Flank-fissure eruptions involve lateral injection and propagation of magma in a volcanic edifice along pre-existing fractures in the direction of the rift zones where magma intrusion and lava flow production are concentrated over time. Thus, the identification and mapping of active fractures and faults is a fundamental aspect of studies of active volcanic systems. However, gradual dyke wedge emplacement at depth in well-fractured zones on volcano flanks and in volcanic rift zones does not necessarily trigger large amplitude deformation signals susceptible to be recorded months or even years before the actual eruption. Here we show that active and potentially eruptive areas can be detected up to 2 yrs before the arrival to the surface of the final eruptive dyke and venting of lava flows by processing satellite images applying a normalized difference vegetation index (NDVI) algorithm. A posteriori analysis of satellite images indeed reveals that the surficial effects of dyke wedge injection and ascent on plant growth were apparent for Mt. Etna from 2000 to 2002 and for Mt. Nyiragongo in 2001, thus months to years before they erupted.

Introduction

In January 2002, a flank eruption occurred on Nyiragongo stratovolcano (Democratic Republic of Congo -DRC; Fig. 2.3). Detailed studies have shown that a major tectonic reactivation in the Kivu rift area of the western branch of the East African Rift weakened the mecanical strength of Nyiragongo's edifice (3470 m a.s.l) (Tedesco et al., 2002; Allard et al., 2002; Komorowsky et al., 2003; Komorowsky et al., 2004a; Komorowsky et al., 2004b). Lava-emissive fractures developed on the southern flanks of the volcano, parallel to the tectonic structures of the Kivu rift system, and propagated for about 16 km downslope towards the city of Goma. The lava flows partly destroyed the city sending about 300000 people on a sudden exodus in the context of a humanitarian crisis and complex emergency associated to Africa's deadliest armed conflict.

In November 2002, after 1 yr of intense seismic and effusive activity along the southern rift zone, Mt. Etna (Fig. 2.1) erupted and a lava flow propagated along the North East Rift Zone in the Piano Provenzana area. Some dykes were injected along the North East Rift Zone (Branca et al., 2003) and lava flows spread over Piano Provenzana area (Tibaldi and Groppelli, 2003) partially destroying touristic facilities. These flank eruptions occurred along the rift zones of two large and heavily populated effusive volcanoes which are amongst the world's most active. Additional tools to detect, on a longer pre-eruptive time frame the reactivation of volcanic rift zones or portions of such systems will improve

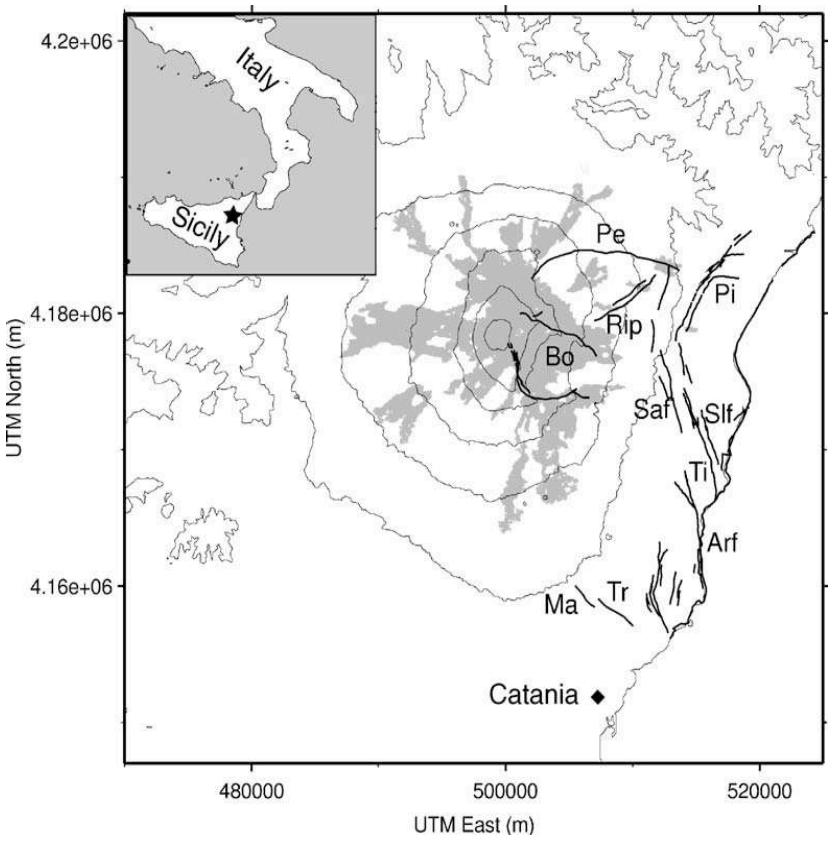

Figure 2.1. Inset: Location of Etna Volcano is marked by a star. The study area: main structures are indicated. MA: Mascalucia fault, TI: Timpe fault system, BO: Valle del Bove, PE: Pernicana–Provenzana fault, Slf: San Leonardello fault, Rip: Ripa della Naca fault

monitoring and eruption forecasts. At Mt. Nyiragongo where an adequate monitoring network was absent prior to the eruption, a posteriori analysis shows that even INSAR remote-sensing data (Poland et al., 2003) did not detect wide-field ground deformation associated with dyke intrusion within the fractured volcanic rift zone months before the eruption. We document for the first time, using remote sensing techniques, the existence of a strong link between preeruptive activity, the growth of vegetation on the volcano's active rift zones, and the location of likely future eruptive activity.

Analytical method

The normalized difference vegetation index (NDVI) is a well-known tool of environmental remote sensing studies to quantify the density and vigor of green vegetation using the spectral reflectivity of solar radiation (e.g. Richardson and Wiegand, 1977). It is calculated as follows:

$$NDVI = \frac{nir - red}{nir + red} \quad (1)$$

It thus provides a standardized method of comparing vegetation greenness between satellite images (Jensen, 2000) and effectively discriminates areas with healthy green vegetation with values close to +1 (0.6–0.9; bright areas in Figs. 2.1 and 2.2) from areas with soil/rocks with values close to zero (dark areas in Figs. 2.1 and 2.2). Green leaves commonly have larger reflectance in the near infrared (NIR) than in the visible range (RED). High NDVI values indicate intense photosynthetic activity of green vegetation.

In this study we used high-resolution multispectral (MS) satellite data acquired by the ASTER (Advanced Spaceborne Thermal Emission and Reflection Radiometer) instrument from the Terra satellite on Mount Etna (Italy) and by the IKONOS sensor on Nyiragongo Volcano (DRC; Fig. 2.3). SpaceImagings IKONOS MS sensor is a high-

resolution instrument that records data in blue, green, red and near-infra-red (NIR) wavelengths with 4-m pixel size. ASTER is an imaging instrument on board the NASAs Terra satellite that measures reflectance and emissivity of the Earth surface with 14 bands covering the visible and near infra-red, short infrared and thermal wavelengths of the electromagnetic spectrum with 15-, 30- and 90-m pixel sizes, respectively.

The process of ortho-rectification requires the satellite camera parameters and its position, an accurate DEM and at least few ground control points (GCPs). In the case of Nyiragongo, there is no high resolution DEM and only the 90 m resolution SRTM data set is available. Moreover, because of security problems and the difficulties of operating GPS equipment in armed conflict areas on the volcano's flank, we could not obtain an adequately balanced distribution of GCPs for a good ortho-rectification. We decided that it was thus better to work on georeferenced raw images using the satellite ancillary data notwithstanding the existence of a strong clear NDVI signal for areas of low topographic relief. An estimate of the geo-position of the 4 corners of each ASTER image is available. IKONOS GEO monoscopic archived level 2 images are geometrically corrected by SpaceImaging and given with a horizontal RMS radial error of 23.3 m and a circular error 0.90 probability of 50 m plus the terrain displacement. Validation that the NDVI features matched exactly the position of the eruptive fractures was easily achieved visually using obvious reference points (lava flows, villages and roads). The NDVI was not stretched with respect to a reference picture in order to reflect the variance of the vegetation growth in the time. All presented ASTER and IKONOS images were processed to produce NDVI images using Eq. (1).

Results

On Etna, we have detected an elevated NDVI signal on ASTER data (Table 2.1) with a width of 60 m (4 pixels), a length of about 3 km and a general NE trend located north of the Pernicana fault (Fig. 2.1) (Azzaro et al., 1998 Azzaro et al., 2001a; Az-

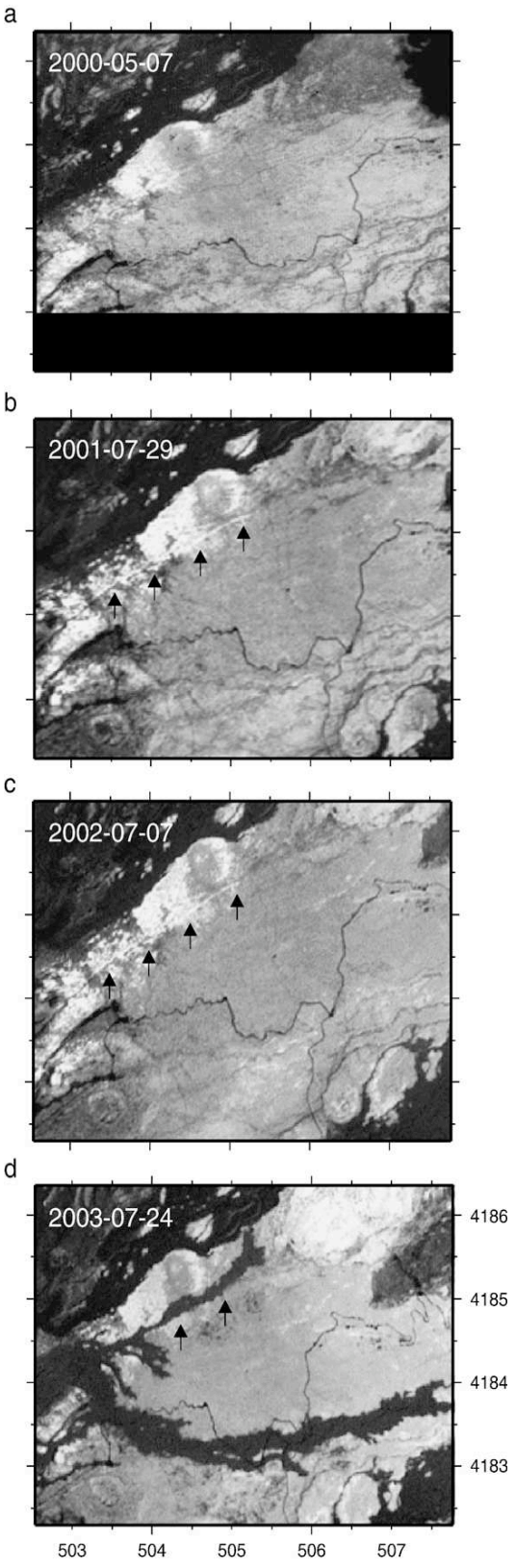

zaro et al., 2001b) in the North East Rift Zone (Fig. 2.2). In this area, an emissive fracture formed during the 2003 eruption to produce the Piano Provenzana lava flow. The NDVI signal is markedly visible for up to 2 yrs before the eruption on images taken in the same season (June to August) in 2002 and 2003 but it is much less visible on images taken in June 2001, 3 yrs before the event. Eruptive fractures several kilometers in length which formed during previous flank-fissure eruptions at Nyiragongo Volcano in 1977 and most likely several hundreds of years ago have been identified in the field (Tazieff, 1977; Komorowsky et al., 2004a).

Figure 2.2 NDVI ASTER images. In pictures a to c were (pixel size=15 m) acquired before the 2002 November eruption, vegetation growth intensity (white pixels) outlines a linear pattern trending E–NE activity on Piano Provenzana (Etna). This trend is similar to the trend of the fracture that produced the March 2003 lava flow. The mean amplitude changes of the NDVI values can be explained by slight variations in photosynthetic activity of the plants over the years.

A new set of emissive fractures was formed over 14 km as a result of the 2002 flank-fissure eruption (Fig. 2.4) (Komorowsky et al., 2004a). On Nyiragongo, we observe on a pre-eruptive 2001 IKONOS satellite image that only the parts of the flank fissure system which became eruptive in 2002 (Fig. 2.5) show an elevated NDVI signal (Figs. 2.6 and 2.7). The spatial amplitude of the Nyiragongo NDVI signal reaches a total width of 20 m (5 pixels) and is thus 3 times smaller than on Etna.

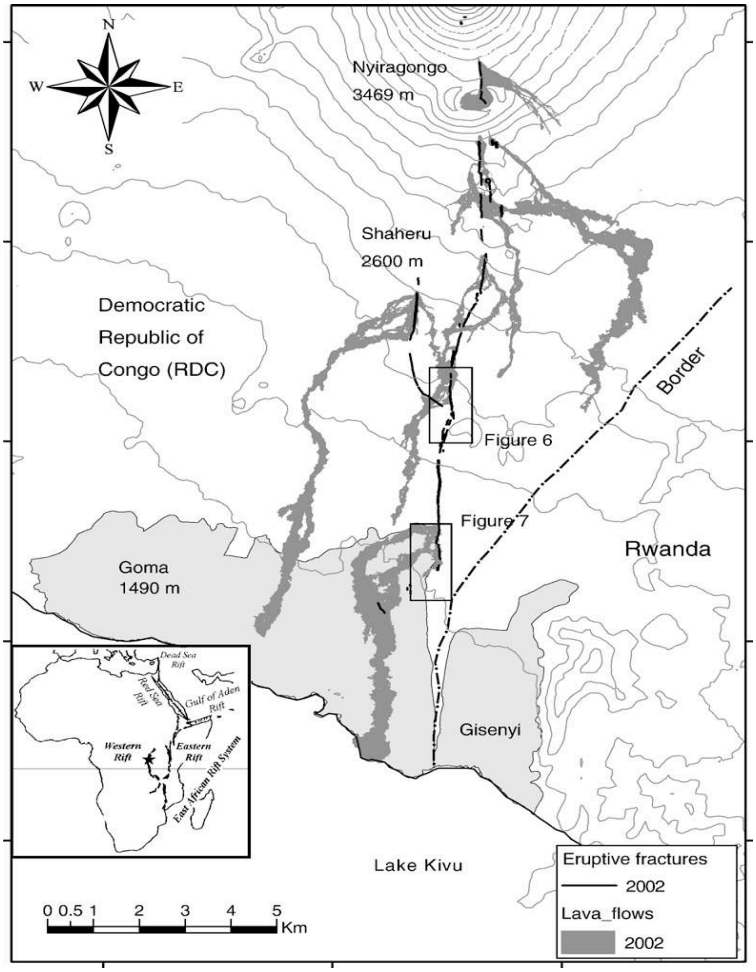

Figure 2.3. Location map of Nyiragongo Volcano (Democratic Republic of Congo) in the western branch of the East African Rift system showing lava flows and fractures formed during the 2002 flank-fissure eruption. The two areas of study are shown by two rectangles related to Figs. 6 and 7. Modified after Komorowsky et al. (2004a).

The main NDVI linear feature (Fig. 2.6) stretches over a length of about 4 km with a N–S trend. Another linear elevated NDVI feature occurs just NE of the Goma city airport stretching over about 1.5 km in a N–S trend and with a width of 5 pixels (Fig. 2.7). In this area also the 2002 eruptive fracture coincides exactly with the NDVI linear feature seen in the 2001 image. Both NDVI linear features form an en echelon system that coincides exactly with the en echelon system of fractures seen in the field which propagated and erupted lava in 2002 (Fig. 2.4).

On Nyiragongo, field observations clearly revealed the absence of any linear topographic features before the 2002 event at the location where lava flows were emitted in 2002 (Komorowsky et al., 2004a). We have tested for the presence of elevated NDVI signals along two other prominent pre-1977 vegetated old eruptive fractures. There is no elevated NDVI signal there. Thus, there is no enhanced vegetation growth within this fracture. However, our analysis has clearly shown that the same vegetation species growing several hundreds of meters east, in an area with no visible pre-eruptive surficial topographic lineament but the same ground typology (pahoehoe lava flow surface), are characterized by a marked elevated NDVI signal. This signal forms the linear feature described above and matches the location where lava emissive fractures propagated in 2002 (Fig. 2.6).

Volcano	Sensor	Date	Pixel size (m)	ID
Etna	ASTER	2000-05-07	15	AST_07_00305072000100910000
Etna	ASTER	2001-07-29	15	0000 AST_07_00307292001100121000
Etna	ASTER	2002-07-07	15	0000 AST_07_00307072002100113000
Etna	ASTER	2003-07-24	15	0000 AST_09_00306242003095934001
Nyiragongo	IKONOS	2001-06-23	4	0000 2000009571000THC
Nyiragongo	IKONOS	2001-06-23	4	2000009571001THC
Nyiragongo	IKONOS	2002-03-08	4	2000013308300THC

Tableau 2.1. Dataset used in this study

Clearly this anomalous elevated NDVI signal and the excessive photosynthetic activity it implies cannot be reconciled except by the combined role of subsurface enhanced heat flux, flux of CO2, and associated water condensation along a structural trend. Different physicochemical processes that can occur on different scales are involved to generate these elevated NDVI linear anomalies. Unfortunately we cannot discuss their spatio-temporal evolution at Nyiragongo because only one image was acquired over the area of interest in 2001 prior to the eruption (Komorowsky et al., 2003; Komorowsky et al., 2004a, 2004b) in 2002. At Etna and Nyiragongo NDVI linear trends mark very precisely the areas where post eruption analysis shows that lava-emissive fractures formed. Thus the observation of anomalous high NDVI linear signal could be interpreted as a precursor of the March 2003 eruption that occurred in the Piano Provenzana area. At Nyiragongo, the early detection of the reactivation of the southern eruptive fracture system far away on the flanks of the volcano from the central crater with its active lava lake could have raised, in the hazard assessment, the determination of the likelihood of occurrence of a future devastating flank-fissure eruption threatening the city of Goma and its 400000 people.

Assuming that deep dyke propagation can occur in volcanic areas without reaching the surface (Gudmundsson, 2002) the kinetics of dyke cooling exclude the hypothesis that the dyke detected on the NDVI images could be the same dyke erupting a few months or years later in the same location. The hypothesis that a series of dykes can be injected within the volcanic edifice before eventually leading to an eruption is supported by several field observations. There are several processes that could account for the preferential growth of vegetation linearly along potentially eruptive fractures. They all relate to the photosynthetic activity of the vegetation (trees at Etna and banana plants at Nyiragongo) and how it translates into a radiometric response of the foliage sensitive to the NDVI algorithm.

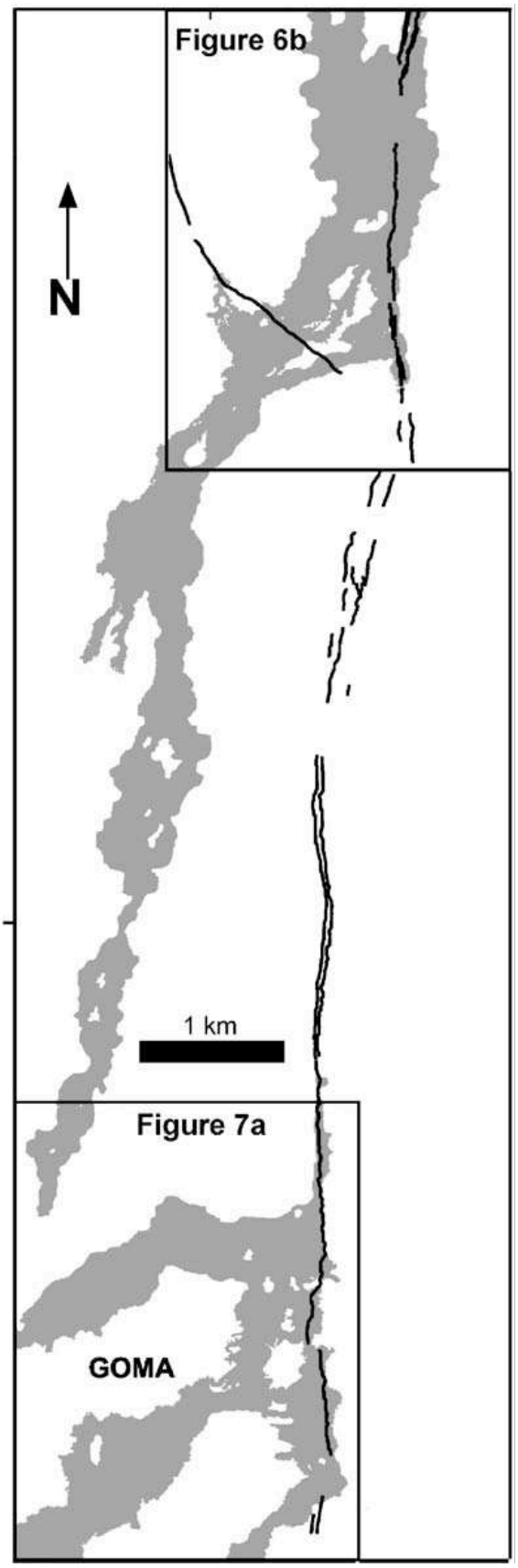

Figure 2.4. Detailed map of the central portion of the lava flows and fractures of the Nyiragongo 2002 eruption. Notice the graben structure and the en-echelon geometry of the two-fracture system. They formed as the result of shallow depth dyke wedge emplacement following a tectonically controlled decrease of the minimum horizontal stress below the volcano which triggered sudden drainage of the lava lake and the magma-filled conduit. The boxes correspond to the portion of the new fracture system which showed as a non-fractured linear area (Figs. 2.5b and 2.6a) with an elevated NDVI signal on IKONOS satellite imagery typical of enhanced plant growth. We postulate that incremental dyke wedge emplacement lead to a combination of increased heat flow, mild CO_2 degassing and vapor condensation through ground fissures and porous lava flow surfaces and thus boosted photosynthetic processes in overlying vegetation.

We have selected a set of parameters potentially detected by the NDVI algorithm and which are relevant to the tree growth and the volcanic processes. First, fracture morphology might play an important role in the channeling of surface runoff, thus making fractures suitable places for vegetation growth. However, the high level of water precipitation in the two studied areas hampers the recognition of any preferential paths for surface runoff. Moreover, the high

permeability of effusive volcanoes prevents formation of permanent streams on Etna and Nyiragongo volcanoes despite the equatorial latitude and/or the high pluviometry. Secondly, thermal flux increases in the fractures and enhanced diffuse emission of ground CO2 gas (Allard et al., 1991; Allard, 1997) will generate the presence of condensing steam in the ground. It has been shown in the past that the CO2 content in the air is linearly related to the observed NDVI signals (Goward et al., 1985; Whiting et al, 1991). We emphasize on the fact that a thermal signal could enhance the NDVI signal by the contribution of the NIR band (see Eq. (1)). Any combination of these two parameters could promote vegetation growth, prevailing that CO2 remain below the flux or concentration threshold above which growth would be slowed (Sorey et al., 1996; Sorey et al., 1998; McGee et al., 2000). Indeed, we have observed on the Infra-Red (IR) band that for the same type of vegetation, the NDVI greenness values are much higher within linear areas where a fracture will form during the eruption than in areas on either side and away from the future fracture. Post-eruptive measurements by the Observatoire Volcanologique de Goma (OVG) show that relict thermal flux and a marked passive degassing of CO2 are associated locally to the central areas of some of the relict emissive fractures where new very healthy vegetation has grown much more efficiently in the few months following the eruption than further away from the fractures. Third, enhanced growth of vegetation in fractures or areas just prior venting of lava might be related to either the rise of the water table due to the upward pressure gradient caused by rising magma from a dyke or the associated geothermal field anomaly. However, this hypothesis is unlikely to cause a single NDVI anomaly detected up to 2 yrs before the eruption of lava. Indeed, the slow rise of a dyke in a fracture cannot take place over several years without significant cooling and thus cessation of upward injection. Instead, we propose that the observed NDVI linear anomalies are caused by the combined physicochemical surface effects consequent to the progressive injection and propagation, a few months before the eruption, of a series of dykes as a dyke wedge (Walker, 1992; Walker, 1999); that did not reach the surface (Gudmundsson, 1992; Gudmundsson and Loetveit, 2005) rather

than a single dyke. This hypothesis is supported by the OVG who observed several months before the eruption (Komorowsky et al., 2004a) the reactivation of fumaroles on fractures active in the 1977 fissure eruption and reported eyewitness accounts of anomalous warm ground in many of the areas where major emissive fractures formed in 2002 (Komorowsky et al., 2004a). The process of dyke wedge formation (Walker, 1975; Gudmundsson, 1995) then culminated in the rapid emplacement of a final and eruptive dyke which propagated rapidly in the direction of the volcanic rift zone. This last hypothesis is able to explain the main part of the signal we have observed at Etna and Nyiragongo. Moreover, our observations suggest that a connection between the two rift zones of Mt. Etna exists. At Mt. Etna, the first eruption phase started in July 2001 (INGV, 2001; Billi et al., 2003). The 2001 flank eruption was reconstructed based on the geochemistry of erupted products from the southern rift zone (Métrich et al., 2004). Subsequent activity from the northern rift zone would thus be linked to over pressurization of the system since 2001 and to the rise of a new batch of deep-sourced magma.

Discussion

This work supports the hypothesis that some dyke injection occurs at depth before the onset of magma injection within the upper part of the volcanic edifices. This implies that the injected volume estimated by ground deformation monitoring is largely underestimated. Recent observations (Houlié et al., 2006) made on Mt. Etna by using Global Positionning System (GPS) support that the minimal volume injected inside the magma feeding system is at least equal to $60\times10_6\ m_3/yr$ between the 1991−1993 and 2000−2002 events, the last two flank eruptions (Branca and Del Carlo, 2004). The discrepancy between the amount of magma injected and the amount of magma erupted is in agreement with quantification of the degassing flux at the volcano scale (Allard et al., 1991; Allard, 1997). While it is admitted that the moderate increase of CO_2 in the air has a positive impact on the plant growth (Lawlor, 1991; Curtis and

Wang, 1998) and on the reproductive processes (LaDeau and Clark, 2001) it has also been recognized that some parameters (the plant's species, health and age; the regional climate in the experimental zone) can moderate this observation (Körner et al., 2005). However, diffuse ground degassing of CO_2 in the two studied areas are clearly not significant enough to increase markedly the local atmospheric concentration of CO_2 to cause plant death as observed in other volcanic areas such as at Mammoth Mountain where soil gas consisted of between 20 and 95 vol.% of CO_2 (Sorey et al., 1996).

Figure 2.5. Main newfracture formed during the Nyiragongo January 2002 eruptionas viewed from the west. This fracture that cuts through banana fields and villages formed as magma from the summit lava lake drained suddenly triggering the propagation of a dyke wedge within the reactivated southern volcanic rift zone over 16 km and towards the city of Goma (population 400000) on the right side of the image. The fracture emitted pahoehoe lava flows (smooth grey surface) and scoriaceous aa lava flows (rough dark surface) that reached and partly destroyed the city of Goma causing widespread devastation and the spontaneous exodus of up to 300000 people (Komorowsky et al., 2004a).

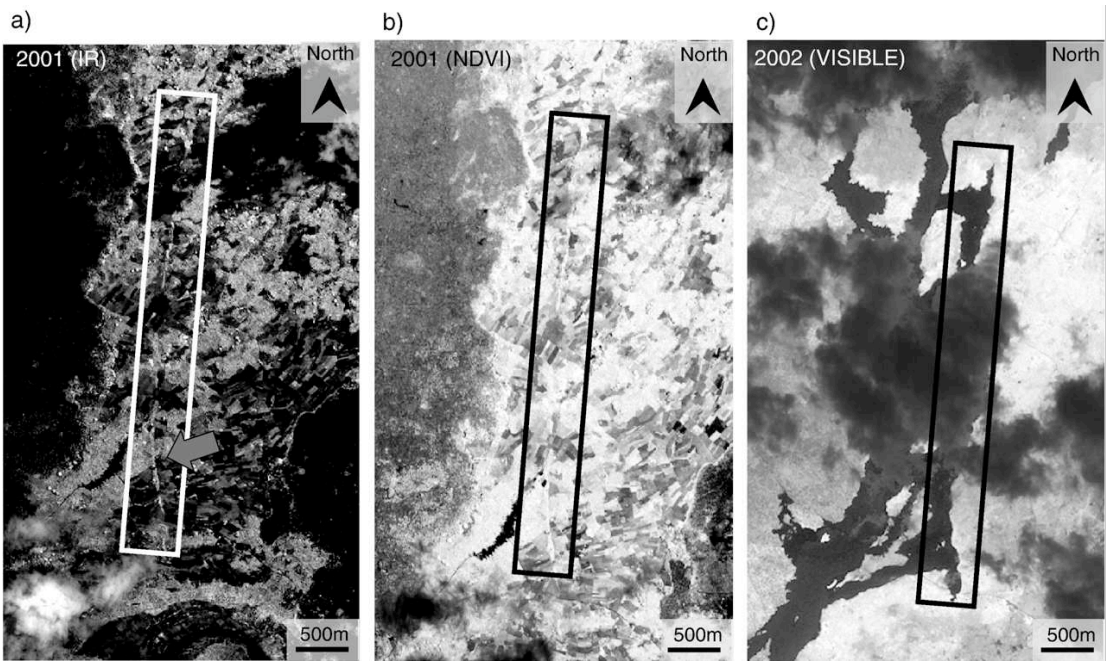

Figure 2.6. NDVI signal along the flanks of Nyiragongo 7 km from the summit.The NDVI process (pixel size=4 m) shows a clear correlation between the fracture-controlled linear patterns of high NDVI values before the eruption (b) and the location of reactivated and new lava-emissive fractures formed during the Nyiragongo 2002 eruption (c). The IR band analysis (a) reveals that the signal is crossing an area (arrow) with growing banana plants. Thus, the signal is not due to a difference of growth of two different vegetal species. The fractures located in this area were observed after the 2002 eruption and identified as newly formed in areas where there was no topographic scarp. Thus the observed signal cannot be linked to a topography effect. The NDVI was processed using IK-ONOS pictures (Space Imaging Inc.).

Routine monitoring by staff of the Goma Volcano Observatory give values between 2 and 6 vol.% for the atmospheric concentration of CO_2 directly inside the 2002 eruptive fractures where a relict moderate heat flux is present and where vegetation has been developing very well since the eruption (M. Yalire, Goma Volcano Observatory, personal communication). We do not have access to the respective contribution of the thermal, degassing and aqueous components responsible for the observed NDVI anomaly anymore. Thus the relative quantification of any of these signal components

is difficult to establish. Some other observations have to be validated and a precursor identification and monitoring strategy has to be completed.

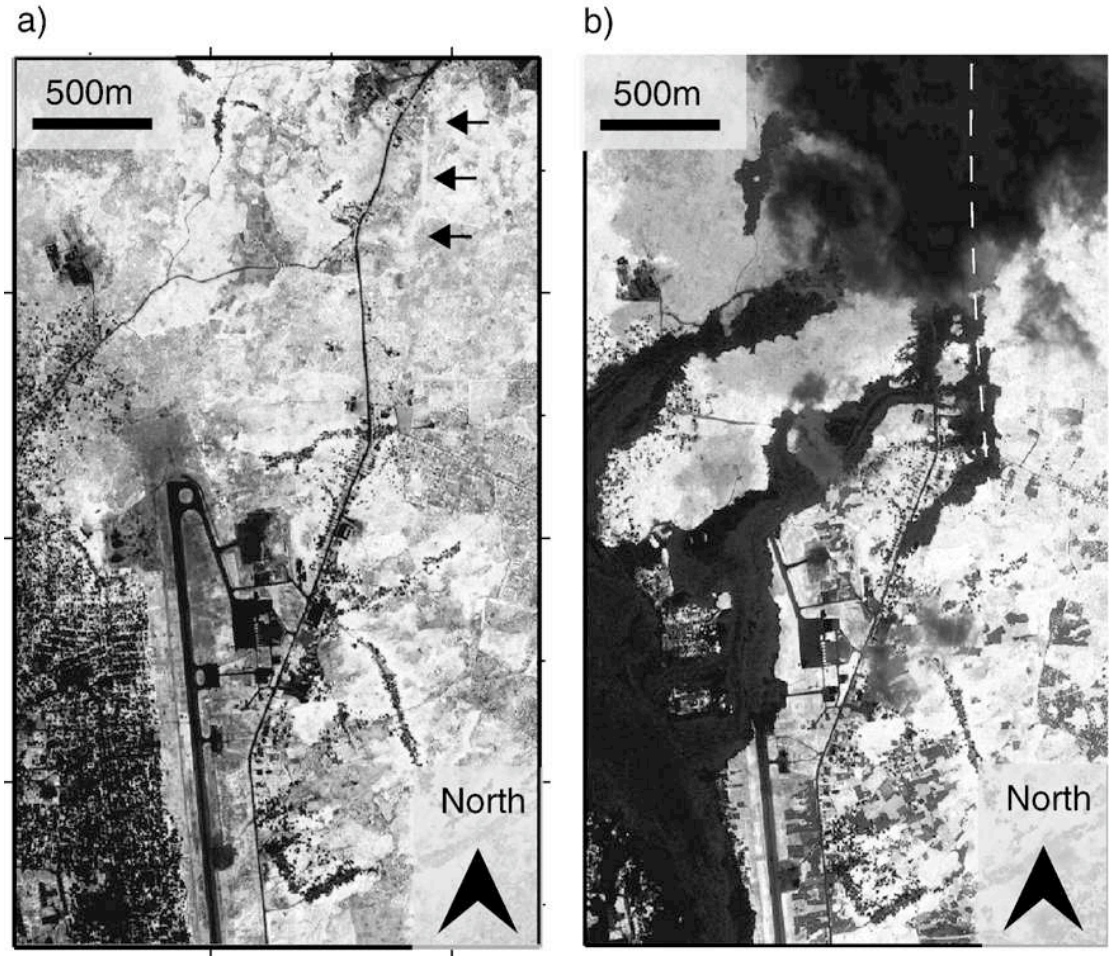

Figure 2.7. NDVI signal along the lower flanks of Nyiragongo 11 km from the summit.This sequence of IKONOS NDVI-processed images (pixel size=4 m) is mapping the vegetation activity before (a) on June 23 2001 and after (b) the 2002 Nyiragongo flank-fissure eruption on March 8 2002. It shows a clear correlation between the linear patterns of high NDVI values 7 months before the eruption (2001) and the location of the eruptive fractures developed during the 2002 eruption. Black arrows indicate the presence of well-marked linear pattern in NDVI values 1 yr before the eruption. The dashed line represents the active fracture of the 2002 eruption and its associated lava flows. This data remarkably shows that pre-existing fractures were reactivated in 2002 to feed several lava flows. Non-ortho-rectified images georeferenced in WGS84 geodetic system and projected into UTM35S (in km).

The new methodology described here to identify and map potentially active fractures and faults on volcanoes has potentially important implications regarding installation and upgrade of monitoring networks, particularly on deeply vegetated restless volcanoes as well as on volcanoes with limited access (remote location, risks from volcanic activity and/or armed conflicts (Casadevall and Lockwood, 1995)). More importantly, on volcanoes that experience a change in eruptive style from crater-centered to eccentric flank activity or for which new inactive volcanic rift zones could be reactivated towards populated areas, our methodology constitutes a new tool for early detection of potential flank eruptive vents. By improving the understanding of the link between edifice structure and eruptive activity of effusive volcanoes it can significantly improve integrated risk analysis and the effectiveness of early-detection warning systems for populations at risk.

Acknowledgements

We are particularly grateful for logistical and scientific input from staff of the Goma Volcano Observatory who monitor the Virunga volcanoes with competence and courage in particularly adverse and dangerous conditions. We are grateful to Mathieu Yalire (GVO) for sharing with us unpublished CO_2 concentration data on some fractures. We thank the UN Office of Coordination of Humanitarian Affairs (UNOCHA), the UN Development Program (UNDP), the International Strategy for Disaster Reduction, the French Ministry of Foreign Affairs (MAE), the Observatoires Volcanologiques et Sismologiques of IPGP and the INSU GPS instrument pool for financial and logistical support. A. Le Guellec (Latitude Geosystems) provided valuable assistance with IKONOS (Space Imaging Inc.) imagery purchased with UNOCHA funding. We are grateful to A. Nercessian, P. Allard, M. Halbwachs, C. Newhall, M. Polland, and S. Carn for discussions. We thank A. Gudmundsson for his review which improved our paper, as well as two anonymous reviewers. This article is a University of California at Berkeley contribution number 06-04.

Chapter 3

Deformation between 1989 and 1997 at Piton de la Fournaise volcano retrieved from correlation of panchromatic airborne images

by Marcello de Michele[1, 2] and Pierre Briole[1]

[1] *UMR CNRS 7531, Institut de Physique du Globe de Paris, Equipe de Géodésie et Gravimétrie, Paris, France.*

[2] *Now at Bureau de Recherches Géologiques et Minéres, Orleans, France*

Foreword - This chapter resumes the work that I have performed at the *Institut de Physique du Globe de Paris* during 2003/2004 under the supervision of Pierre Briole who had the precursory idea of using airborne pictures to measure displacements of the Earth surface. This was my main research topic at that time. The results presented in this chapter have been submitted for publication in July 2005 to *Geophysical Journal International* and published in 2007 as de Michele and Briole (2007). This delay is mainly due to my moving from the *Institut de Physique du Globe de Paris* to *TRE (Telerilevamento Europa)* and then to the *Bureau de Recherches Géologiques et Minières* (BRGM). This work has benefited from stimulating discussions with Rémi Michel on the topic of image correlation and it would not have been made possible without the help of Hélène Vadon on the use of MEDICIS software during quite a few visits at CNES.

Summary

We processed two panchromatic airborne images in the attempt to measure deformation on Piton de la Fournaise volcano between 1989 and 1997. Piton de la Fournaise erupted three times during 1989-1997 with fissures opening near Dolomieu summit crater. During this period no InSAR data were available and only few geodetic points surveyed the summit crater. We therefore apply for the first time the subpixel image-correlation technique on airborne images for monitoring ground deformation on Piton de la Fournaise volcano. Correlogram analysis reveals cumulative deformation in the summit area. We observe ESE spreading of the summit caused by the inflation-deflation cycle during 1989-1997. We calculated relative ground displacement along both sides of the main eruptive fissures, finding a maximum of 1.8 (±0.42) meters opening. Direct comparison between deformation retrieved by correlation and available geodetic data at four locations shows qualitative agreement. We demonstrate the potential of sub-pixel image correlation technique, using panchromatic airborne images, for deformation monitoring on volcanoes. We also illustrate the capability of this technique for remote lava flow mapping.

Introduction

Piton de la Fournaise, La Reunion Island, France, is an active basaltic shield volcano (Fig. 3.1). Most of its recent effusive activity, including the 1990, 1991 and 1992 eruptions, is located within the Enclos Fouqué caldera. Eruptive fissures are mainly located near the central crater, Dolomieu. The fissure pattern on Piton de la Fournaise outlines two unstable rift zones trending NE and SE respectively where most eruptions and dyke intrusions occur, while most pre-eruptive swarm earthquakes occur under Dolomieu summit crater (Nercessian *et al.* 1995). Deformation and flank spreading is also localized in the summit area, being well correlated in time and location with eruptions (Briole *et al.* 1998). Several studies have shown that flank spread-

ing on Piton de la Fournaise might result from both dike intrusions and gravitational sliding towards low confinement areas (e. g. Lenat *et al*. 2001; Merle *et al.* 2003).

The year 1998 marked the end of 5 years quiescence at Piton de la Fournaise volcano. While eruptions occurring from 1998 to the present have been studied by remote sensing techniques (e.g. Sigmudsson *et al*. 1999; Froger *et al.* 2004; Fukushima *et al.* 2005), the period 1989-1997 lacks similar data. Moreover, between 1989 and 1997 there are far fewer ground geodetic data than now, with GPS used increasingly since 1992 but especially since 1999 when more portable units became available. In this study we focus on the period 1989-1997, in an attempt to measure ground displacement by an image correlation technique applied to panchromatic airborne images. Image correlation techniques represent a valuable complement to Differential Synthetic Aperture Radar Interferometry (DInSAR), in particular near faults and fracture zones where large displacements result in a poorly coherent SAR signal.

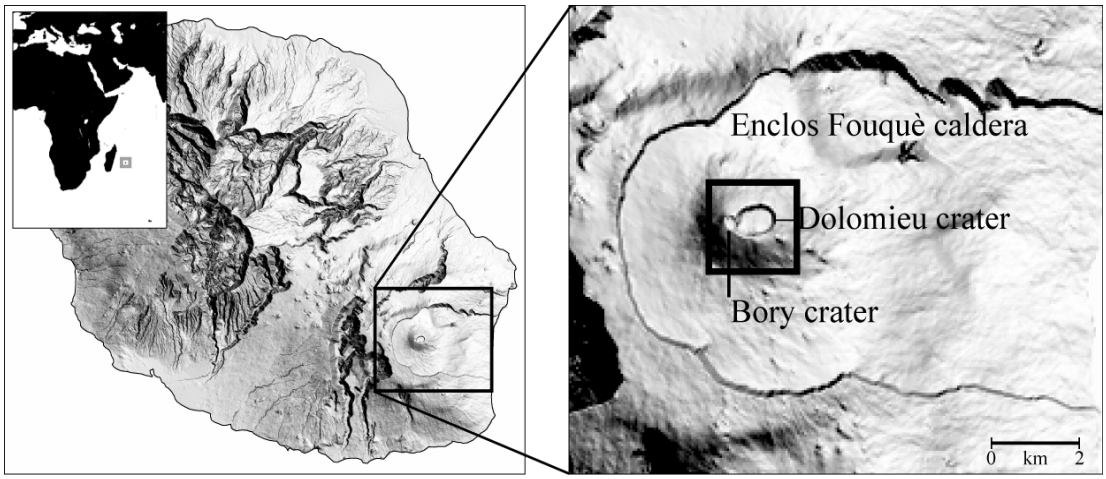

Figure 3.1. Study area. Piton de la Fournaise volcano, La Reunion Island, Indian Ocean. Black box in the right image represents the study area in figure 3.

This technique has been successfully applied using both SAR amplitude images and satellite/airborne optical images in different fields of study. In particular, in seismo-tectonics (e. g. Van Puymbroeck *et al.* 2000; Michel & Avouac 1999; Michel & Avouac 2002; Dominguez *et al.* 2003, Binet & Bollinger, 2005; Fialko *et al.* 2005, Klinger *et al.*, 2006; Michel & Avouac, 2006), in volcano deformation (Tobita *et al.* 2001) and in gravitational movement assessment (*e.g.* Delacourt *et al*. 2004; Berthier *et al. 2005*). Nevertheless, this is the first time that the correlation technique has been applied to panchromatic airborne images for quantifying volcano deformation.

Eruptive activity on Piton de la Fournaise (1989-1997)

Three basaltic eruptions took place in the period 1989-1997 at Piton de la Fournaise volcano in 1990, in 1991 and in 1992 (Toutain *et al.* 1990; Toutain *et al.* 1991; Toutain *et al.* 1992a) (Fig. 3.2). These eruptions occurred in an unpopulated area and did not induce any threat to property.

The 1990 eruption began on January 18th from both the E interior of the Dolomieu crater and SE Dolomieu upper flank where it propagated S-SE for several hundreds of meters. During the dyke injection, tilt-meters recorded migration of the deformation centres in the same direction as the feeding fracture (Toutain *et al.* 1990).

The 1991 eruption started on July 19th. Lava was emitted from two fissures along an eruptive fissure trending ENE. One fissure was localised inside Dolomieu crater, erupting some lava along its SE border. The other fissure was localised outside Dolomieu crater (Toutain *et al.* 1991).

The 1992 eruption began on August 27th from a fissure within the S-W Dolomieu crater area. The fissure propagated rapidly southward, crossing the rim. Four additional fissures opened SE of the first fissure. The seismic pattern suggested a small magma pocket fed the intrusion moving up towards Dolomieu (Toutain *et al.* 1992a).

The tilt-meter pattern suggested general inflation of Dolomieu crater (Toutain *et al.* 1992b).

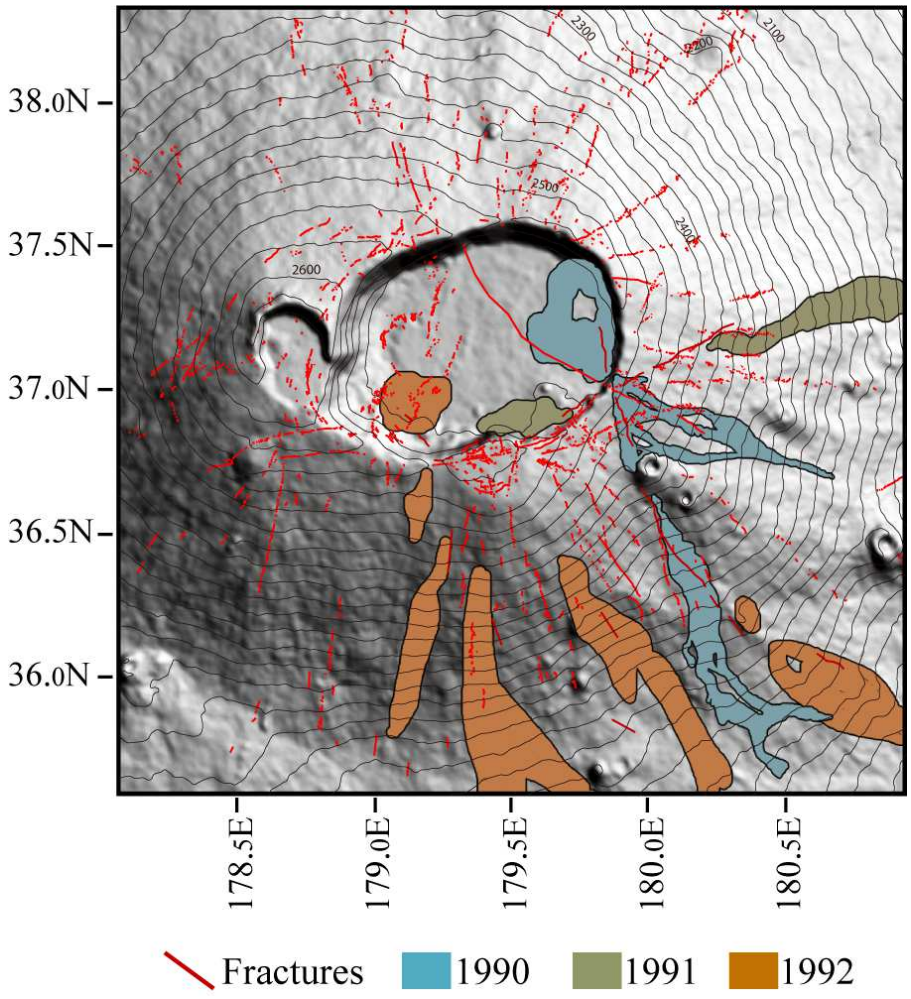

Figure 3.2. Map representing the 1990, 1991, and 1992 lava flows at Piton de la Fournaise after Toutain et al., 1990, 1991, 1992a. The lava flows have been plotted on the DEM. Red lines represent the main fractures within the study area. Units are in km, Gauss-Laborde map projection.

Data

Two panchromatic airborne images have been used in this study (Fig. 3.3). Both the images have been acquired using wide-angle cameras during two IGN (Institut Géographique National) photogrammetric surveys. The first image was acquired during a

1989 survey (mission REU, 112, P) at 1:20.000 scale. The second image was acquired during a 1997 survey (mission REU, 119, P) at 1:30.000 scale. Both have been scanned at 1300 dpi (dots per inch) resolution, 8-bit pixel depth.

There are several reasons for selecting the aforementioned images. Firstly, both images cover the summit volcanic area, which is the place where we knew deformation had been active in the period 1989-1997, with the deformation sometimes visible in the field (e. g. new eruptive fissures from decimetres to meters opening). Secondly, the base to height ratio (B/H) between the chosen images is the smallest among the entire set of available images**,** which minimises the effect of topography on the offset measurements. Thirdly, the pixel size (0.5m for 1989 images and 0.7m for 1997 images) suits the requirement for fissure opening measurements using sub-pixel correlation analysis.

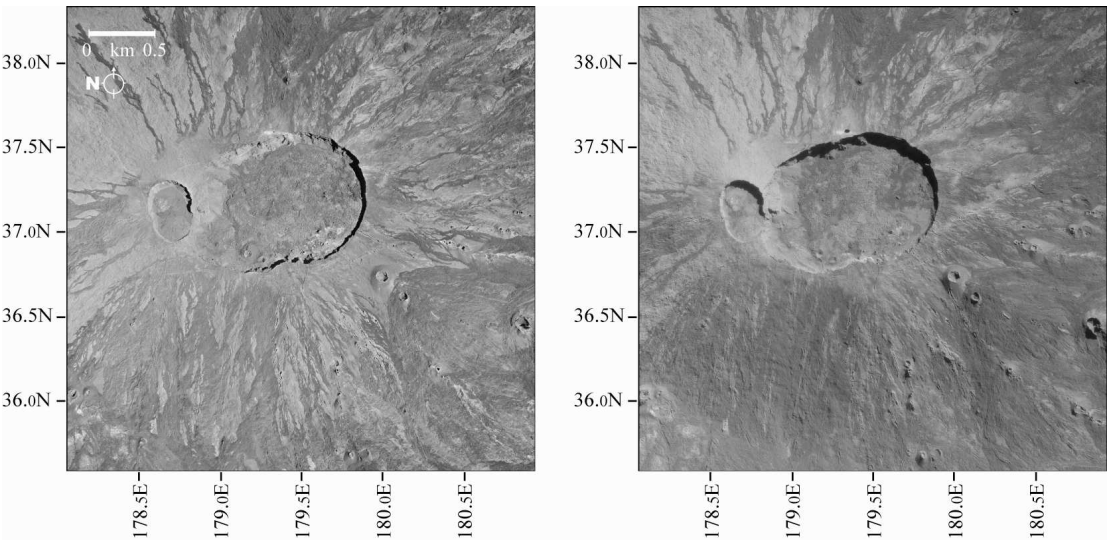

Figure 3.3. Piton de la Fournaise summit area. 1989 orthoimage (left), 1997 orthoimage (right). These are the images we have used in the correlation analysis. Notice the differences in solar illumination, and surface changes due to new lava flows. Units are in km, Gauss-Laborde map projection.

We used a five metre grid size Digital Elevation Model (DEM) as a geo-coded reference surface in the ortho-rectification process. The DEM covers a25 square km area on top of Piton de la Fournaise. The DEM accuracy has been tested against over 10,000 kinematic differential GPS points (DGPS) (Trembley & Briole, 2005). The standard deviation between the DEM and the DGPS profiles has been found to be 1.5m with a maximal error of 3m.

Data processing and accuracy assessment

The image correlation technique relies on the statistical analysis of two sets of data (e.g. digital panchromatic imagery). This technique matches the 'before' image (1989) and the 'after' image (1997) at each point on a grid, analysing the degrees of local correlation at each step. Differences in the local instantaneous frequency of the images result in sub-pixel spatial differences in ground patterns (Crippen, 1992). The results are an expression of both movements in the ground surface and image distortions. Sources of image distortions are very well discussed in Michel & Avouac (2006). Distortions mainly depend on the B/H, where B is the perpendicular distance between the two airplane positions and H is the altitude above the datum. The B/H controls the stereoscopic effect and therefore the degree of local differences in both scale and feature position between the two air-photos. Moreover, when correlating two images, the B/H determines the level of quality the DEM has to have, given that the higher the B/H the higher the apparent horizontal displacement that would be induced by an error in the DEM (Van Puymbroeck *et al.* 2000). In a hypothetical case where both the images have been acquired from exactly the same position (B/H=0), one would not need to perform any ortho-rectification since there would not be any stereoscopic effect. In our case (B/H≈0.25), an error of 1.5 meter in the DEM would create an apparent horizontal displacement of ~0.3 meters (~0.4 pixels). Since a finer DEM is not available, 0.3 meters represents one significant limit in the accuracy of our measurements. Another source of distortion might come from the camera lens. This distortion is virtually zero at the centre of the scene and increase towards the

edges. Our photos have been acquired by a metric camera so that the degree of distortion rate versus the lens radius is a known parameter that can be compensated during resampling.

The image correlation technique requires both the airborne images to be re-projected into the same geometry before calculating sub-pixel cross-correlation. Therefore, images are first projected into the DEM geometry (Orthorectification). In the orthorectification process we used both the metric camera parameters and 40 ground control points (GCPs). The viewing camera parameters have been provided by IGN while the GCPs have been retrieved from both the GPS network at Piton de La Fournaise and selected points on kinematic GPS profiles from Trembley & Briole (2005). Moreover, 20 tie points identified on both the images have been used to improve co-registration. Both the images have then been resampled to 0.7 meters pixel size using a cubic convolution in order to preserve radiometric quality. Uncertainties on the viewing camera parameters are minimised in the process of orthorectification. However, a residual low wavelength error might bias the results. An empirical estimate of the cumulative effects of all un-modelled sources of errors could not be performed in this study due to the lack of quality data in non-deforming periods prior to 1989. Therefore, somehow our error assessment is underestimated. Michel and Avouac (2006) have shown that un-modelled errors other than the DEM uncertainty might account for another ~1/3 of the overall error. This yields a comparative estimate which we use to reassess the accuracy of our offset measurement to ±0.42 meters.

The correlation analysis has been performed by the use of MEDICIS software. MEDICIS allows sub-pixel offset measurements by means of a sliding NxM window (Centre National d'Etude Spatiales, 2000) with an accuracy of 1/10 pixel. The size of the sliding window is chosen according to local differences in the radiometry of the input images. Each pixel is a measure of the radiance and each digital number changes according to differences in either solar illumination or surface changes, mainly. Therefore, on the one hand, a small window would be too sensitive to noise (i.e. random radiometric changes). On the other hand, a large window would be less

sensitive to non-uniform offsets. In this case study, a 31x31pixel sliding window has been used. It yields independent measurements every 16 pixels (11.2 metres). The local correlation coefficient (ρ) is calculated between the two images at each step of the grid. The local correlation coefficient is a normalised value that varies between 0 and 1. It gives an assessment of the radiometric differences between the images and therefore provides us with an estimate of the uncertainties on the measurements; i.e., below a particular threshold the measurement is not reliable. In this study, we do not use offset values with $\rho \leq 0.4$. Radiometric changes typically reflect physical variations occurring on the ground between the acquisition of the two photos. Differences in solar illumination and random surface changes (like erosion phenomena or lava flows) result in poorly correlated pixels.

Quantification of displacement

Fig. 3.4 shows the results of correlation analysis between the 1989 and the 1997 images. Figs. 4a and 4b represent the East and South offset respectively. These data represent the cumulative ground displacement of the summit area of Piton de la Fournaise over an eight year period. They show that the summit area experienced ground deformation due to the inflation/deflation cycle triggered by dike intrusions in 1990-1991-1992. Deformation is mainly localised south-east of Dolomieu crater where north-south oriented fissures opened during the eruptions. This sector is collapsing south-eastward. In this sector of the volcano, our data show a spatially continuous displacement field, which we think is due not only to opening of new fissures but also to reactivation of ancient fractures. In fact, ground deformation is not only localised in the vicinity of each new eruptive fissure but also shows up with a clear coherent signal around ancient fractures that were not erupting during 1989-1997.

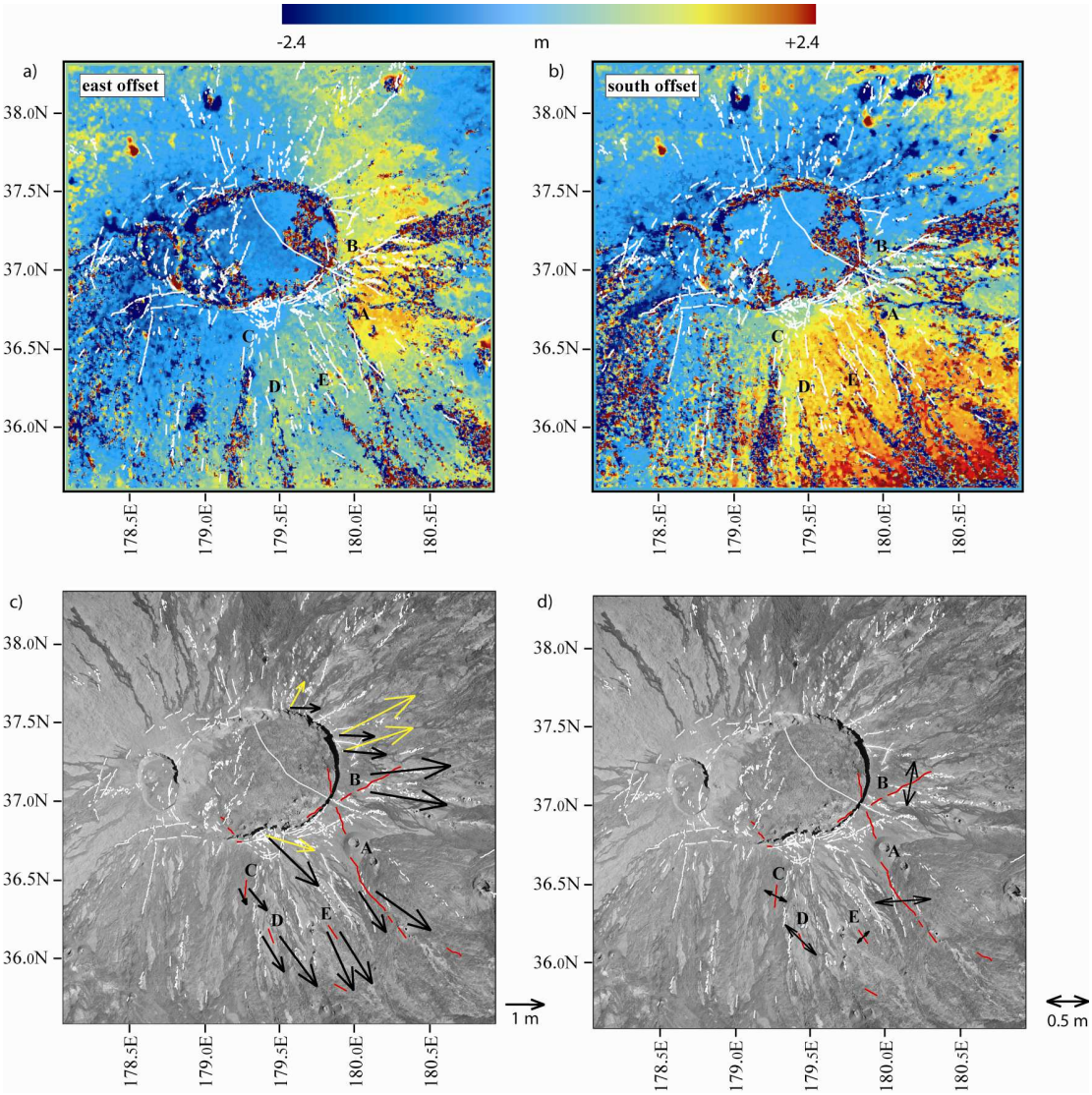

Figure 3.4. Correlation analysis results.Offsets between 1997 orthoimage and 1989 orthoimage have been calculated. a) east offset, b) south offset, c), GPS velocity vectors, in yellow, compared with offset values, in black, along main eruptive fissures and at GPS locations, d) averaged absolute fracture widening along main eruptive fissures. Noisy values in a) and b) correspond to poor correlation areas where large differences in radiometry exist between the two images (e. g. the 1990 lava flow, east of the Dolomieu crater interior). Differences in solar illumination also affect the quality of the correlation in the steeper areas. We superimposed the fracture map, in white, on the offset measurements a) and b). Areas with stronger deformation gradients correspond to the location of the 1990, 1991 and 1992 eruptive fissures. A spatial relationship between fractures and displacement offset is clear also for several pre-existing fractures, which are not directly related to the 1990, 1991 and 1992 dykes intrusions.

We inferred the ancient fractures from direct observation of the ortho-images in 1989 and 1997 (plotted in white in Fig. 3.4c and 3.4d). We suggest that, during the process of inflation, the ground begins to deform in areas of weak resistance (i.e. ancient fractures) while the new dike is intruding and creating a new fissure. The few available geodetic measurements from Briole *et al*. (1998) (yellow vectors in Fig. 3.4c) show that magnitude and direction of the deformation inferred by field geodesy is comparatively consistent with displacement field inferred by correlation (Tab. 3.I). Differences can be partly explained by the fact that field geodesy displacements are calculated on a slightly different time period (1985-1992) and they represent point wise values. Correlation results quantify cumulative displacements across 1989-1997 and are characterized by spatially continuous analyses where each pixel embodies information about averaged displacement occurring within 21.7 metres on the ground (31x31 pixels).

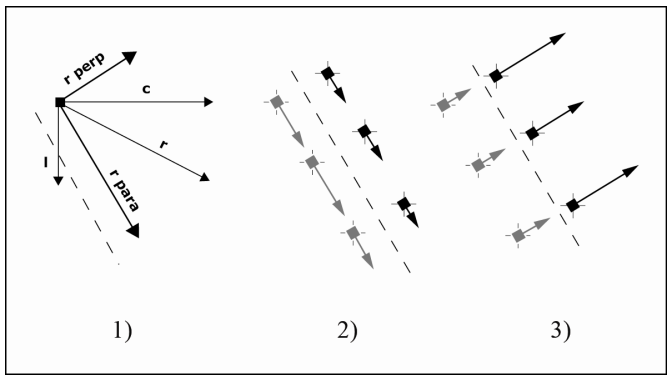

Figure 3.5a. Illustration of the method used to produce graphs in figure 3.5b and 3.5c. The offset perpendicular (r perp) and parallel (r para) component in respect to fissure direction (dashed line) is shown in 1). l **and** c **represents the original offset lines and columns vectors at given geographic location. 2) and 3) represents the methodology that we used for offset measurements across eruptive fissures.**

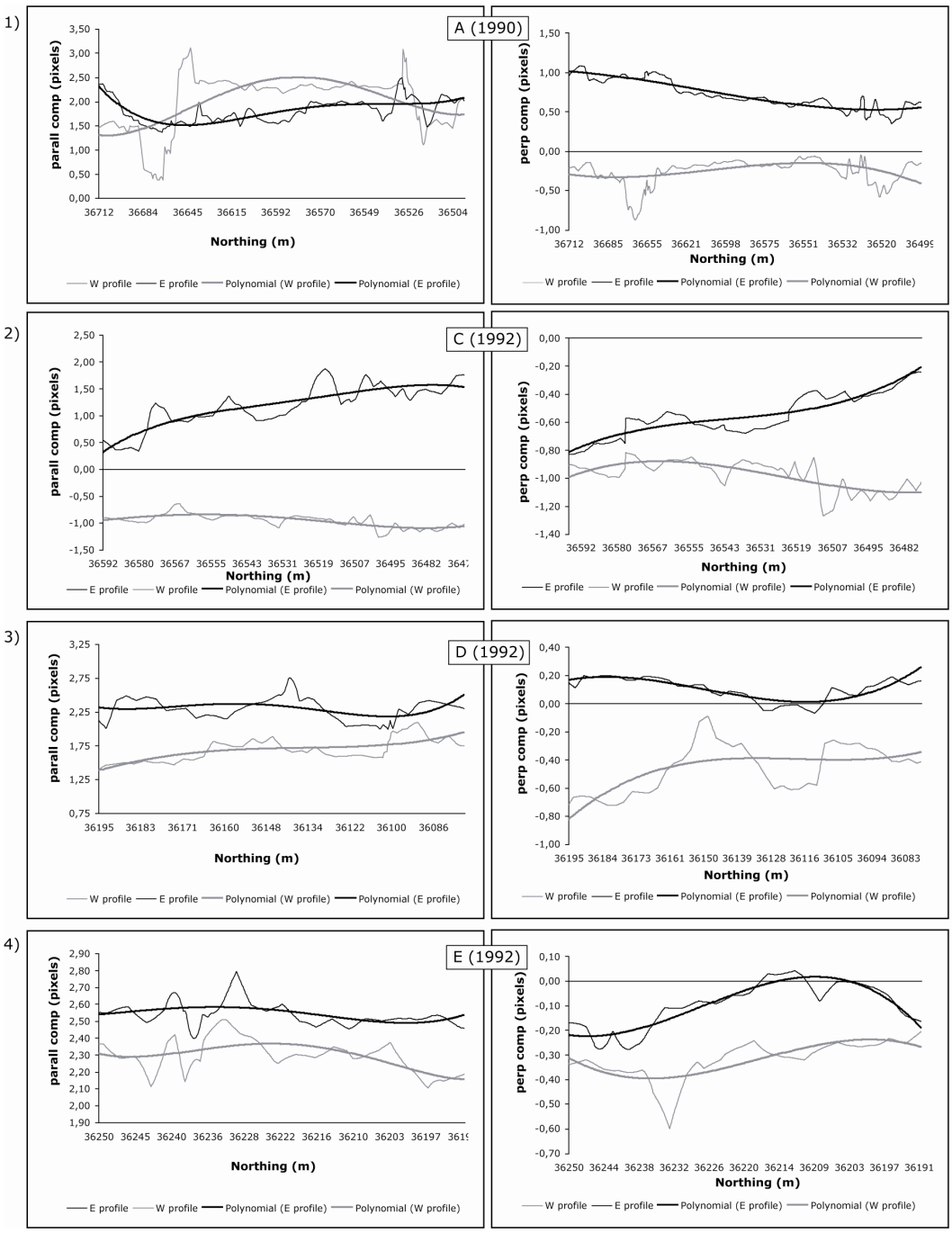

Figure 3.5b. Estimation of the offset (parallel and perpendicular components) of the 1990 (A) and 1992 (C, D, E) eruptive fissures. Refer to Figure 4 for fissure A), C), D) and E) locations. Grey lines correspond to offset values on the western border and black lines to values on the eastern border of each fissure.

We think that long wavelength features in the offset field (lower than $1km^{-1}$) represent cumulative volcano inflation. Nevertheless, the uncertainty on aerial image offset measurements at this long wavelength is significantly higher due to un-modeled low frequency bias thus preventing precise quantitative long-wavelength deformation assessment.

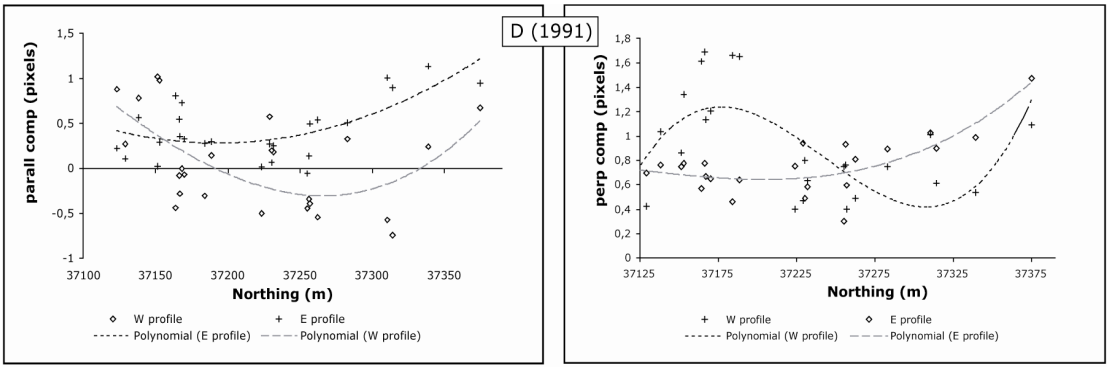

Figure 3,5c. Estimation of the offset (parallel and perpendicular components) of the 1991 eruptive fissure (B). Refer to Figure 3.4 for fissure B) location. Although its signature is clear in the data, the 1991 eruptive fissure opening could not be accurately measured probably because the deformation is spread across several small fissures rather than localised, generating a noisy deformation pattern in that area. Moreover, lava flows in 1991 covers much of the fracture, yielding low ρ.

We estimated the distribution of perpendicular and parallel relative motion across the 1990, 1992 and 1992 eruptive fissures (Fig. 3.5a). For that, we measured the offset field on both edges of selected eruptive fissures in areas where lava flows did not cover the surface, yielding $\rho>0.4$ (Fig. 3.5b, 3.5c). The results are plotted in Fig. 3.5b-c as an offset versus geo-location graph. We observe that each fissure widens in a non-uniform fashion and each side shows different amounts of deformation. Moreover, fissures open and deform the ground with two components, parallel and

orthogonal to their direction. Although widening is non-uniform along each fissure, we can state that there is an average opening of about 1 meter with a maximum widening of 1.8±0.42 meters occurring on fracture 1992b. Correlation around the 1991 main fissure is poor, which is due to significant surface changes. In particular, the 1991 fissure partially overlaps the 1990 lava flow. Moreover, deformation around the 1991 fissure is spread across several small fractures rather than localised, generating a noisy deformation pattern in that area. Therefore, measurements around the 1991 eruptive fissure are less dense or missing.

Mapping lava flows

An interesting side-result of this study is shown in Fig. 3.6. This figure illustrates that it is possible to use the correlation-score image to map surface changes due to lava flows resurfacing between the two image acquisitions. This map has been produced by choosing pixels with $\rho<0.3$ and supervising the results with *a priori* knowledge about the 1990, 1991, 1992 lava flow locations (Toutain *et al*., 1990, 1991, 1992). We think that this methodology could be run automatically if images are acquired routinely before and after a single particular eruption. The correlation-score image in Fig. 6a has also been useful to double-check the location of each eruptive fissure. A comparison between Fig. 3.6b and Fig. 3.2 shows a good fit between the ground-based map and the coherence-based map.

Discussion and conclusions

We measured ground deformation between 1989 and 1997 on Piton de la Fournaise volcano by correlating two panchromatic airborne images. During the study period, no SAR data were available on Piton de la Fournaise. The offset results clearly show broad flank deformation of the east-southeast side of the summit area. The deformation is the result of several inflation/deflation eruptive cycles and consequent em-

placement of dyke intrusions in 1990, 1991 and 1992. Offsets between the 1989 and 1997 images represent cumulative displacement of the summit area and correspond to the sum of several stages of Piton de la Fournaise activity.

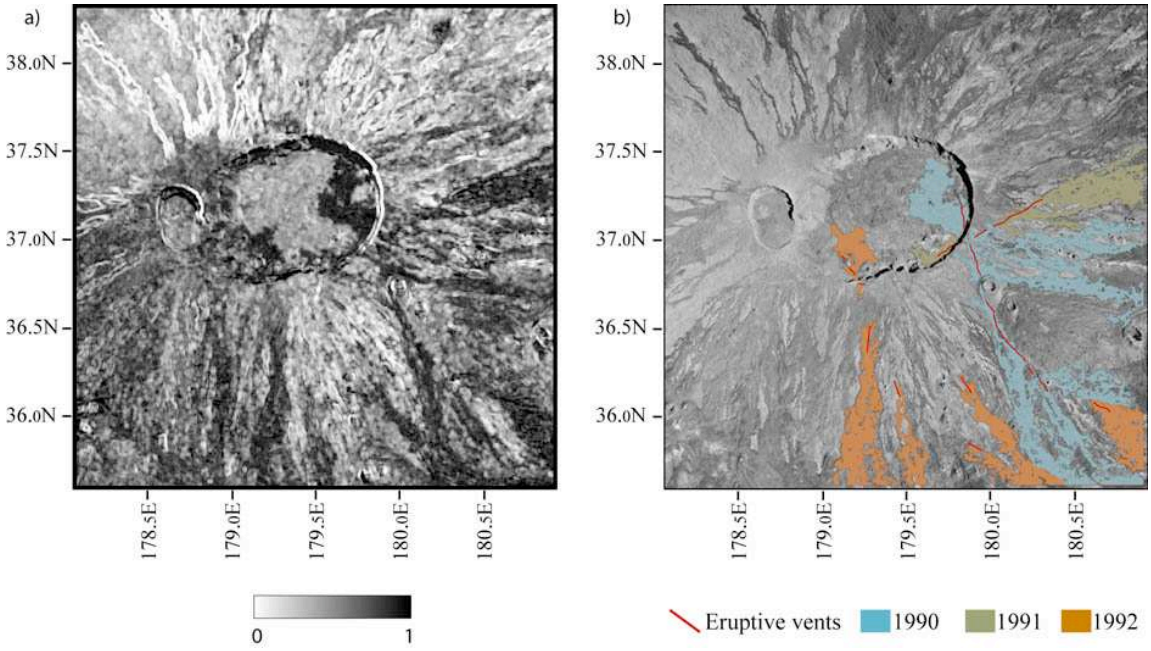

Figure 3.6. Correlation coefficient image yields scores in terms of radiometric changes between the orthoimages. New lava flows being one of the most significant source of radiometric change, a map of the 1990, 1991, and 1992 lava flows could be inferred from the correlation coefficient image in a). Pixels with correlation index lower than 0.3 and *a posteriori* knowledge have been used to estimate the location of new lava flows and produce the map in b). See Figure 2 for comparison.

Fissure geometry on Piton de la Fournaise is typically *en echelon*, which exhibits splays of fractures rather than a single one. We found that the flank deformation is not only due to new fissures opening (eruptions in 1990, 1991 and 1992) but also to reactivation of pre-existing fractures. This observation is supported by the overlap between changes in offset gradient and part of the non-eruptive fracture pattern. Pre-existing fractures have been possibly reactivated by either an inflation-deflation cycle

in the 1989-1997 period, gravitational sliding between 1989 and 1997 or sporadic movements due to ground shaking crises during dyke intrusions.

	N_g	N_o	E_g	E_o	M_g	M_o
I	0.61	**0.01**	0.42	**0.59**	0.73	**0.77**
II	1.30	**-0.30**	1.88	**0.88**	2.20	**0.92**
III	0.83	**-0.33**	1.53	**0.94**	1.74	**0.99**
IV	-0.45	**-1.31**	1.21	**1.23**	1.29	**1.78**

Table 3.I . Comparison between North and East components of deformation vectors measured by geodetic surveys (N_g, E_g) and by offset (N_o, E_o) at points locations I, II, III, IV. Refer to figure 4c, where point location I is the northernmost point followed by point II, III and IV clockwise. M_g and M_o represent vectors magnitude.

Development of arrays of strainmeters monitoring the opening of fractures on Piton de la Fournaise would help in discriminating among the aforementioned hypotheses in the future. We notice that reactivated fractures largely outline the unstable sector ESE of Dolomieu crater. By measuring offsets around the main eruptive fissures we found that the way each fissure widens is non-uniform along its length. The fact that offsets measured by correlation are comparatively consistent with displacement vectors acquired in a slightly different period using geodetic data acquired in the field corroborates our results. Still, we can observe a general underestimation of deformation retrieved by correlation offset in respect to ground geodetic data. This might be due to the different monitoring time period and probably to underestimation of long wavelength offset bias. Moreover, offset measures are averaged on a 21,7 meters correlation window (31x31 pixels) while geodetic data correspond to point-wise measures, which partially explains the misfit at GPS location.

The B/H ratio between the images, even though small, is not zero. Therefore we expect orthorectification residual to bias the offset measurement. Further low frequency bias might come from temporary and permanent thermo-mechanical deformation of negative films. Film distortions could yield low frequency bias with magnitude greater than 1 meter and thus putting severe limitation in the accuracy of the offset measures at long wavelength (Michel & Avouac, 2006). This could also partially explain the misfits between the ground geodetic measurements and offset at GPS locations in the present study. Nonetheless, low frequency residuals do not prevent the accurate measurement of fracture opening as a relative movement across eruptive fractures.

A possible improvement of the measurement method used in this study would be the independent estimation of the uncorrelated bias amplitude still present in the displacement map. This estimation would be feasible by correlating ortho-rectified air-photos acquired on the summit area over a period in which no deformation has occurred. Unfortunately, our archive does not contain data suitable for such analysis.

An ideal data acquisition configuration would consist of air-photos acquired routinely with virtually zero baseline (B/H=0). In this way, 1) there would be a large number of data available, 2) the data would not be biased by temporal decorrelation due to differences in solar illumination or changes in the ground surface, 3) there would be virtually zero uncertainty due to DEM inaccuracies.

Eight years have passed between the first and the second photo acquisition. Differences in solar illumination and changes of the volcano surface (like new lava flows and ancient lava flows erosion) contributed to decorrelation. We performed a decorrelation analysis to map new lava flows, since new lava flows generate one of the most important sources of decorrelation in this study. Lava flow mapping transcends the aims of this paper, so it is not discussed deeply. Nevertheless, we illustrate the potential of this technique for remote lava flow mapping.

In conclusion, eruptions of 1990, 1991 and 1992 on Piton de la Fournaise volcano produced an important summit deformation, which could be mapped by correlation of panchromatic airborne images. Fracture patterns between 1989 and 1997 outline an unstable area in the ESE fraction of Dolomieu crater. Monitoring in terms of both deformation and lava flow mapping could be improved by routinely acquiring data from the same point of view. Correlograms derived from panchromatic imagery have shown the potential for volcanic deformation measurements as a complement to differential SAR interferometry and GPS displacement measurement.

Acknowledgements

This study has been carried out in the frame of the Space Volcanoes Observatory (SVO) project (Briole, 2003) supported by CNES. We wish to thank Hélène Vadon (CNES) and Remi Michel (CEA) for fruitful discussions. We are grateful to two anonymous reviewers whose comments and suggestions improved our manuscript.

Chapter 4

Measuring coseismic deformation on the northern segment of the Bam-Baravat escarpment associated with the 2003 Bam (Iran) earthquake, by correlation of very-high-resolution satellite imagery

by Marcello de Michele[1], Daniel Raucoules, Hideo Aochi, Nicolas Baghdadi and Claudie Carnec

[1] All the authors are with the French Geological Survey (BRGM), Development Planning and Natural Risks Division, Orléans, France

Foreword - This chapter resumes part of the research work that I carried out in 2005/2006 at BRGM and that has been published as de Michele et al., 2008 in *Geophysical Journal International.* This research started from the need of using very high-resolution imagery data such as Quickbird data to retrieve co-seismic surface displacement without having access to the images ancillary information. So basically, we tried to answer the question «what can you do when you do not have access to the image geometry data and need to measure ground displacement?». Also we try to address the issue of using high spatial resolution image data without having high spatial resolution topography data. This paper has been the object of some critics, as we should have gone into some more details on the technique given that this is the first time Quickbird is used along with the image correlation technique. We published this work as a four pages letter as we thought that the displacement on the Bam-Baravat escarpment implied some important issues for seismic hazard in the region. We did go further in this research direction (see chapter 7 and 9) and a more detailed study is ongoing at the

moment. Despite the critics we like to think that with this work we have introduced a kind of «three pass» image correlation method.

Summary

The role that the oblique-reverse fault projecting to the surface at the Bam-Baravat escarpment played in the slip accommodation of the 2003 (Mw 6.5) Bam earthquake is still unclear regardless of many seismological and geodetic studies following this event. In this study, we correlate pre- and post-seismic very high spatial resolution panchromatic satellite images to map coseismic surface deformation along the northern segment of the Bam-Baravat escarpment, a few hundred meters east of the urban area of Bam. Using a new approach based on Principal Component Analysis (PCA) on offset measurements we obtain 1.8 ±0.6 cm east slip component and 2 to 6 ±0.6 cm south slip component along the fault segment. Our results are consistent with ground observations over the study area and support the idea of the reactivation of the shallow part of this fault segment.

Introduction

The city of Bam is located between the Jebal-Barez and the Kafut mountain ranges in southern Kerman Province, Iran. It is situated near the south-eastern termination of the Nayband and Gawk fault system (Figure 4.1). This active right-lateral strike-slip system accommodates about 15 mm/yr of the collision between the Arabian and the Eurasian plates (Vernant *et al.,* 2004). Although the area is seismically active, there are no recorded historical earthquakes in the Bam area, which is one of the oldest centres of urban life in Iran (e.g. Ambraseys & Melville, 1982; Ashtiany & Mousavi, 2005).

The city of Bam was struck by an M_w 6.5 earthquake on the 26 December 2003. The epicentre is located south of Bam, some 10 km west of a pre-existing structural fea-

ture known as the Bam fault. The Bam fault is a mainly right-lateral strike-slip fault extending over 65 km with a strike of N8°-15°W passing through between the city of Bam and the town of Baravat (Jackson *et al.*, 2006; Fu *et al.*, 2007). Historical seismicity associated with the Bam fault is rather low as most earthquakes occurred on the Nayband and Gawk fault to the north and on the Jiroft fault to the south (e.g. Engdahl *et al*., 2006). The main geomorphologic expression of the Bam fault in the vicinity of Bam is a positive topographic feature known as the Bam-Baravat escarpment (BBE). The BBE is an asymmetric fold verging east with a steep eastern side and an almost flat top. It shows typical characteristics of a fold above a blind, west dipping reverse fault (Hessami *et al.*, 2005; Jackson *et al.*, 2006). Erosion of drainage channels in the uppermost layer of the escarpment and their lateral displacement suggest vertical slip rates of 1.4 to 2.5 mm/yr and a lateral slip rate of 2.6 mm/yr (Hessami *et al.*, 2005).

As first inferred from Synthetic Aperture Radar Interferometry (InSAR), the Bam 2003 earthquake ruptured a blind right-lateral strike-slip fault 5 km west of the BBE, south of the city of Bam (Talebian *et al.*, 2004). The main surface expression of this previously unmapped fault is a series of *en echelon* surface breaks each of length 50 to 100m with 20 cm maximum dextral offset. Coseismic deformation on this blind strike-slip fault has been measured and modelled by different remote sensing techniques (e.g. Funning *et al.*, 2005; Binet & Bollinger, 2005; Sarti *et al.*, 2006). However, surface deformation and seismic moment released in the main shock in the vicinity of Bam cannot be fully explained by a single fault model, leading to an open debate on the seismic hazard of the region (Talebian *et al.*, 2004; Perski & Hanssen, 2005; Funning *et al.*, 2005; Jackson *et al.*, 2006). Further field observations report small to medium scale fissuring (1 to 12 cm) along the BBE and along the pre-existing Bam fault trace indicating that the Bam fault has been involved in the surface rupture process (Talebian *et al.*, 2004; Hessami *et al.*, 2005; *Fu et al.*, 2007). Highlighting coseismic surface deformation along the BBE is then important information to better constrain coseismic deformation models and aftershock interpretations (Tatar

et al, 2005; Nakamura *et al*., 2005) in the Bam region. In this study, we focus on the BBE and we measure coseismic surface deformation on its northern segment, a few hundred meters from the city of Bam.

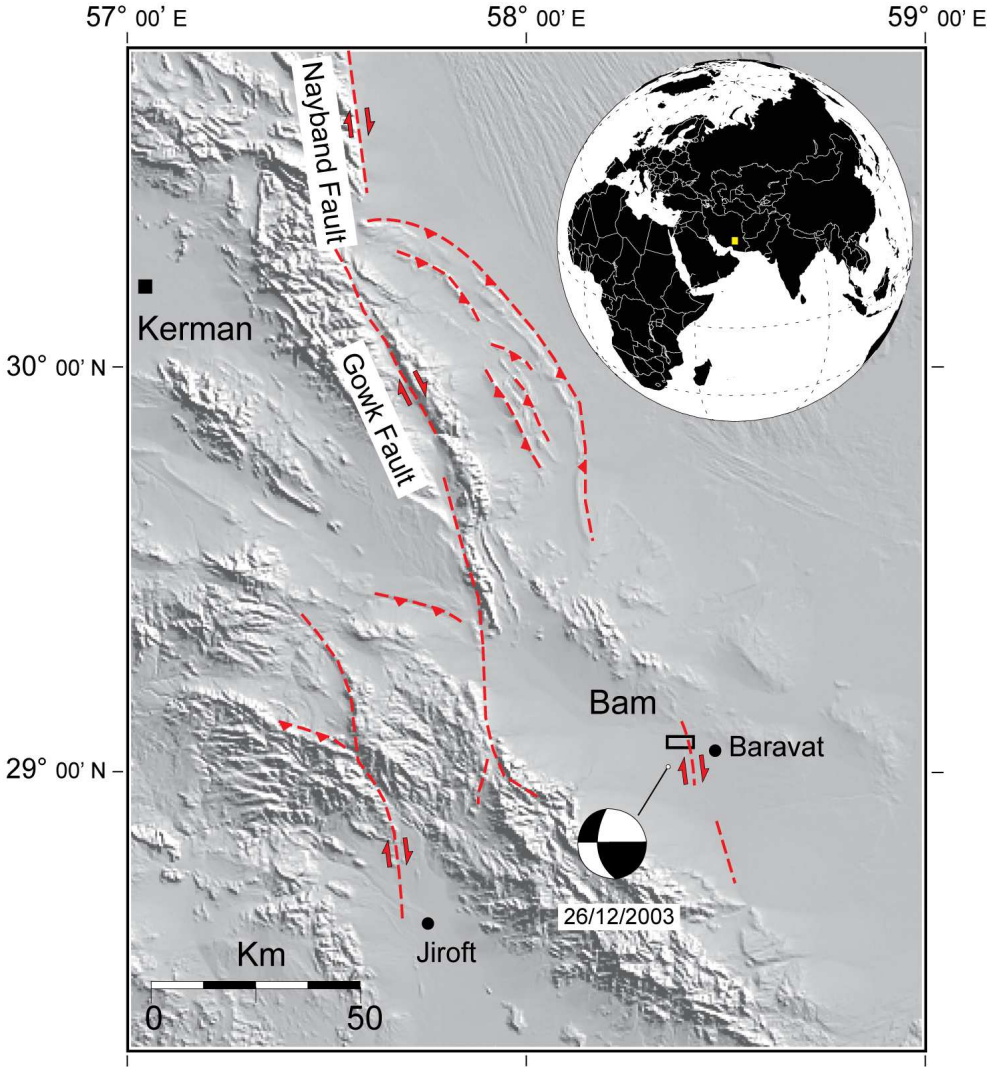

Figure 4.1. Geographic position of Bam, major faults of the area from Walker and Jackson (2002) and the 2003 earthquake mechanism from the Harvard CMT earthquake catalogue. The black rectangle indicates the study area shown in Figure 2.

Data

Two panchromatic Quickbird images and one SPOT-5 image are used in this study (Table 4.I). The two Quickbird images with 0.6 m spatial resolution were acquired before and after the 2003 Bam earthquake respectively (Figure 4.2). The SPOT-5 image with 2.5 m spatial resolution was acquired before the earthquake. Both the Quickbird and SPOT-5 images covering the City of Bam have been made available through the International Charter (http://www.disasterscharter.org) activated immediately after the 2003 earthquake.

Platform/Sensor	Acquisition	Date	Spatial resolution
SPOT-5/THR	Pre-seismic	16 Oct 2003	2.5 m
Quickbird/PAN	Pre-seismic	30 Sept 2003	0.6 m
Quickbird/PAN	Post-seismic	03 Jan 2004	0.6 m

Table 4.I. Satellite images used in this study.

There are three reasons for using the aforementioned satellite data. Firstly, the pixel size allows the retrieval of small-scale surface deformation through the analysis of sub-pixel offset. Secondly, the data are centred on the city of Bam. Therefore, we could investigate the area where differential InSAR measurements are not fully legible due to scarce temporal signal coherence owing to substantial urban building destruction (e.g. Hoffmann, 2007). Besides, the lack of numerous SAR data just before the earthquake does not allow multi-temporal analysis, which could partially overcome the coherence problem (e.g. Ferretti *et al.*, 2001). Thirdly, as the surface rupture observed by InSAR coherence and field observation does not propagate into the city of Bam, the chosen area is suitable for studying the deformation field of the BBE.

Methodology

Correlation of both panchromatic and radar amplitude images is a commonly used technique for the measurement of surface deformation (e.g Van Puymbroek *et al.*, 2000; Delacourt *et al.*, 2007). It has been proven to be complementary to InSAR in a number of geophysical studies (e.g. Klinger *et al.*, 2006; de Michele & Briole, 2007). In the method, images acquired before and after a deforming event are firstly resampled to a common map geometry (orthorectification) by the use of a Digital Elevation Model (DEM), a camera model and few Ground Control Points (GCP) either retrieved from the DEM or by the Global Positioning System (GPS).

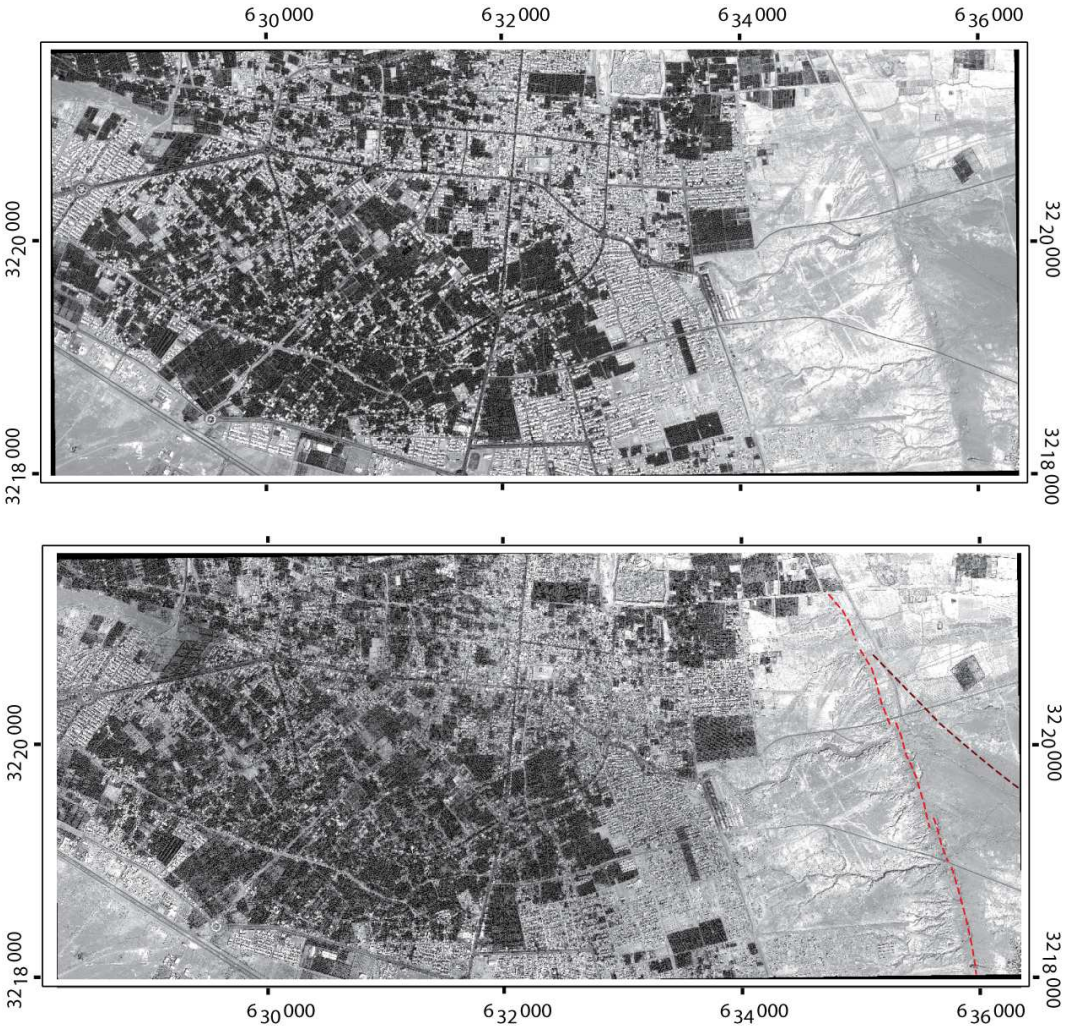

Figure 4.2. Pre-earthquake (above) and post-earthquake (below) Quickbird images centred on the city of Bam. UTM projection, zone 40. These are the panchromatic images used to retrieve coseismic deformation. The dotted red line represents the trace of the rupture along the BBE reported in Hessami *et al.* (2005) and Fu *et al.* (2007). The dark red dotted line represents a secondary fault trace deduced from interferometry by Perski & Hanssen (2005).

The aim of orthorectification is to minimize the pixel offset due to parallax between satellite images acquired from slightly different viewpoints. This offset contribution is proportional to topography (henceforth called topographic offset, ω_t). Once ω_t is removed, subpixel offset is calculated by means of a moving window. The residual offset between the two images is then expected to be due to surface deformation that occurred within the images' acquisition period.

The Quickbird camera model could be consistently used only if undertaking the orthorectification process on raw data (e.g. Robertson, 2003), which is not the case for the already geocoded data delivered through the International Charter. Moreover, no precise GPS points are available at Bam. Furthermore, the freely available 90 m Shuttle Radar Topography Mission (SRTM) DEM has too low a spatial resolution compared to Quickbird images to achieve high-precision orthorectification over a small area. Therefore, since standard methodologies (e.g Leprince *et al.*, 2007) might not be applied in our particular case, we adopt a different approach to model and remove ω_t.

We assume that ω_t and topography are linearly correlated over the relatively small study area. Then, we co-register the SPOT5 pre-event image and the Quickbird pre-event image using a 1st order polynomial assuming that the imaged area is small with respect to the distance between the spacecraft and the ground. Afterwards, we exploit the parallax between the co-registered images and retrieve ω_t from their calculated

offset. The Quickbird pre-event image is firstly degraded to 2.5 m spatial resolution to achieve the same spatial resolution as the SPOT5 image. As a result, we have:

$$\omega_{Qb1\text{-}Sp5} \cong \omega_{t1} + \nu$$

where $\boldsymbol{\omega}_{Qb1\text{-}Sp5}$ represents the offset calculated from pre-event Quickbird-SPOT5 images and $\boldsymbol{\nu}$ represents the noise component to offset measures due to random surface changes. After that, we calculate the offset from co-registered Quickbird pre-event post-event images ($\boldsymbol{\omega}_{Qb1\text{-}Qb2}$). This second offset contains both the topographic offset (ω_{t1}) and the offset due to coseismic deformation (ω_{def}). As a result, we have:

$$\omega_{Qb1\text{-}Qb2} \cong \omega_{t1} + \omega_{def} + \nu$$

where $\boldsymbol{\nu}_1$ represents noise. Between $\boldsymbol{\omega}_{t1}$ and $\boldsymbol{\omega}_t$ a linear relation exists, so that:

$$\omega_t \propto \omega_{t1}$$

In contrast, image offsets due to coseismic deformation are not linearly correlated with topography-related image offsets. Therefore, retrieving coseismic deformation from these two sets of offset data becomes a problem of separating un-correlated components from linearly-correlated datasets. We solve this problem through PCA.

The PCA, also known as the Karhunen-Loève transform, has already been used to extract correlated signals in geophysical data (e.g. Savage 1988). It resolves data that are simultaneously observed into a superposition of a number of signal components each of which are orthogonal and therefore independent (see Menke, 1989). Given the

matrix $\boldsymbol{\omega}$ as composed by input data bands $\boldsymbol{\omega}_{\text{Qb1-Sp5}}$ and $\boldsymbol{\omega}_{\text{Qb1-Qb2}}$, a PCA-transformed offset vector at the j^{th} pixel, $\mathbf{o}^{j}$, where

$$o = PCA(\omega)$$

is split into:

$$o^{j} = \sum_{i=1}^{n} \alpha_i^j \, \mu_i$$

where the calculation of μ_i is based on the diagonalization of the $\boldsymbol{\omega}$ correlation matrix. From here, we obtain un-correlated orthogonal functions where μ_i represents the i^{th} component of the orthogonal functions and $\alpha_i{}^{j}$ represents the coefficient, or weight, for the i^{th} component at the j^{th} pixel. The i^{th} component that contributes at maximum to the variance of correlated dataset is referred to as the first principal component among n input bands. In this study, PCA is calculated on the input data bands $\boldsymbol{\omega}_{\text{Qb1-Sp5}}$ and $\boldsymbol{\omega}_{\text{Qb1-Qb2}}$ so that the first principal component represents topographic offset in PCA space. Modeled this way, topographic contributions to the coseismic offset can be separated allowing the extraction of the offset due to coseismic deformation.

Results

We have measured offset between pre and post earthquake Quickbird images using an innovative approach such as the PCA applied to sub-pixel correlation. The results highlight coseismic surface deformation over the Bam urban area (Figure 4.3). In particular, we can observe an offset break striking ~N15°W along the BBE. The west

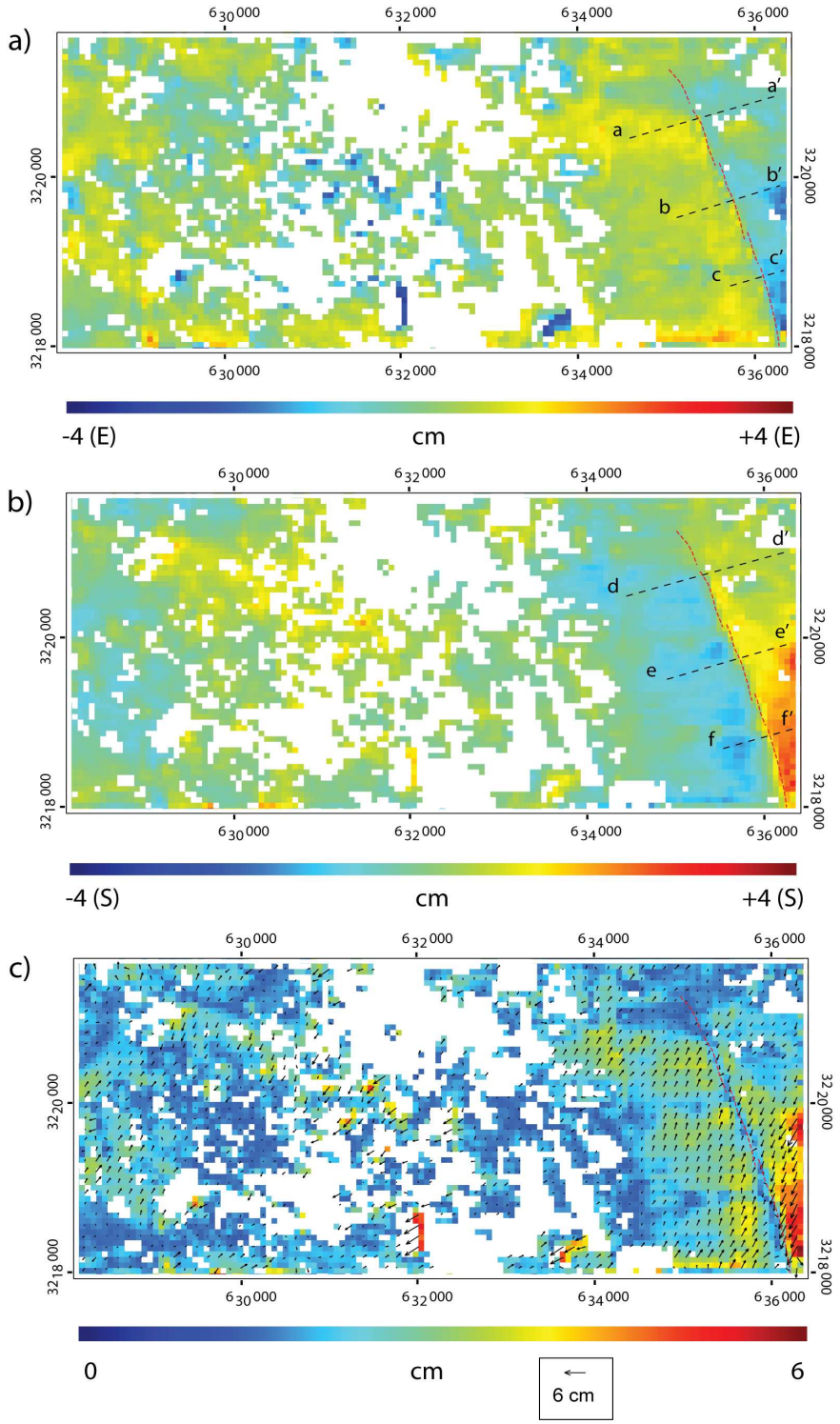

component of the offset break has an average magnitude of 2 cm (Figure 4.3a, Figure 4.4a, b, c) while the south component has a magnitude of about 2 to 6 cm (Figure 4.3b, Figure 4.4d, e, f), revealing a dextral strike-slip movement with possible minor

reverse component (Figure 4.3c). These results are consistent with both field observations reported in Hessami *et al.* (2005) and Fu *et al.* (2007) and the InSAR interpretation of Perski & Hanssen (2005). Coseismic surface deformation within the city of Bam is also highlighted, although that interpretation is made difficult by the complex deformation pattern since Bam lies close to the northern tip of the blind strike-slip fault detected by InSAR.

Figure 4.3. Coseismic correlograms showing the east offset a), south offset b) and offset absolute magnitude (colour scale) and direction (black arrows) in c). White pixels mask areas of poor correlation score. These results can be interpreted as a strike slip fault with a possible minor oblique reverse component whose surface projection corresponds to the fault trace mapped in the field by Hessami *et al.* (2005) and Fu *et al.* (2007) (dotted red line). Black dotted lines a-a', b-b', c-c', d-d', e-e' and f-f' indicate Figure 4 profiles location.

The sub-pixel correlation is calculated by the CNES (Centre National d'Etudes Spatiales) Medicis tools (CNES, 2003). We have used a 103 pixels window size. This yielded independent measures every 61.8 m. The offset measure is partly corrupted by temporal surface changes. This yields low correlation scores where severe building damage occurred between the two acquisition dates. Low correlation scores mainly affect the urbanized area of Bam therefore the offset measurement along the portion of the BBE in the desert is most reliable. In this study we do not take into account offset measures associated with a correlation score lower than 0.6 (white areas in Figure 3). The accuracy of the Medicis procedure is expected to be 0.1 pixels. Nonetheless, an empirical estimate of the offset signal to noise ratio (snr) measured on the offset data after PCA gives 0.01 pixels (0.6 cm) as the precision of our final measurements.

Discussion

Offset measured by correlation of very-high resolution satellite images and PCA reveals coseismic deformation along the northern segment of the BBE associated with the 2003 earthquake. It is the first time that surface coseismic deformation is imaged on the BBE. Our findings support the idea that the 2003 earthquake is the result of the activation of a complex fault system where part of the coseismic deformation is accommodated by the Bam-Baravat segment of the Bam fault (e.g. Perski & Hanssen, 2005). A full description and interpretation of the 2003 earthquake would need a comprehensive analysis of different data sources from seismology, geodesy and remote sensing.

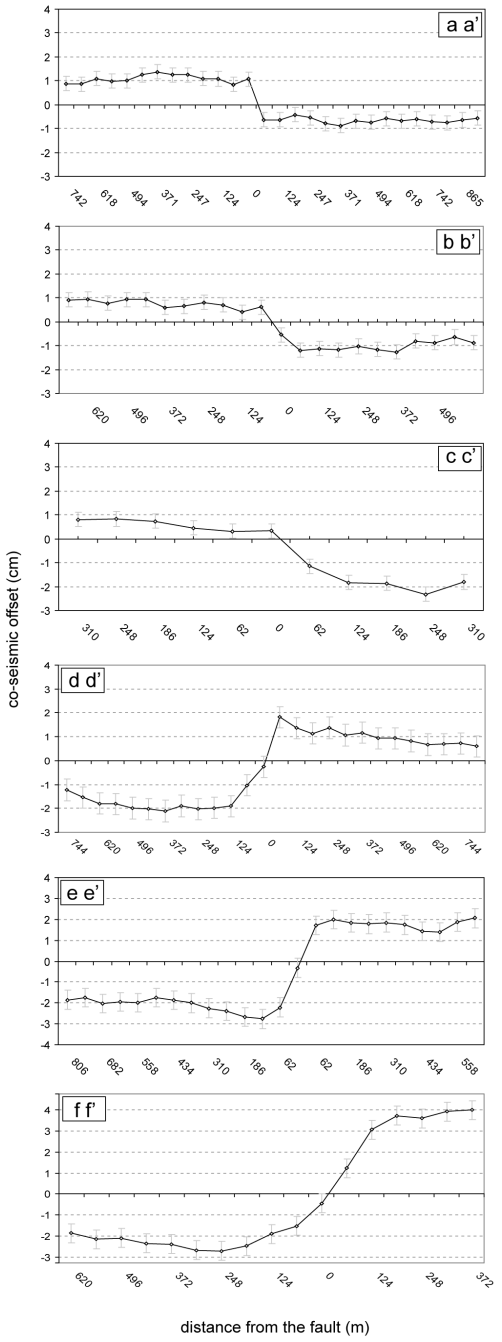

Figure 4.4. Offset distribution measured on the correlograms of figure 3 along the BBE (offset units are in cm). The offset break indicates reverse slip component of about 2 cm (a-a', b-b', c-c') and a dextral slip of 2 to 6cm (d-d', e-e', f-f') (refer to Figure 3 for profiles location).

An indirect validation of our results is provided by the work of Hessami et al. (2005) and Fu et al. (2007) who mapped

in the field fractures ranging from 1 to 20 cm along the Bam fault and the BBE following the earthquake.

We underline the complementarities between correlograms and interferograms. We focus on an area where part of the InSAR signal is incoherent and we measure the surface deformation field assumed by InSAR interpretations (Talebian *et al.*, 2004; Perski & Hanssen, 2005**;** Funning *et al.*, 2005; Jackson *et al.*, 2006). In particular, Funning *et al*. (2005) used modeling of InSAR data, seismology and geomorphology to suggest that the fault beneath the BBE slipped at depth. The observation that a small amount of surface slip occurred could better constrain this interpretive model.

The subtle centimetre-scale coseismic surface deformation on the BBE can be seen by InSAR although it is, undoubtedly, difficult to enhance. We suggest two possible explanations. Firstly, the subtle deformation along the BBE is masked by the larger deformation field produced by the blind strike-slip fault located 5 km to the west. Secondly, assuming that the deformation is mainly in the horizontal plane and considering the near North-South orientation of the fault, InSAR is essentially sensitive to the east slip component of the offset values which is about 2 cm. Considering the incidence angle of the SAR sensor ($i \approx 23°$) we can estimate that the SAR line-of-sight displacement is about 2 cm x sin$i$ (*i.e.* 0.8 cm), which results in 0.3 fringes in a C-band interferogram. This subtle quantity is difficult to discern by conventional differential InSAR because of potential residual topographic and atmospheric effects.

In nature topography and deformation are related since topography is often built by the complex interaction between repeated seismic events and erosion processes. The location of surface deformation can be associated with relief. However, the image offsets associated to a single coseismic event have different direction and distribution with respect to the topographic image offsets. We point out that in our study coseismic deformation represents the non-correlated component of two datasets having globally a partial linear correlation, one containing topography, the other containing both topography and deformation.

In conclusion, the application of PCA and the correlation of very-high-resolution satellite images to the Bam area allowed us to estimate centimetre-scale coseismic surface deformation. This novel methodology is a valid complement to InSAR and GPS processing over small areas as it has the potential to measure sub-pixel offset with 0.01 pixels precision. Another major advantage of this methodology is that it virtually does not require both the knowledge of the satellite camera parameters and the use of a DEM. In a next step, we plan to extend the investigation of coseismic deformation to other significant areas on the Bam fault using this novel approach.

Acknowledgments

The data used in this study were freely provided through the International Charter on Space and Major Disasters. The authors wish to thank the BRGM Direction of Research for funding this study. In addition, comments by Dr John Douglas and careful reviews by two anonymous reviewers were helpful and led to improvements to this article.

Chapter 5

Using InSAR for seismotectonic observations over the Mw 6.3 Parkfield earthquake (29/09/2004), California.

by Marcello de Michele [a], Daniel Raucoules, Jerome Salichon, Anne Lemoine, Hideo Aochi

[a] All the authors are with the Land Use Planning and Natural Risk division of the French Geological Survey (BRGM), Av. C. Guillemin, 45000 Orléans, France.

Foreword - This chapter represents our first approach on the use of InSAR on the San Andreas Fault at Parkfield. The use of InSAR on the Parkfield segment of the San Andreas Fault is the object on a ESA Category-1 research proposal. This chapter mainly resumes the work we made during 2007 at BRGM, that I presented at the 37th congress of the *International Society of Photogrammetry and Remote Sensing* held in Beijing in July 2008. The results are published as de Michele et al., 2008 in the *ISPRS proceedings.* This work marks my first publication in the InSAR domain, which theoretical basis I learnt at college and improved practically at Institute de Physique du Globe de Paris. In this chapter I chose to show only the published results that are constrained by the small allotted space. Consequently I don't show the numerical modeling efforts made by Jerome Salichon and Anne Lemoine whose intensive work I wish to acknowledge. The Parkfield segment of the San Andreas Fault is one of the main topics of this dissertation; I chose to show a further detailed InSAR study over Parkfield in the next chapter.

Summary

Across an earthquake cycle stress builds up along faults. The understanding of how stress builds up and when and where it is released is crucial in the understanding of the earthquake cycle. Remote sensing techniques offer a unique tool for detecting and quantifying deformations along active faults during the different stages of the seismic cycle. Synthetic Aperture Radar Interferometry (InSAR) provides a practical means of mapping movements along major active strike-slip faults. The InSAR archive allows the investigation of the history of past earthquake events, which may highlight possible precursors or triggering phenomena. We have applied InSAR techniques along with ENVISAT and ERS2 data on the Parkfield (US) 2004 earthquake of Mw 6.3. We focused on the co-seismic and on the pre-seismic InSAR signal and put into evidence the locked segment of the S. Andreas fault responsible for the 2004 Parkfield earthquake.

Introduction

Strain energy accumulating around a fault is periodically released as an earthquake. In contrast, some faults continue sliding aseismically due to different frictional behavior (Scholz, 2002). The San Andreas Fault Zone (SAFZ) particularly around the Parkfield area is of particular scientific interest mainly because of the short time-period earthquakes recurrence and because of the complex frictional fault behavior as a transition from stick-slip regime to aseismic creep (Bakun et al. 2005; Roeloffs and Langbein, 1994). Macroscopically, the San Andreas Fault shows simple fault geometry. Though, there exists a complexity such as segmentations on the surface trace which geometry plays an important role in the nucleation or stopping of the earthquake rupture (King and Nabelek, 1995). As reported for the previous 1966 Parkfield earthquake, it is important to know what makes the barriers or asperities and where they are located (Aki, 1979). Understanding the strain accumulation during the preseimic period is thus cru-

cial for the evaluation of seismic potential as earthquakes can occur according to the strain partitioning before the event (Weldon et al, 2005).

The San Andreas Fault, a rather mature transform fault, features different fault segments with different slip styles and rehological behaviour (Le Pichon et al, 2005; Fialko, 2006 ; Rosen et al., 1988). In particular, the Parkfield area in central California is referred to as a transition zone between two slip styles occurring under a common strike-slip faulting regime (e. g. Smith and Sandwell, 2006). The Parkfield area in the SAFZ (Fig. 5.1) is located at the boundary between a “creeping” fault segment to the north and a “locked” fault segment to the south (Toké and Arrowsmith, 2006). Our main interest is to make clear what happens in this region before the Parkfield earthquake in terms of strain history. In this study we use radar data acquired by the European Space Agency’s ERS1/2 satellites to form descending interferograms that individually record preseismic strain accumulation and subsequent coseismic strain release at the transition between the creeping segment and the locked segment of the SAFZ near Parkfield.

We analyze spatial pattern of the strain rate field and highlight preseismic strain accumulation along the fault trace. Analysing also the spatial pattern of the coseicmic deformation of the September 28 2004 earthquake, we study how the two iterferograms are correlated and namely how the earthquake rupture is characterized by the preseismic deformation.

InSAR evidence of pre-seismic strain accumulation

We have examined the preseismic deformation field recorded by space-based InSAR (Interferometric Synthetic Aperture Radar) in the Parkfield area. InSAR can map ground deformation at a decameter spatial resolution with sub-centimeters precision in the line of sight direction (LOS) (Massonnet and Feigl, 1998).

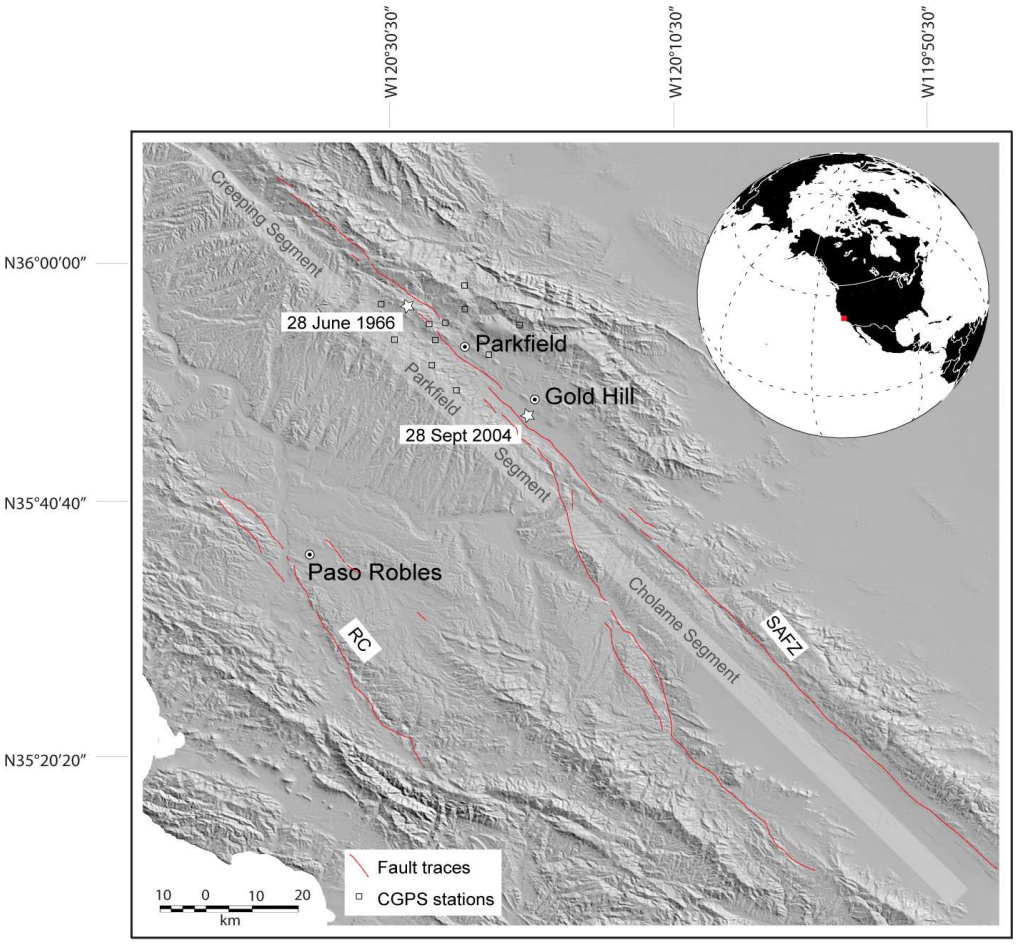

Figure 5.1. Map of the Parkfield region studied in this paper. It shows the location of major faults and continuous GPS sites. SAFZ stands for San Andreas Fault Zone and RC for Rinconada Fault. We plot the epicentres of the 1966 and 2004 earthquakes as white stars. Topography is from the Shuttle Radar Topography Mission (SRTM) (Farr et al., 2004) digital elevation model.

The San Andreas fault north of Parkfield undergoes continuous creep at an average rate of ~3 cm/yr (Toké and Arrowsmith, 2006). Atmospheric delays in the radar scenes of the interferometric pair (Zebker et al, 1997) could mask this kind of signal in a single interferogram. We therefore constructed the InSAR velocity field by averaging 30 selected unwrapped interferograms (Raucoules et al., 2003; Le Mouélic et al., 2005) calculated over the preseismic period 1993-2004, prior to the September 28

2004 earthquake. With this procedure, the effect of atmospheric delay is minimized as it is assumed to be uncorrelated with time.

Considering the simple mechanism of the strike-slip faulting regime of this region, we can rule out substantial contribution of vertical fault slip in this area of the SAFZ (Titus et al., 2006; Murray and Langbein, 2006) and assume that the InSAR signal is only due to horizontal surface fault slip. The result is, therefore, a velocity map (Fig. 5.2) showing right lateral shear distribution over 141 km of the San Andreas Fault centred in the Parkfield area prior to the 28 September 2004 earthquake.

A prominent feature of strain accumulation in the Gold Hill area highlighted in the preseismic interferogram stack is the abrupt spatial decrease of creeping rate along the SAFZ towards Gold Hill, where relative creep velocity reaches a local minimum (Fig. 5.3). This suggests either a change in the rheological material properties or a bend in the fault strike resulting in increasing friction towards Gold Hill. 30 km further south-east of Gold Hill, at the beginning of the Cholame segment, relative surface velocity increases to moderate values (~0.7 cm/yr) indicating the re-starting of surface creep. This spatially discontinuous change in the mode of slip suggests the presence of a stronger section of the fault between Gold Hill and Cholame that acts as a barrier locking the fault sub-segment south of Gold Hill. We will see further how this feature played a significant role in the nucleation of the 2004 Parkfield earthquake.

Subsidence due to water pumping in the Paso Robles sub-unit (Valentine et al., 1997) manifested as a bull eye shaped range change pattern south of Parkfiel is a marked feature in the presismic interferogram. Similar features though smaller in area can be observed in the northern sector of the preseismic interferogram (Fig 5.2). These correspond to petroleum and gas withdrawal from a shallow reservoir in the Lost Hills field and neighbouring reservoirs (Fielding et al., 1998, Brink et al., 2002).

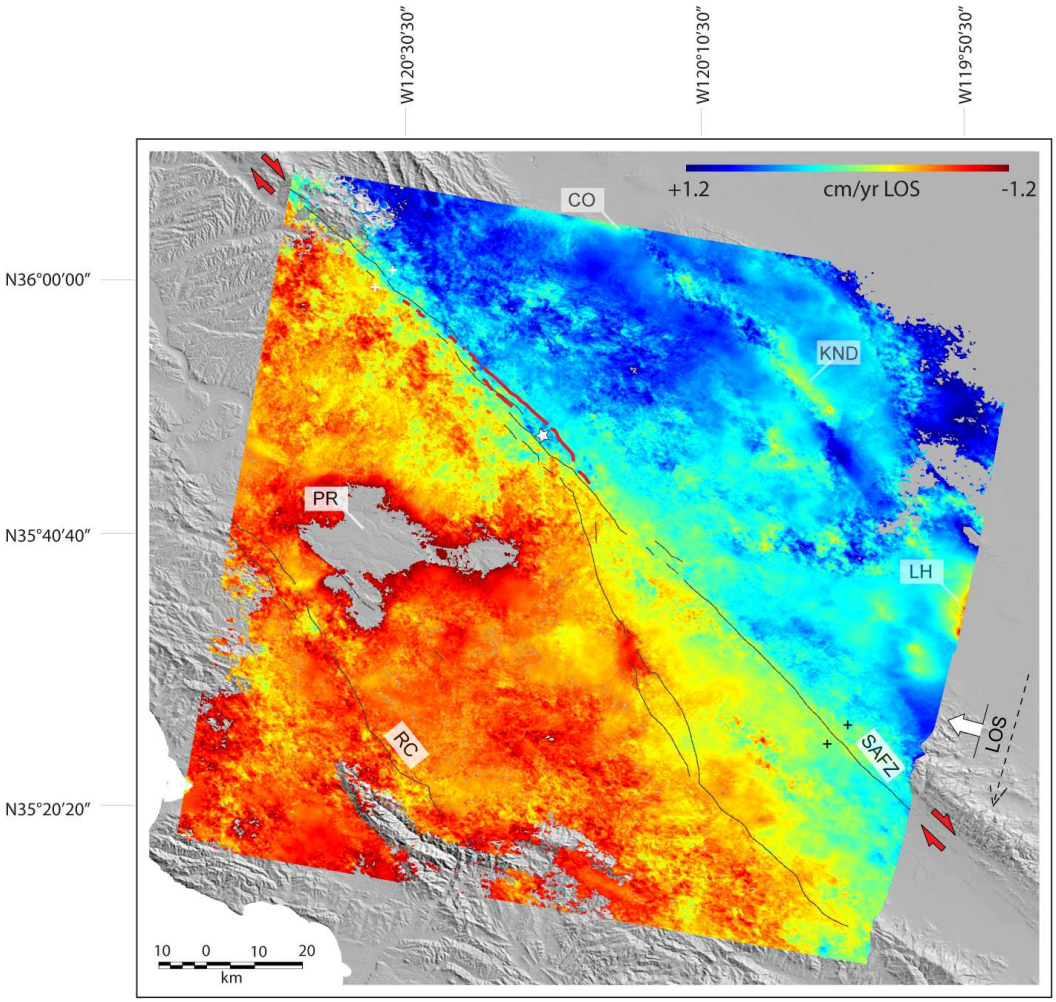

Figure 5.2. Preseismic strain buildup on the SAFZ at Parkfield. The map is composed by averaging 20 unwrapped ERS-1/2 interferograms in a stack. Each 20x20 m pixel is then a measure of the average LOS velocity in the period 1992-2004 prior to the earthquake. The scale-bar values represent centimeters parallel to the fault. To do this, we assume there are no vertical tectonic movements and we projected LOS velocity into the horizontal velocity component parallel to the fault strike. We plot 2004 earthquake rupture (in red) as well as the epicenter position (white star). CO=coalinga subsidence, LH=Lost Hills subsidence, KND=Kettleman North Dome subsidence, PR=Paso Robles subsidence. Black and white crosses indicate the position of the profiles used for extracting the differential profile in Figure 5.3.

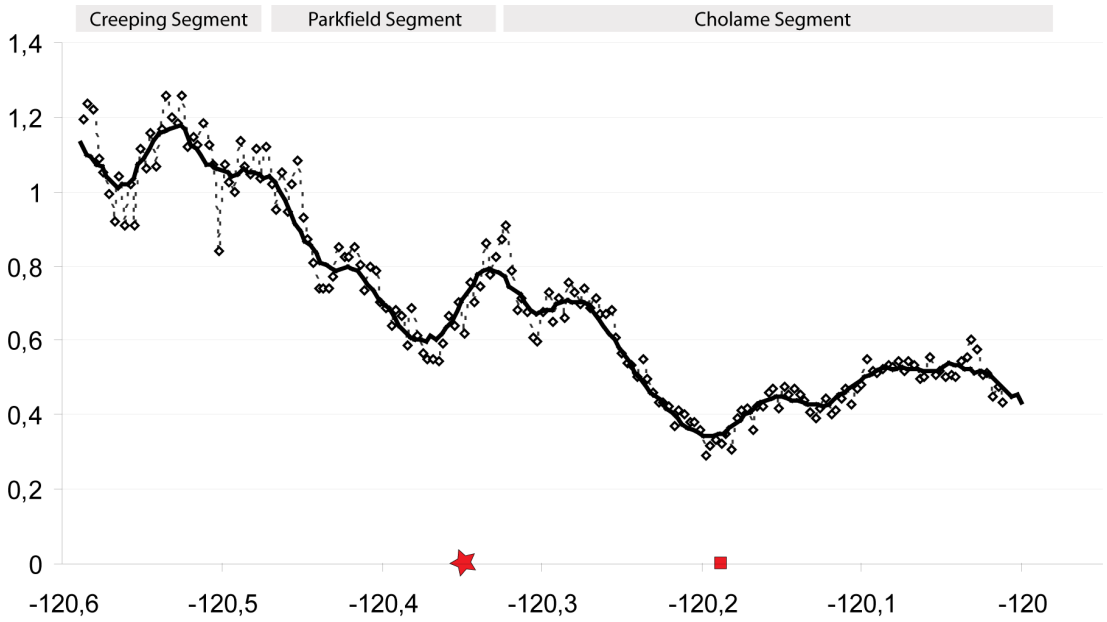

Figure 5.3. Differential velocity profile showing creep rate variation along the strike of the SAFZ (measured at ~1 km from the fault) during the preseismic period 1992-2004. We built this profile according to the methodology described in (de Michele and Briole, 2007). Notice the abrupt decrease in creep rate towards a local minimum south of Gold Hill where the future 2004 earthquake epicenter is located (red star). White squares represent minima in the preseismic creep rate profile indicating other possible stronger sections of the fault.

Pumping-induced vertical motion is a source of non-tectonic lateral signal inhomogeneities thus considered as noise for the purpose of our study. Moreover, such a transversal anisotropy in the deformation pattern is not considered by simple elastic dislocation models that rather assume the Earth's crust to respond as a laterally homogeneous and isotropic body. Therefore, no simple dislocation model is able to perfectly match hence explain our preseismic observations made with InSAR data. For the same reason we were not able to de-trend InSAR data by fitting a plane, whose estimation would be arbitrary. Our InSAR observations are therefore meant to be relative as are other geodetic techniques.

InSAR evidences of co-seismic strain release

We then used radar data from ERS-2 satellite to form interferograms that records co-seismic surface deformation of the September 28 2004 Parkfield event. The ERS-2 satellite experienced gyroscope failure in 2001. However, we could use 4 selected radar scenes among the ERS-2 dataset to construct coherent interferograms. Atmospheric phase contribution is a major limiting factor in the precision of a single interferogram. We minimize the atmospheric contribution to the coseismic signal by averaging two coherent coseismic interferograms spanning 950 and 490 days, respectively. It has to be noted that with such an important time lapse, aseismic deformation contributes significantly to interferometric signal in masking co-seismic deformation. Thus, we estimate aseismic phase contribution according to each time lapse from the aforementioned pre-seismic interferogram and remove pertinent aseismic contribution from each individual co-seismic interferogram before stacking. The results show a LOS spatially detailed coseismic surface displacement and provide a map of the surface that ruptured during the September 28 2004 Parkfield earthquake (Fig. 5.4).

We observe that the earthquake rupture extends from south of Gold Hill and ruptured North West toward Middle Mountain forming discontinuous breaks on the north western side of Cholame Valley, which is consistent with field observations (Rymer et al., 2006). We observe that the rupture developed along at least 35 km of the SAFZ. Coseismic surface deformation is consistent with a dextral strike slip mechanism. We measure maximum coseismic slip of up to 15 cm LOS, which makes ~21 cm horizontal displacement assuming that the vertical coseismic slip component is negligible. We compared our coseismic InSAR results with permanent GPS solutions ("http://www.usgs.gov" www.usgs.gov; Johanson et al., 2006). GPS permanent stations were installed in the framework of the Earthquake Prediction Experiment at Parkfield (Roeloffs and Langbein, 1994). InSAR results are briefly in good agreement with continuous coseismic GPS solutions that captured the coseismic signal about 20 km north-west of the epicenter.

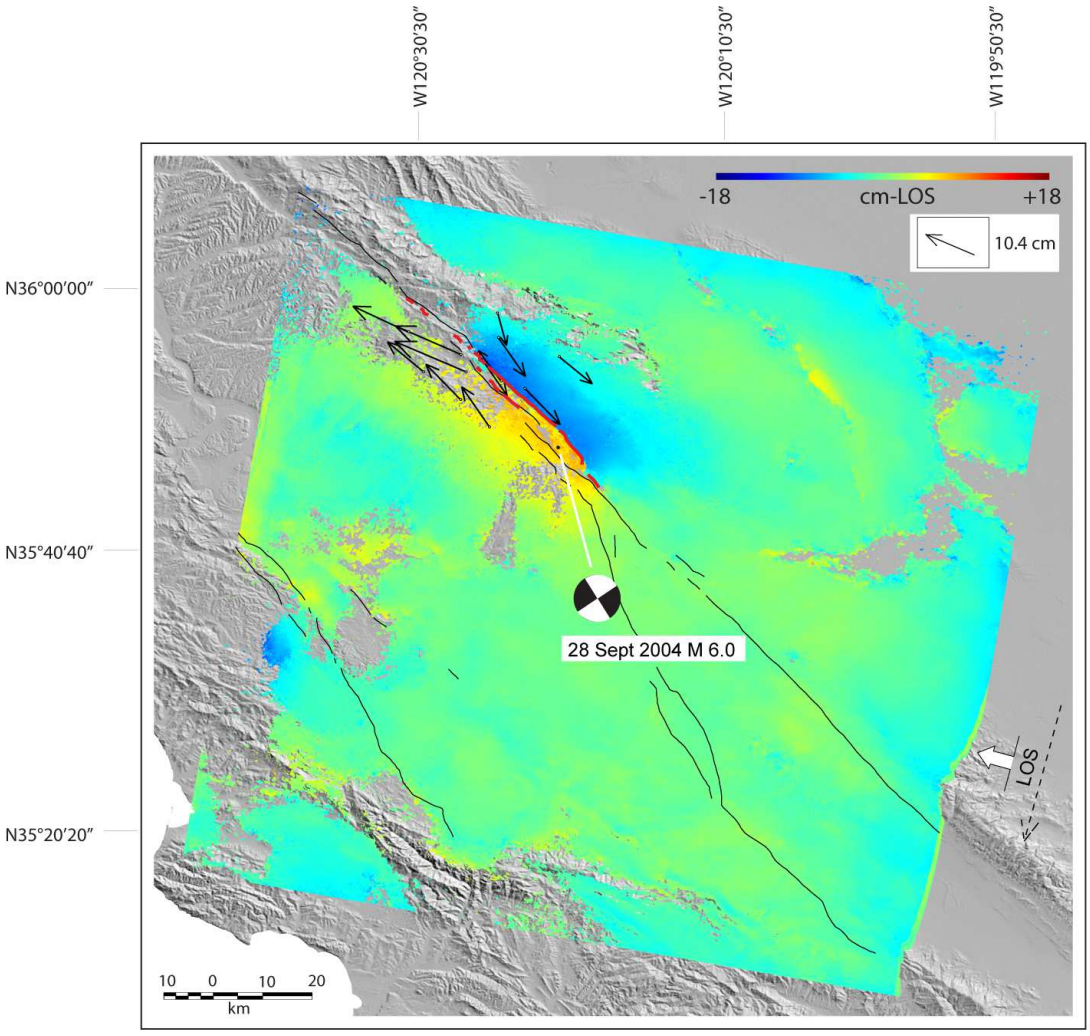

Figure 5.4. Unwrapped coseismic ERS-2 interferogram. Surface deformation in the LOS direction is consistent with a dextral strike-slip mechanism. The inferred surface rupture indicates northward propagation of the earthquake surface deformation as if a stronger section of the fault (-a barrier) limited dynamic propagation towards the south. We plotted coseismic GPS solutions from permanent stations for comparison (black arrows)

One of the most salient features in the co-seismic interferogram is the abrupt arrest of the rupture south of Gold Hill accompanied by a sharp transient in the surface deformation field. This observation implies the presence of a local structural control (Sibson, 1985) or earthquake barrier (Klinger et al, 2006) that may govern the propagation

(Aochi et al, 2005) and stopping of rupture as well as the propagation of surface deformation.

Discussion and Conclusions

The spatial pattern of the preseismic InSAR deformation rate (Fig. 5.2) indicates that strain distribution is not uniformly repartitioned along the fault strike. We observe that the spatially continuous abrupt decrease in the creep rate measured by preseismic InSAR data on the Parkfield segment of the San Andreas Fault reaches a minimum south of Gold Hill before gently increasing again. We notice how the preseismic surface deformation pattern highlights strain accumulating towards a stronger section of the San Andreas Fault south of God Hill. The identification and geographic location of an earthquake barrier or asperity is of major importance. Interseismic barriers might act as stress concentrators thus playing an important role in starting the earthquake rupture. It is known by seismological analyses that the 2004 rupture propagated northward unless the 1966 one. Our InSAR coseismic interferogram show how the surface rupture extends north of the epicenter on the SAFZ while south of Gold Hill the earthquake rupture bends abruptly and culminates. The InSAR coseismic deformation pattern follows the same trend as deformation lobes do not extend gently off the southern tip of the rupture as one would expect in a simple coseismic strike-slip shear regime. This is evidence of the presence of either structural or geometric features south of Gold Hill on the SAFZ that acted as a kinetic barrier opposing rupture propagation. The barrier is well localized at the transition between two different modes of aseismic slip on the SAFZ and it is geographically well correlated with the barrier assumed by observing strain accumulating in the preseismic interferograms stack. Therefore, we are spotting the location of a highly probable earthquake such as the 2004 Parkfield. In this case, our InSAR results would have helped the planning of ground instrumentation network in the vicinity of the future epicenter.

Long wavelength lateral signal heterogeneities partly due to subsidence phenomena observed in the preseismic interferogram hamper simple elastic modelling of preseismic strain build-up.

We jointly interpret preseismic and coseismic InSAR observations as evidences of the presence of a local structural/geometrical control that governs strain accumulation and consequent earthquake nucleation. We conclude that the spatially detailed constructed SAR interferograms have the capability to highlight inhomogeneities in the strain history of a region and allow us to identify the area of potential earthquake nucleation.

Acknowledgements

SAR data have been made available by ESA though the CAT-1 project proposal. Authors wish to thank BRGM research division for funding this study.

Chapter 6

Spatiotemporal evolution of surface creep in the Parkfield region of the San Andreas Fault (1993-2004) from Synthetic Aperture Radar.

by Marcello de Michele [a], Daniel Raucoules [a], Frederique Rolandone [b], Pierre Briole [c], Jerome Salichon [d], Anne Lemoine [a], Hideo Aochi [a]

a French Geological Survey (BRGM), 3 Av. C. Guillemin, 45060 Orléans cedex 2, France.

b Laboratoire de Tectonique, CNRS UMR 7072, Université Pierre et Marie Curie -Paris VI, 4, Place Jussieu, Paris Cedex 05, France.

c Laboratoire de Géologie, CNRS UMR 8538, Ecole Normale Supérieure, 24 Rue Lhomond, 75231 Paris Cedex 05, France.

d Institut National des Sciences de l'Univers, Géosciences Azur, UMR-6526,

250 rue Albert Einstein, Les Lucioles 1, Sophia Antipolis, 06560 Valbonne, France.

Foreword - This chapter is an improvement of the previous chapter. Encouraged by the previous InSAR results on the Parkfield segment of the San Andreas Fault, we decided to go further in the data analysis. In particular, we want to improve the precision of the measurements and better investigate the InSAR signal in the Cholame segment. We do a number of processing steps in order to

remove at best any signal due to atmospheric contribution to the interferometric signal. We concentrate only on the inter seismic phase of the seismic cycle at Parkfield and we decide to use a multi baseline approach that enable us to retrieve time series of surface displacement. We compare our results with micro seismic activity and we propose an unconventional way of visualizing the time series. This work arises more questions in terms of seismotectonics that it answers to. At the moment, the results presented in this chapter are not published. We are actually preparing a manuscript to be submitted by the end of September 2010.

Introduction

The San Andreas Fault system is a complex array of late Cenozoic right- and left-lateral strike-slip faults that accommodates motion between the North American and Pacific plates. It stretches between Cape Mendocino to the north and the Gulf of California to the south (Powell, 1993; Wallace, 1990). The San Andreas Fault features different fault segments with different slip styles and rheological behaviour (e. g. Steinbrugge and Zacher, 1960; Allen, 1968; Wallace, 1970; Thatcher, 1990). In particular, the Parkfield area in central California is referred to as a transition zone between two slip styles occurring under the common dextral shear regime (e.g. Harris and Archuleta, 1988; Lienkaemper and Prescott, 1989; Smith and Sandwell, 2006). The Parkfield area in the San Andreas Fault Zone (SAFZ) (Fig. 6.1) is located at the boundary between a "creeping" fault segment to the northwest, which slips steadily at a rate of 25-30 mm/y (Whitten and Claire, 1960; Bennett, 1979; Burford and Harsh, 1980; Lisowski and Prescott, 1981; Schulz et al., 1982; Titus et al., 2006; Toké and Arrowsmith, 2006) and a "locked" fault segment to the southeast, which last ruptured in the 1857 M_w 7.9 Fort Tejon earthquake (McEvilly et al., 1967; Sieh, 1978). Furthermore, the Parkfield area on the SAFZ is of particular scientific interest because of the occurrence of earthquakes with short recurrence times (e.g. Roeloffs and Lang-

bein, 1994; Bakun et al, 2005) and because of the complex frictional fault behavior as it represents a transition zone from stick-slip regime to aseismic creep. Therefore, it is of great interest to measure and analyze not only the spatial evolution of surface displacement in this area but also its relation or dependency to time. The Parkfield area on the SAFZ is very well instrumented on the ground but south of Parkfield ground

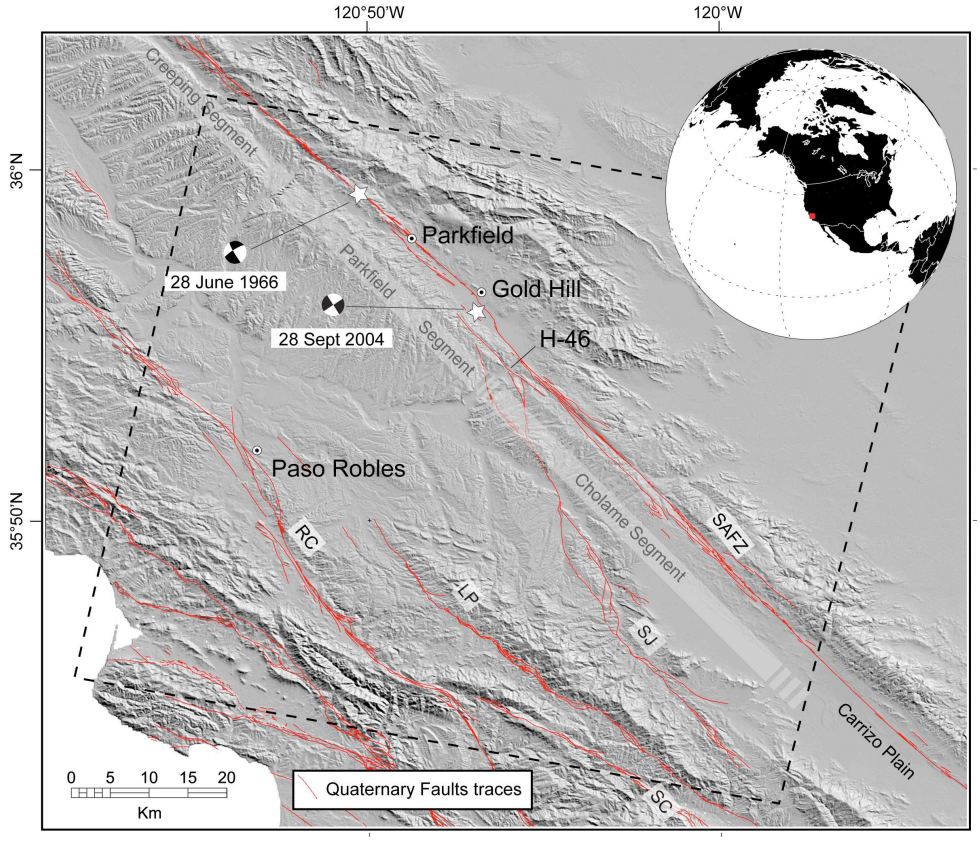

Figure 6.1. Map of the Parkfield region of the SAFZ. It shows the location of major faults (after USGS). SAFZ stands for San Andreas Fault Zone, RC for Rinconada Fault, SJ for San Juan Fault Zone, LP for La Panza Fault and SC for South Cuyama Fault. H-46 stands for Highway 46. We plot the epicentres of the 1966 and 2004 earthquakes. Creeping, Parkfield and Cholame segmentation is drawn following Toké and Arrowsmith (2006). The black dotted line represents the ground swath shared by the ERS1-2 radar scenes. Topography is from the Shuttle Radar Topography Mission (SRTM) (Farr et al, 2004) digital elevation model.

instrumentation is sparse. InSAR technology has the capability to retrieve Earth surface motion from space, virtually without the need of ground instrumentation. Therefore, it is of great complement to ground based techniques especially where the latter are sparse of totally absent.

Presently, no InSAR studies have been performed on the interseismic period before the 2004 Parkfield event (Mw 6.0) in the Parkfileld area of the SAFZ. In this manuscript we present the analyses of the multitemporal InSAR signal in the Parkfield region that we use to analyse the strain history of the SAFZ in the period 1993-2004. In particular, we focus on characterising the space and time evolution of surface creep on the Parkfield and Cholame segment of the SAFZ. To this aim, we use radar data acquired by the European Space Agency's European Remote Sensing (ERS1-2) satellites to form descending interferograms that we combine to retrieve time series of surface displacement. In the following paragraphs, we discuss the methodology and present the main results of this study.

Methodology

On the SAFZ, a number of teams have used InSAR to detect aseismic slip (e.g. Rosen et al., 1988; Lyon and Sandwell, 2003; Johanson and Burgmann, 2005) or strain build-up (Fialko, 2006), Lundgren et al. (2009). For instance, Ryder and Burgmann (2008) improved the results of Rosen et al. (1998) by stacking 12 differential interferograms spanning 1992 to 2000 to measure the spatial variation in the slip deficit on the creeping segment of the SAFZ, northwest of Parkfield. On the other hand, on the transitional segment of the SAFZ, between Parkfield and south of Cholame, where shallow slip is assumed to fade from steady creep to locked conditions, there are no multitemporal InSAR studies. We have examined the inter-seismic displacement field recorded by space-borne ERS1-2 InSAR in the Parkfield area over the 1993-2004 period. Prior to 2004 this area lacked major earthquakes since 1966 and given the short time period earthquake recurrence of this area, an event was expected (Bakun and

McEvilly, 1984; Roeloffs and Langbein, 1994). InSAR can map ground deformation at a decameter spatial resolution with sub-centimeters precision in the Line Of Sight direction (LOS) of the satellite (e. g. Massonnet and Feigl, 1998). We acquired all the ERS1-2 archived data available on the Parkfield area. We chose the descending mode to improve InSAR LOS sensitivity to strike-slip surface movement that is a function of the relative orientation between the platform flight direction and the fault strike (i.e. the LOS sensitivity to strike-slip surface movement goes to a minimum when satellite orbit and fault strike directions are parallel to each other). The San Andreas Fault undergoes continuous creep at an average rate of ~2.5 cm/yr north of Parkfield and ~l cm/y around Parkfield (e. g. Toké and Arrowsmith, 2006; Schulz et al., 1982; Titus et al., 2006). Atmospheric delays in the radar images of the interferometric pair could mask this kind of signal in a single interferogram (Zebker et al, 1997; Puysségur et al., 2007). To reduce atmospheric influence on the interferometric phase, we apply a methodology widely known as Small Baseline Subset (SBAS –Berardino et al., 2003) that was firstly conceived by Usai et al. (1999) and developed in a number of studies (e.g. Lundgren et al., 2001, Usai, 2003; Le mouelic et al., 2005; Lundgren et al., 2009). This method is implemented in the GAMMA software with the name of Multi-Baseline (MB) (Wegmüller et al., 2009).

We start from a set of 51 Single Look Complex (SLC) ERS data and we calculate 341 differential interferograms with a perpendicular baseline smaller that 250 meters. Topographic contribution to the interferometric phase is calculated for each interferogram starting from the Shuttle Radar Topography Mission (SRTM) Digital Elevation Model (DEM) and subtracted. Among the 341 differential interferograms, we retain a subset of 170 high coherence interferograms, based on visual analysis. Then we use the GAMMA Minimum Cost Flow (MCF) algorithm to unwrap these selected interferograms (Costantini and Rosen, 1999; Werner et al., 2002). For each interferogram, the unwrapping is improved by the use of a phase reference model obtained by unwrapping the multi looked interferogram followed by resizing of the unwrapped interferogram to the original resolution. For each pixel the unwrapped phase value is set to

the value which is within the interval (±π) of the provided model and which is consistent with the complex valued interferogram in the sense that re-wrapping of the unwrapped interferogram will result in the original interferogram phase value, except for a constant phase offset (Werner et al., 2002).

Even though in the study region the atmospheric phase delay is not as exacerbated by extraordinary relief as reported elsewhere (e.g. Elliot et al., 2008), depending on atmospheric conditions there might exist an altitude dependence of the path delay with respect to altitude caused by changes in the atmospheric water vapour and pressure profiles between the acquisitions of the interferometric image pairs (e. g. Doin et al., 2009). Therefore, we determine the linear regression coefficients of the residual phase with respect to height in the unwrapped interferograms using the DEM (in radar geometry) and generate the phase model of the height dependent atmospheric phase delay for each unwrapped interferogram. Each phase model is subtracted from the corresponding single interferogram. At this stage, we apply the MB algorithm. The MB algorithm uses the weighted least square method to generate a times-series of unwrapped deformation phases given a multi-temporal reference stack of unwrapped phases primarily due to deformation. The implicit idea is that the total deformation phase at time t_n is the sum of deformations from t_0 to t_1, from t_1 to t_2 and from t_{n-1} to t_n (Usai 2003). Lienkaemper and Prescott (1989) observed that after the 1966 earthquake after-slip, aseismic slip has been nearly constant on the Parkfield segment. Titus et al. (2006) reported that average surface creep rates have not systematically changed over course of the last 40 years. Although the slip rate at Parkfield for the period 1993-2004 may not be representative of the inter-seismic rate (e.g. Langbein et al., 1999; Nadeau and McEvilly, 1999) the first order assumption that the shallow aseismic slip pattern has a nearly constant average rate over the observed period motivates the use of the MB derived times-series of unwrapped deformation phases to derive a linear velocity map from linear regression on the time series at each image pixel (Fig. 6.2). The linear velocity map is by definition atmospheric-contribution free

as potential residual atmospheric contributions are supposed to behave non-linearly with time.

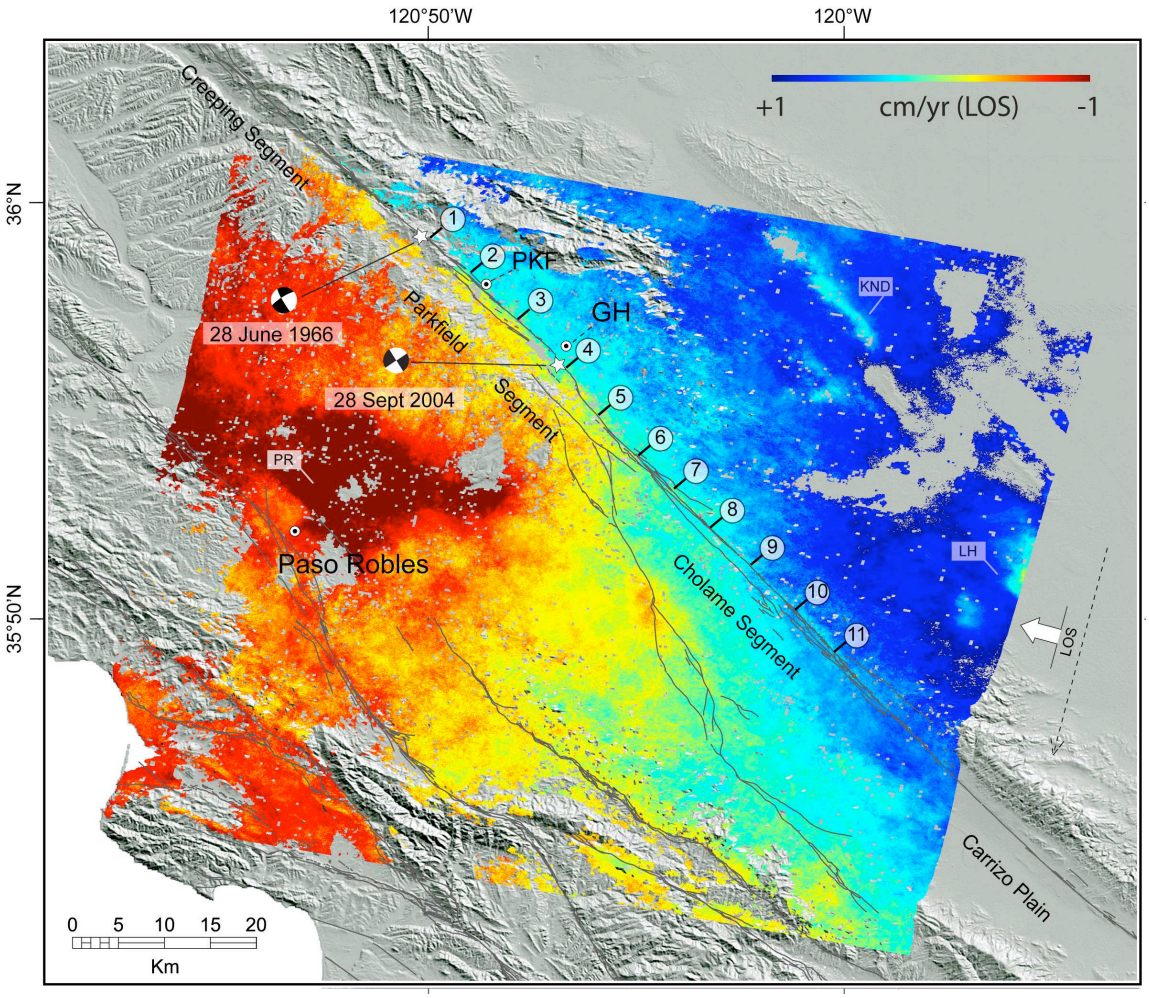

Figure 6.2. Linear surface displacement rate in period 1993-2004, in the LOS direction of the satellite. Negative values represent surface displacement away from the satellite. Positive values represent surface displacement towards the satellite. Tectonically, this figure represents inter-seismic strain build-up on the SAFZ in the Parkfield area before the 2004 earthquake. 2004 and 1966 earthquake epicentres (white star) are plotted. Numbered circles from 1 to 11 represent the location where we measured the time series of figure 4. This image shows also subsidence of non tectonic origin. CO=coalinga subsidence, LH=Lost Hills subsidence, KND=Kettleman North Dome subsidence, PR=Paso Robles subsidence. Pk stands for Parkfield, GH for Gold Hill.

Considering a simple mechanism of the strike-slip faulting regime of this region, we can rule out a substantial contribution of vertical fault slip in this area of the SAFZ (e.g. Titus and De Mets, 2006; Murray and Langbein, 2006) and we assume that the InSAR signal in figure 2 is mostly due to horizontal surface slip, constant in time. *De facto*, a small amount of normal convergence exists in central California and it is mainly accommodated by contractional structures such as thrust faults and folds in the California Coast Ranges (e.g. Rolandone et al. 2008).

Besides, in order to highlight possible time variable creep phenomena, we extract 11 time series of surface displacement along the SAFZ from Parkfield to south of Cholame. The time series are time-filtered to remove eventual un-modeled residual atmospheric contributions to the interferometric phase. We take measurements at an average of 1.5 km distance from the fault. Time series refer individually to a fixed North American plate in the sense that each of the 11 time series is referred to a given reference time series that is symmetrically measured 1.5 km on the north-eastern sector of the SAFZ on the Pacific Plate (Fig 6.4). We underline that we do not make use of any particular *a priori* model of surface displacement in any of the processing steps described above.

Results and discussion

Figure 6.2 shows the linear displacement rate over 1993-2004 measured in the LOS direction of the sensor (23° on the vertical). The bimodal distribution of surface displacement enhances dextral shear. From ~25km north of Parkfield to ~15 km south of Gold Hill (Highway 46) we notice a sharp discontinuity in the InSAR data reasonably due to the steady component of surface creep, well localised on the SAFZ. The sharp discontinuity seems to fade progressively from NW to SE along the SAFZ possibly indicating that shallow creep evolves towards more diffuse surface displacements. We want to concentrate on the close SAFZ field (± 1.5 km form the fault trace) and quantify the along-strike spatial evolution of the linear surface displacement by taking a

number of measurements along strike based on figure 6.2. We took measurements according to the methodology proposed by Avouac et al. (2006) and Leprince et al., (2007) i. e. on stacked transversal-to-the fault profiles. Each measure represents the velocity of a cluster of pixels at 1.5 km south of the SAFZ relative to the velocity of a cluster of pixels 1.5 km north of the SAFZ (Fig 3). We compare our results with historical records available from Short Range Electronic Distance Measurements (Bennett, 1979; Lisowski and Prescott, 1981), creepmeters (Schulz et al., 1982) and alignment array surveys (Burford and Harsh, 1980; Titus et al., 2006) at same locations along strike on the SAFZ. Within a certain degree of precision, we can see that the InSAR profile retrieves the general trend of spatial evolution of surface creep captured by ground measurements. According to Lisowski and Prescott (1981), there is no difference between surface creep rates measured using 100-to-200 m-wide alignment arrays and those from the 1-to-2 km-wide Short Range EDM located in the same area along the SAFZ. Therefore, we could be relatively confident that the profile in figure 3 effectively samples surface creep and that the observed surface creep rate decreases from ~1.4 cm/yr north of Parkfield to zero at about ~12 km south of Highway-46. From this point on for ~10 km, surface creep rate is about zero. Surface creep rate seems to increase up to 0.2 cm/yr in the Cholame segment north of the Carrizo plain (this observation is supported by one ground measurement by Schulz et al., 1982). This drop in the creep rate might highlight a stronger section of the fault at depth. We therefore compare the spatial evolution of surface creep with microsismicity catalogues from the Northern California Earthquake Catalog and Phase Data (www.ncedc.org, 2010) over the same period of observation as the InSAR (Fig. 6.3). Surprisingly there is a nice spatial correlation between micro-earthquakes location at depth and the presence of surface creep. Is there a correlation between earthquake magnitude at depth and the dynamic of surface creep? Does surface creep evolves linearly with time (steady creep) or are we facing episodic creep or stick-slip phenomena? How this correlates with microsismicity?

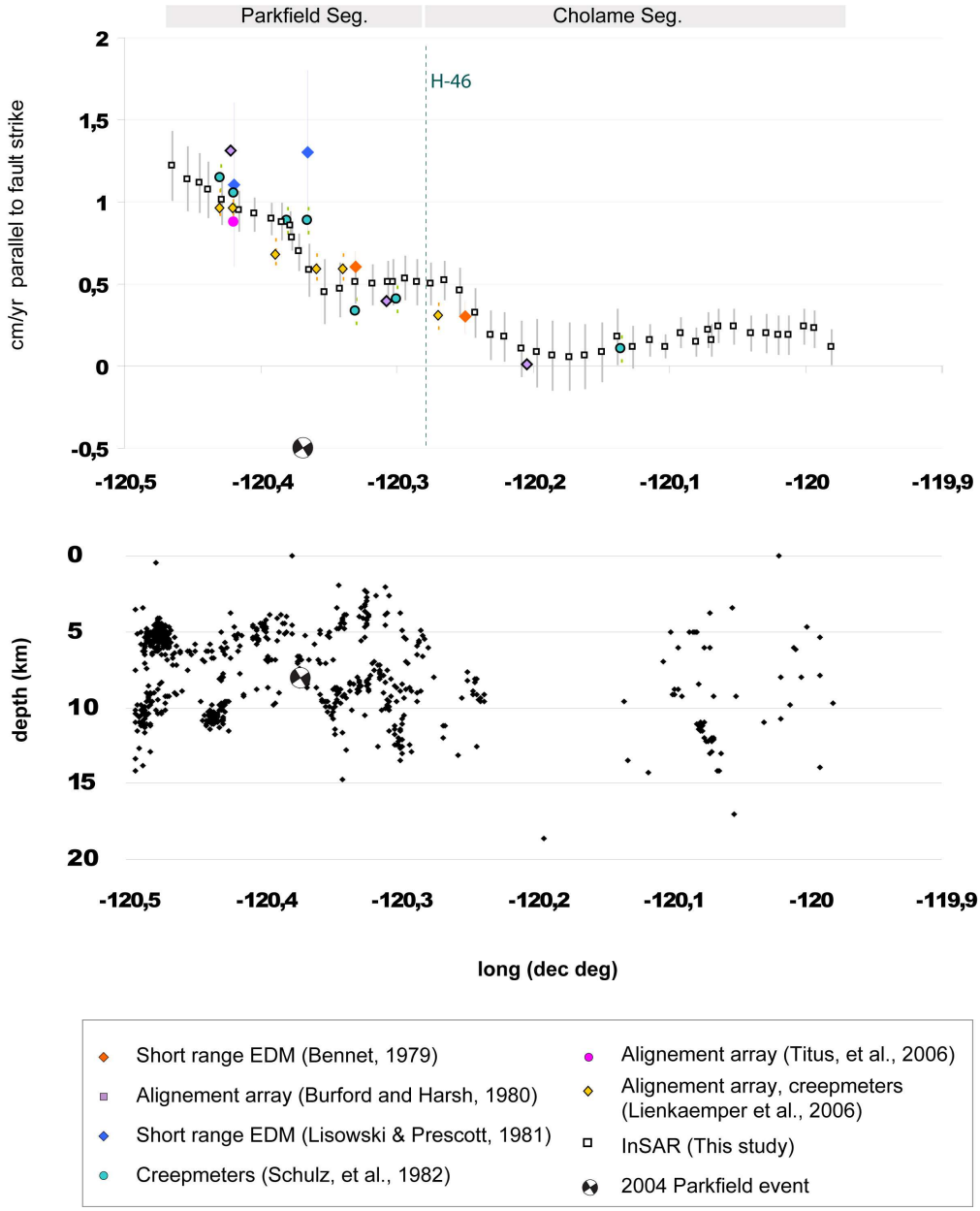

Figure 6.3. On top: Profile showing the linear surface displacement rate along strike of the SAFZ, form north of Parkfield to South of Cholame (longitude 120W) in the period 1993-2004 from InSAR (values are in cm/yr, projected horizontally and parallel to the Fault strike). InSAR values are compared from historical records from EDM, alignment array and creep meters. The focal mechanism showing the location of the 2004 Parkfield earthquake is plotted. Bottom: seismicity (1993-2004) plotted as longitude versus depth (source: NCEDC).

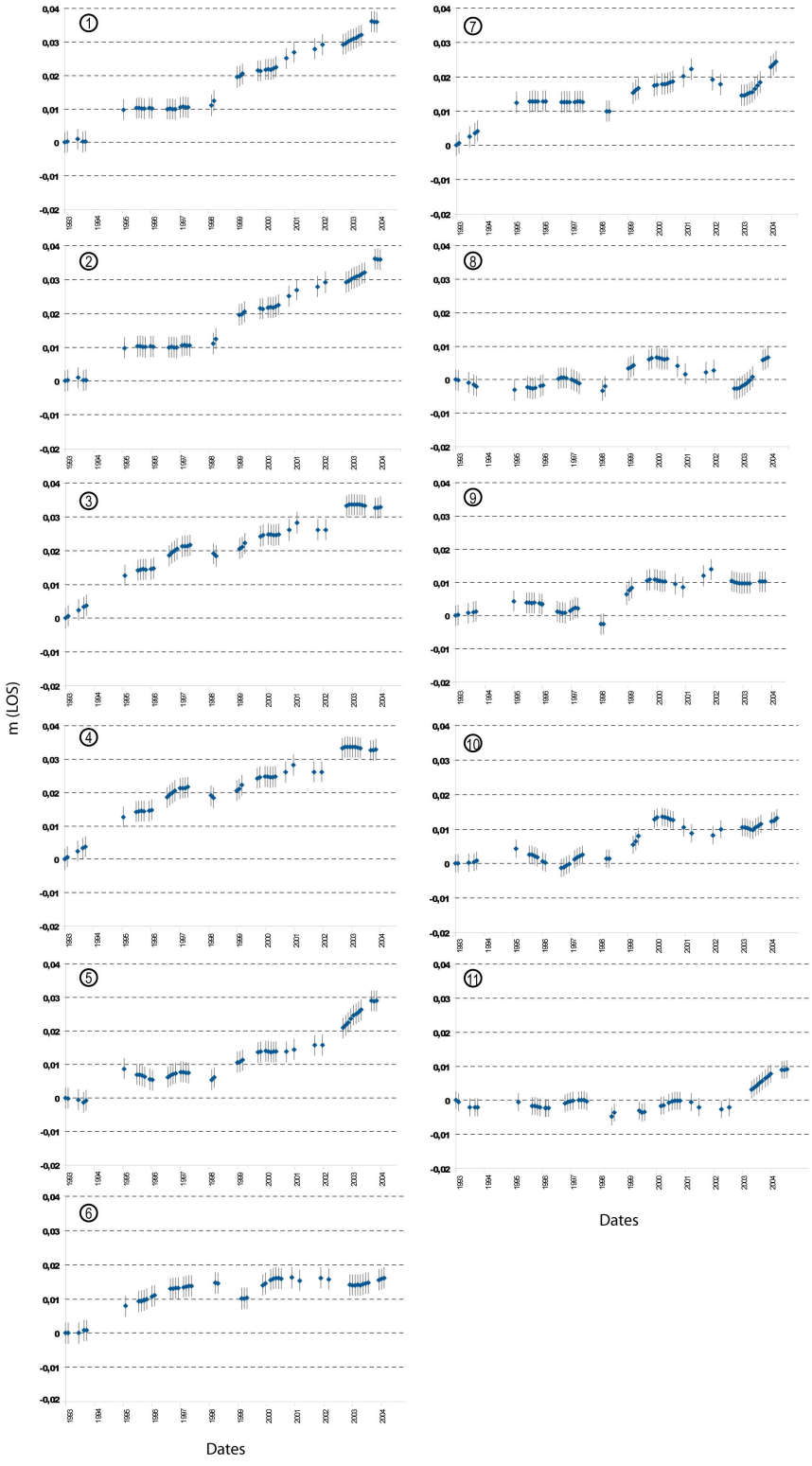

Figure 6.4. Time series extracted at location 1 to 10 (see figure 2). They show the temporal evolution of surface displacement within ±1.5 km from the main trace of the SAF. They refer to a fixed North American plate.

By looking at the time series from point 1 to point 11 (Fig. 6.4) we notice that the dynamic of surface creep on the SAFZ is complex. It seems that there is an alternation of periods of episodic creep to periods of steady state creep resulting in time and space variable local creep rate.

Is micro-seismicity the driver of these changes in the spatiotemporal creep behaviour? In figure 5 we present a way to visualise the spatiotemporal evolution of surface creep from InSAR and compare it with the spatiotemporal distribution of micro-earthquakes (and their magnitude) from north of Parkfield to south of Cholame. Four remarkable features stand out from figure 6.5. Firstly, surface creep evolves non-linearly neither in space nor in time. Secondly, surface creep occurs where seismic activity exists at depth. Notice that there is a microseismicity gap around 120.16 longitudes where cumulative surface creep is minimum (as also highlighted in figure 6.3). Thirdly, cumulative surface creep seems to be more pronounced where seismic activity is higher at depth. Lastly, the Cholame segment of the SAFZ experience episodic creep at the surface and manifests diffuse microsismicity at depth. Is the behaviour of surface creep driven by microsismicity on this segment of the SAFZ? Is there any relationship between seismic moments at depth and surface creep? If yes, is there a particular threshold on cumulative seismic moment that onsets episodic creep at the surface? By calculating the first derivative of the spatiotemporal evolution of surface creep of figure 6.5, we try to put into evidence local changes in the slope of the time series representing local changes in creep rates (accelerations). We show these results in figure 6.6, where we compare local changes in the slope of the time series with microsismicity. With figure 6.6 we gain twofold information. Firstly, we can observe pulses of surface displacement corresponding to episodic creep at the surface and we can localize them easily along strike on the SAFZ between north of Parkfield and south of Cholame. Secondly, we notice the lack of apparent correlations between microsismicity and increase of creep activity. The lack of correlation is highlighted in figure 6.6b, where we plot the mean temporal evolution of surface creep on a 30 km segment from Parkfield to Highway-46 versus the temporal evolution of slip at depth calculated from the seismic moment (that is the spatial integral of slip multiplied by the rigidity, Kanamori, 1977) on a 30 km long fault segment extending from the surface to the bottom of the seismogenic layer (20 km). Slip at depth is characterised by repeating microearthquakes (Md 3.9-4.9) and a typical stick slip dynamics.

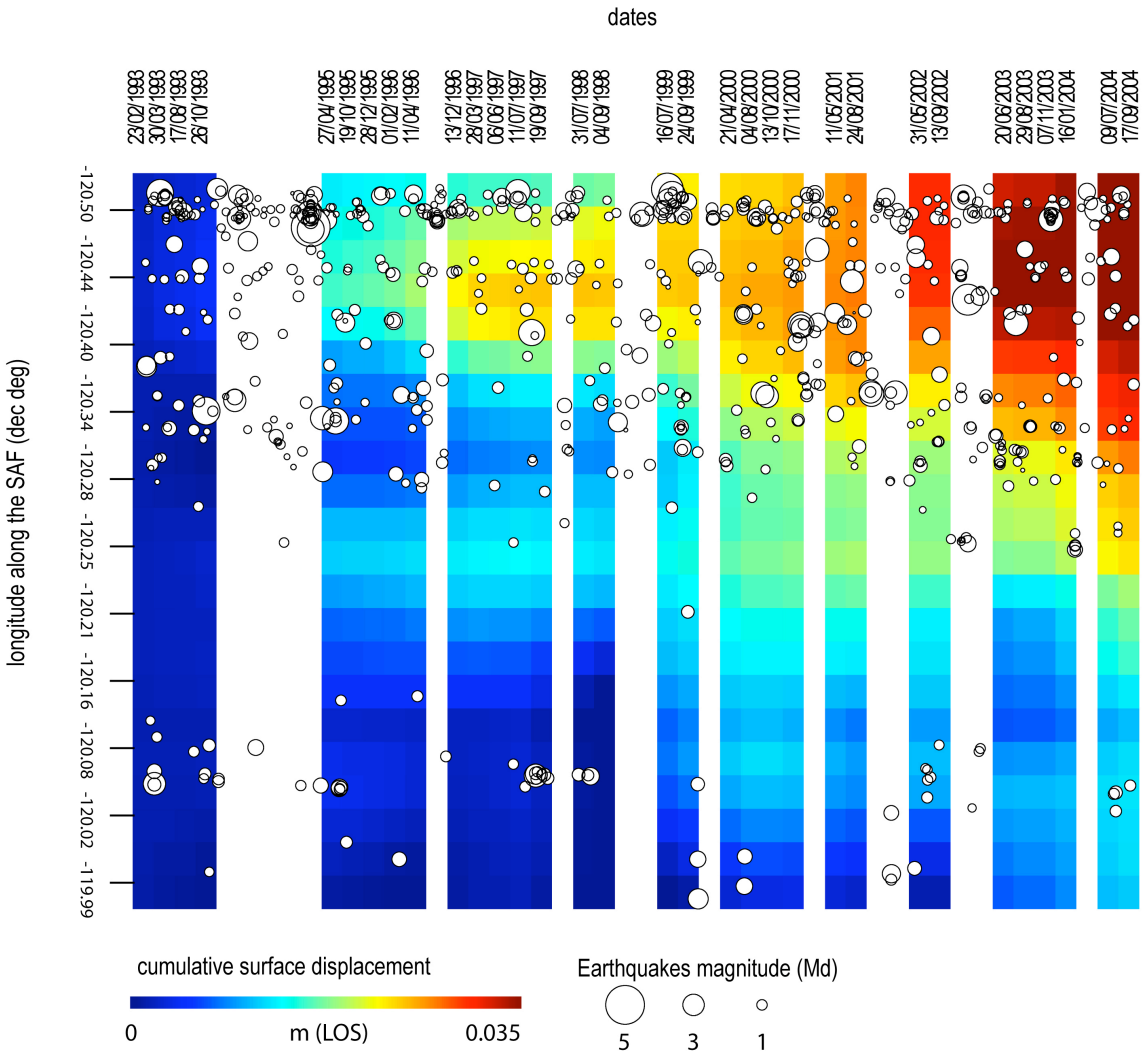

Figure 6.5. Spatiotemporal evolution of surface creep on the SAFZ from north of Parkfiled to South of Cholame plotted along with miscroseismicity.

Creep at the surface ranges from episodic to almost steady state dynamics. Therefore, the style of slip at depth is decoupled with the style of slip at the surface, probably because of varying rheology of the upper crustal material. Subsidence due to water pumping in the Paso Robles sub-unit manifested as a bull's-eye-shaped rate change pattern south of Parkfield is a marked feature in the inter-seismic interferogram (Fig. 6.2). Valentine et al (2001) used ERS InSAR as well as ground water level data from

58 wells to study this phenomenon. They do not report that it reaches the Parkfield section of the SAFZ thus we can be confident that the InSAR signal close to the SAFZ at Parkfield is primarily tectonic. Similar features, though smaller in area, can be observed in the northern sector of the inter-seismic interferogram.

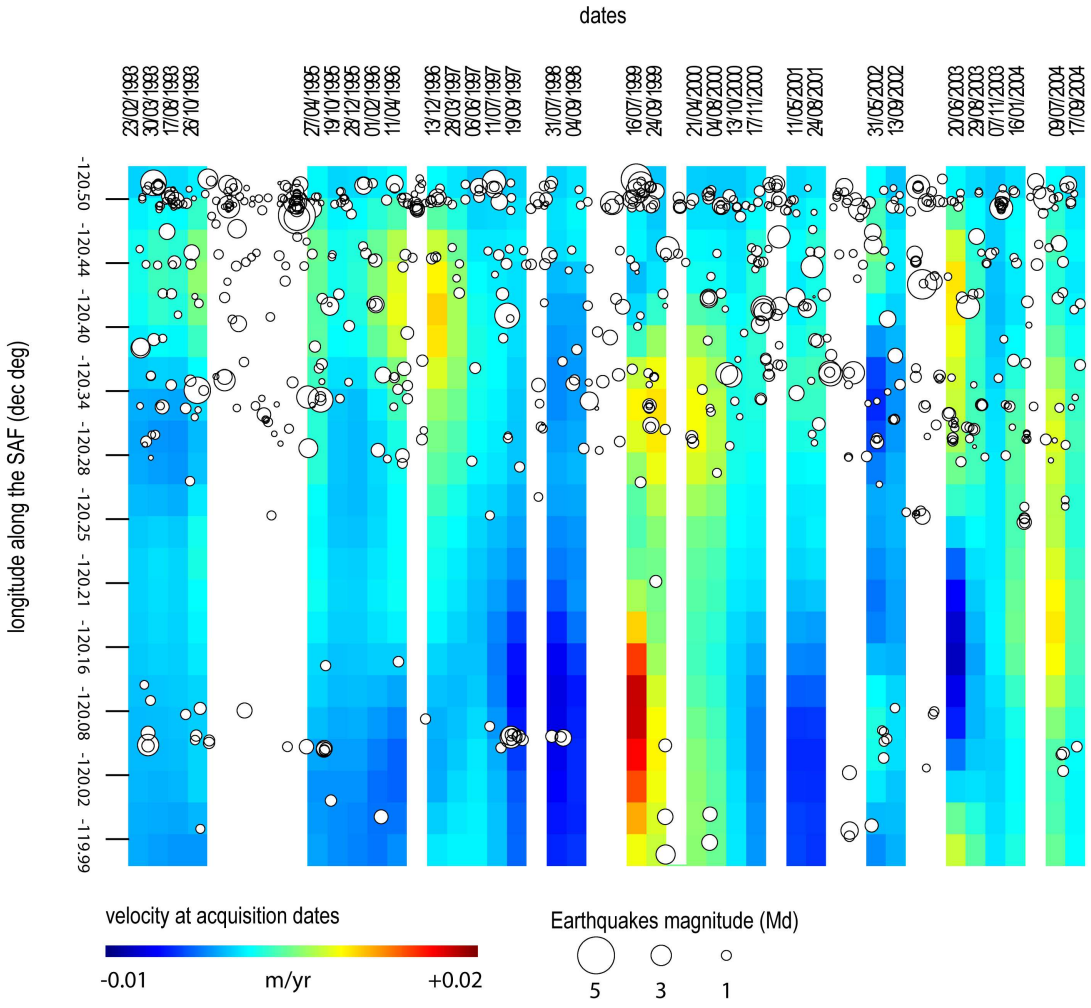

Figure 6.6. Velocity change of surface creep on the SAFZ from north of Parkfiled to South of Cholame plotted with miscroseismicity.

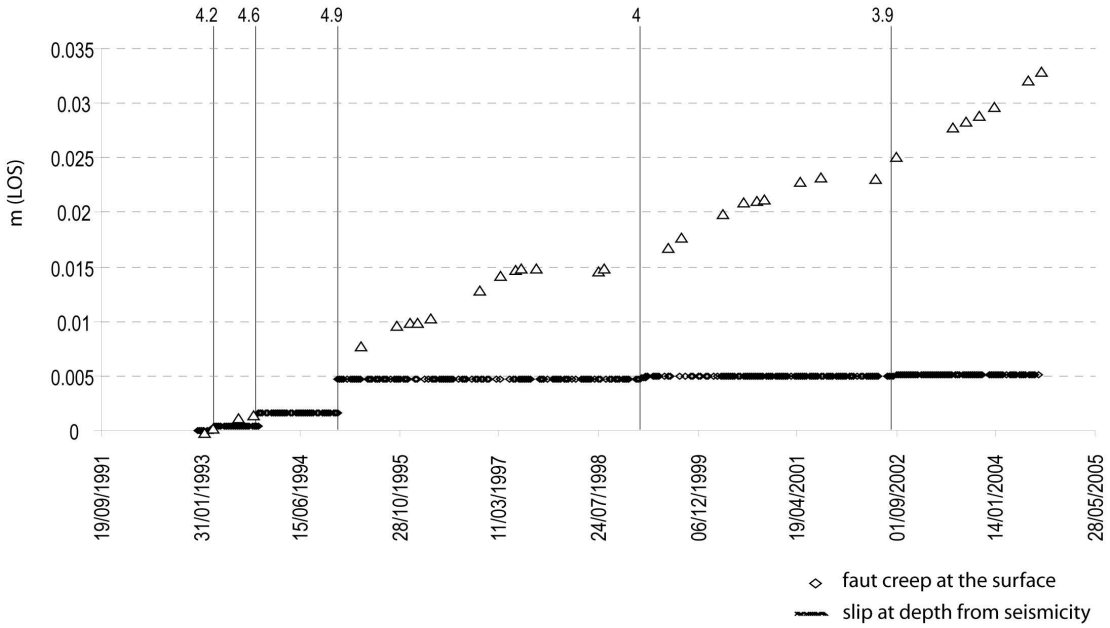

Figure 6.7. 1993-2004 temporal evolution of seismic slip calculated from seismic moment at depth (black dots) compared with the temporal evolution of aseismic creep at the surface measured from InSAR (white triangles). Vertical lines indicates prominent 3.9 to 4.9 Md Earthquakes.

These correspond to petroleum and gas withdrawal from a shallow reservoir in the Lost Hills field and neighbouring reservoirs (Fielding et al, 1998; Brink et al, 2002). Pumping-induced vertical motions are a source of non-tectonic signal heterogeneities and thus are not considered in depth in this study.

Conclusions

The Parkfield segment of the SAFZ experienced time-variable creeping phenomena in the period 1993-2004. Creep dynamics at the surface range from periods of episodic to periods of steady-state creep (fig. 6.4). At depth, fault displacement occurs

with stick-slip dynamics. The onset of surface creep is variable in time and space (fig. 6.5), which possibly reveals a further sub-segmentation of the SAFZ in the Parkfield area. This leads to localised creep acceleration or pulses of surface displacement (fig. 6.6). While seismic activity at depth is well correlated in space with creep activity at the surface, we do not observe any first order relationship between seismic moment released at depth and the triggering of episodic creep at the surface (fig. 6.6).

The spatial pattern of the inter-seismic displacement rate (fig. 6.2) indicates that tectonic strain is not uniformly distributed along strike of the fault over the period 1993-2004. We observe a decrease in the creep rate from the Parkfield segment to south of Cholame from 1.4 ±0.3 cm/yr to 0.06 ±0.3 cm/yr and a small but significant creep rate increase on the Cholame segment up to 0.2 ±0.1 cm/yr (fig. 6.3). This result highlights strain build-up towards a stronger section of the San Andreas Fault south of the Highway-46 that corresponds to a zone of lack of microseismicity at depth.

The evidence of episodic creep on the Cholame segment of the SAFZ south of Parkfield may trigger debates since it is in contrast with previous published interpretations of GPS and trilateration data. For instance, the model presented in Murray and Langbein (2006) shows no resolvable creep between 10 and 30 km south of Gold Hill. Notwithstanding this, the profile in figure 3 seems to be in good agreement with the creep pattern retrieved by ground measurements (Bennett, 1989; Burford and Harsh, 1980; Lisowski and Prescott, 1981; Schulz et al, 1982; Titus et al., 2006), at least up to longitude 120°15'W (DMS).

Stone et al. (2002) and Young at al. (2002) studied the recent rupture history of the Cholame segment by trenching. They reported that although unlikely, they can not rule out the possibility of a post 1857 displacement. According to Young et al., (2002) post-1857 tectonic fracturing of historic sediments may have resulted from creep, triggered slip, or ground shaking from nearby moderate earthquakes.

This segment of the SAFZ merits close monitoring as it has shown recent evidence of deep slip (Shelly et al., 2009) and was the nucleation point of the great 1857 Fort Te-

jon earthquake (Sieh, 1978). Unfortunately, we could not find in the literature alignment array surveys or creepmeters measurements on the segment of the SAFZ stretching from 120°00'W to 120°15'W (DMS) to validate our observations at this location.

Acknowledgements

Authors wish to acknowledge BRGM Research Direction (RD) for financially supporting this work and the European Space Agency (ESA) for providing ERS1-2 data in the framework of the Category-1 research proposal.

Chapter 7

The Mw 7.9, 12 May 2008 Sichuan earthquake rupture measured by sub-pixel correlation of ALOS PALSAR amplitude images

by Marcello de Michele [1], Daniel Raucoules [1], Cécile Lasserre [2], Erwan Pathier [2], Yann Klinger [3], Jérôme Van Der Woerd [4], Julia de Sigoyer [5], Xiwei Xu [6]

1 French Geological Survey (BRGM), Land Use Planning and Natural Risks Division, Orléans, France.

2 Laboratoire de Géophysique Interne et Tectonophysique, CNRS, Université Joseph Fourier, Grenoble, France

3 Institut de Physique du Globe de Paris, Laboratoire de Tectonique, Paris, France.

4 Institut de Physique du Globe, Strasbourg, France.

5 Ecole Normale Supérieure, Laboratoire de Géologie, Paris, France.

6 China Earthquake Administration, Institue of Geology, Beijing, China.

Foreword - This chapter resumes the work that I carried out in collaboration with the colleagues of the CIEST group (Cellule d'Intervention et d'Expertise Scientifique et Technique) following the activation of the International Charter on Space and Major Disasters after the catastrophic Sichuan earthquake. This

chapter mainly contains the results accepted for publication (2009) in the special issue on the Sichuan earthquake of *Earth Planets and Space* journal. Unfortunately, at the time of the writing of this dissertation, the *Earth Planets and Space* special issue has not been published yet. This work has been completed in October 2008. We put into evidence the main surface ruptures of the Sichuan earthquake as well as some guesses about possible secondary surface ruptures (in particular the one on the Noth-Eastern mountain front) that lead us to the idea of an active «blind structure» that we investigate further in chapter 9. I have been invited to present this work at the Technical University of Chengdu in 2008 by the team of the *Laboratoire de Géologie* at the *Ecole Normale Supérieure,* who I wish to thank. In that occasion I participated to a field trip along the rupture zone in the Longmen Shan. The field trip was also organized by the team of the *Laboratoire de Géologie* at the *Ecole Normale Supérieure* in the frame of a collaboration with the Technical University of Chengdu (ANR Jeunes Chercheurs, lead by Rodolphe Cattin).

With the work presented in this chapter, we face the biases in the InSAR signal due to the ionosphere. It is actually the first time that we encounter the ionospheric signature in the radar data. This aspect of the InSAR processing is described in more details in chapter 8.

Summary

PALSAR L-band spaceborne Synthetic Aperture Radar (SAR) amplitude images are used to map the Sichuan earthquake rupture (China, Mw 7.9, 12 May 2008) and to identify the faults activated by the earthquake. A sub-pixel correlation method is used to retrieve the coseismic displacement field projected into the line of sight of the satellite and the horizontal along-track direction, and to map the surface rupture. The earthquake broke ~270 km of the Beichuan fault and ~70 km of the Guanxian fault, with a complex thrust-dextral slip mechanism. Along the southwestern part of the rup-

ture, slip seems to be partitioned into a dextral-dominant component on the Beichuan fault and a thrust-dominant component on the Guanxian fault. Dextral slip may also be dominant at the northeastern tip of the Beichuan ruptured fault. Coseismic surface displacements reach on average 3 to 4 m in both measured directions. The SAR rupture mapping has proven complementary to field studies extending the zone of coseismic displacements and identifying other possible co-seismic rupture strands.

Introduction

The Sichuan earthquake, Mw 7.9, struck the western Sichuan province on 12 May 2008. It represents one of the most disastrous earthquakes in Chinese history, severely affecting an area where little historical seismicity is reported (Gu et al., 1989; Chen et al., 1994) and a small convergence rate is measured (e.g., Gan et al., 2007). The hypocentre is located within the Longmen Shan at 19 km depth (USGS, 2008) between two major faults of the Longmen Shan thrust system, the Wenchuan and Beichuan faults (Figure 7.1). The Longmen Shan thrust system bounds the eastern margin of the Tibetan plateau and is considered as a major thrust zone that was reactivated during the India-Asia collision (e.g., Tapponnier and Molnar, 1977; Avouac and Tapponnier, 1993; Chen and Wilson 1996; Arne et al., 1997). However, contrasting geological evidence of sparse thrusting and marked dextral strike-slip faulting during the Quaternary (Burchfiel et al., 1995; Densmore et al., 2007) have led to models of dynamically sustained topography or crustal channel flow (Royden et al., 1997) limiting the role of earthquakes in mountain building and leaving the mechanism of long term strain distribution in this area as an open question. In this paper we use L-band spaceborne Synthetic Aperture Radar (SAR) from the PALSAR sensor onboard the ALOS satellite to map the Sichuan earthquake rupture and to identify the faults activated by

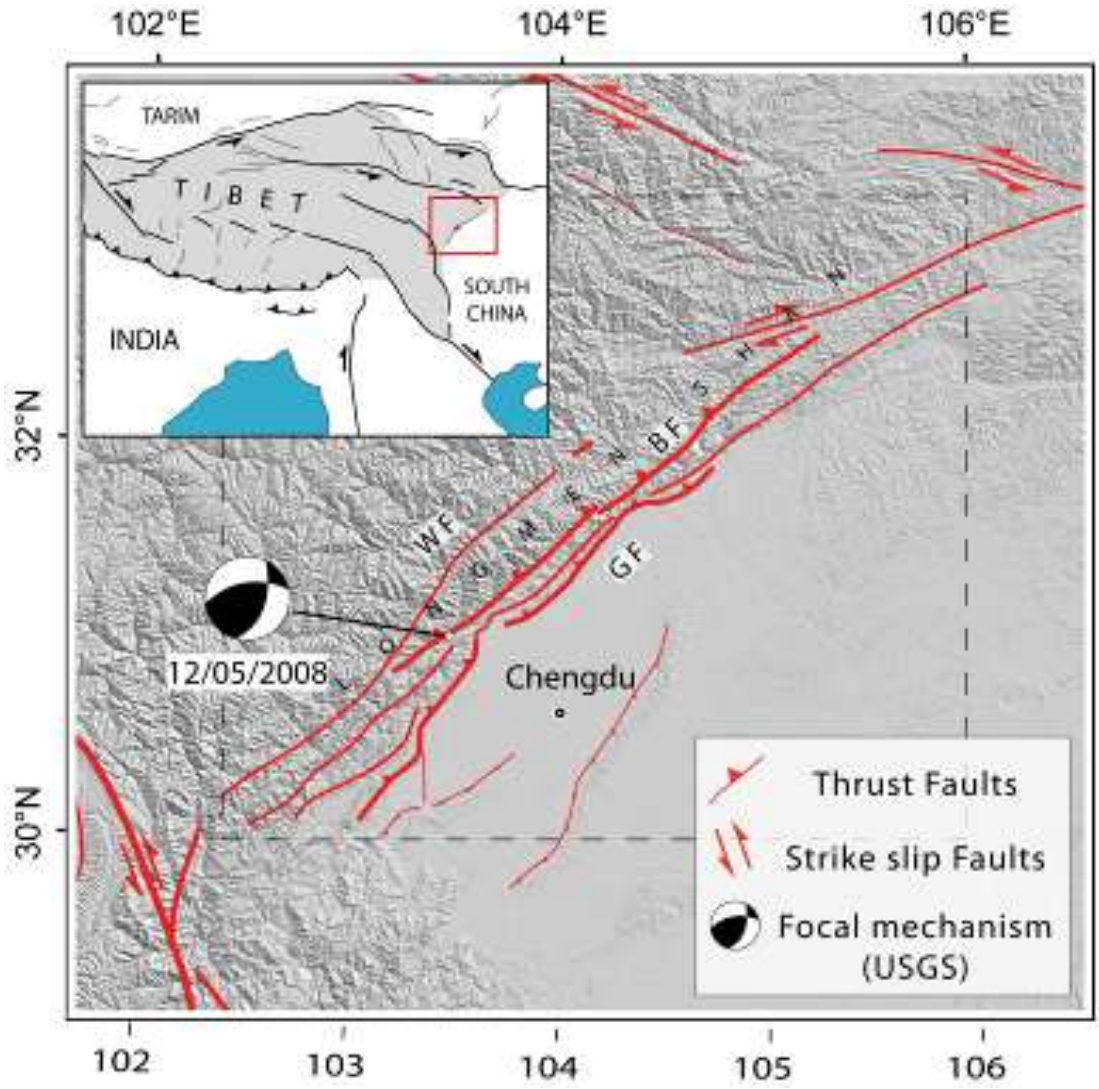

Figure 7.1. The study area struck by the Sichuan earthquake. Quaternary active faults and their kinematics are plotted in red (modified from Tapponnier and Molnar, 1977). BF=Beichuan fault; WF=Wenchuan Fault; GF=Guanxian Fault. The dotted rectangle corresponds to the location of figure 2 and 3.

the earthquake. By measuring the co-seismic offsets field in both the line of sight (i.e., slant range) and along track (i.e., azimuth) directions of the sensor, we gain an understanding of the rupture geometry, segmentation and sense of displacement. Our results complement field observations since parts of the ruptured areas are inaccessible impeding detailed field studies (Dong et al., 2008; Xu et al., 2009).

Track	Date	Mode	Pixel size Range/ Azimuth (m)
471	29/02/2008 31/05/2008	Ascending	4.68 / 3.15
472	31/01/2008 17/06/2008	Ascending	4.68 / 3.15
473	17/02/2008 19/05/2008	Ascending	4.68 / 3.15
474	05/04/2008 05/06/2008	Ascending	4.68 / 3.15
475	21/12/2007 22/06/2008	Ascending	4.68 / 3.15
476	08/04/2008 24/05/2008	Ascending	4.68 / 3.15

Table 7.1. PALSAR data used in this study.

Data analysis

A SAR system sends radar pulses to the ground and measures the amplitude and the phase of the backscattered signal. Each radar return is sampled at the base of an azimuth/slant range grid so that each echo corresponds to a geographic location, after geometric transformation. If between two radar acquisitions the position of a target changes we can precisely measure its corresponding offset by subpixel correlation analysis (e.g., Michel et al., 1999; Barbot et al., 2008). We use PALSAR amplitude

images acquired before and after the Sichuan earthquake and measure the offset field generated by the earthquake in the range and azimuth directions by using the subpixel correlation routine implemented in the GAMMA software (Werner et al., 2005). We calculate offsets based on a 64 pixel window size on PALSAR fine beam single polarisation mode (FBS) data acquired during six parallel overlapping ascending tracks (Table 7.1). Range offsets may suffer from limitations due to stereoscopic effects. We reduce the stereoscopic contributions to coseismic range offset by adapting the methodology based on Principal Component Analysis presented in de Michele et al. (2008) to SAR amplitude images. We use the Digital Elevation Model (DEM) from the Shuttle Radar Topography Mission (SRTM) projected into radar geometry to estimate and reduce for the stereoscopic effect. Azimuth offsets may be affected by the influence of ionospheric electron density fluctuation occurring during the synthetic aperture (Gray et al, 2000). For an L-band SAR, this phenomenon results in deca-km scale modulation in the position of optimum azimuth registration, which appears as oblique bands or 'azimuth streaks' in the offset image. Based on the observation that the azimuth streaks have a constant preferential orientation that does not coincide with the strike of the fault, we reduce this effect by an adaptive de-stripe filter originally developed by Leprince et al. (2007). It yielded a ~56% average ionospheric correction on the azimuth offsets. The corrected offsets maps are then orthorectified and assembled (Figure 7.2, 7.3).

Results

Figures 2 and 3 present maps of the range and azimuth offsets. We interpret steep offset gradients as the surface expressions of the earthquake rupture. The clearest offsets indicate that the rupture broke a 270 km-long major segment of the Beichuan Fault and a 70 km-long segment of the Guanxian Fault, both trending ~N55E. It seems that another 10 km-long segment ruptured perpendicularly to the Beichuan and Guanxian Faults at the southwestern end of the Guanxian inferred rupture (grey segment in Fig-

ure 7.2). Its signature is markedly visible on both offset maps. Our SAR rupture map is confirmed by field observations made by Dong et al. (2008) and Xu et al. (2009) and complements them in inaccessible areas. Further interpreting the SAR offset results, other ruptured fault segments might be evidenced although their signatures are less clear due to noise. These segments are typically inside the Longmen Shan, along the Wenchuan Fault and along the northeastern part of the Guanxian fault (black dotted lines in Figures 2 and 3).

Figure 7.4 shows along-strike profiles of range and azimuth offsets across the Beichuan and Guanxian faults. Each measured point on the profiles in Figure 4 results from the stack of 51 cross-strike profiles [according to the method proposed by Klinger et al. (2006) and Avouac et al. (2006) and implemented in Leprince et al. (2007)], providing an approximation of the offsets every 1 km. The plot in figure 7.4 yields an estimate of the magnitude and standard deviation of fault slips at the surface in range and azimuth directions. The standard deviation obtained during the stacking process provides an estimate of the precision of the offsets. This yields 0.31 m in azimuth and 0.24 m in range. The range offsets reach 3 and 2 m and the azimuth offsets reach 3.7 and 2.5 m on the Beichuan and Guanxian faults, respectively. However, our offset measurements are limited to two directions. Without a third component of the displacement and geometric constraints on the dip of the faults, we cannot make a quantitative comparison between horizontal and vertical slip values collected in the field and our offsets.

Discussion and conclusion

Figures 7.2 and 7.3 display a complex rupture pattern that propagated on different fault segments. Results in Figure 7.4 show the offset values in the range and azimuth

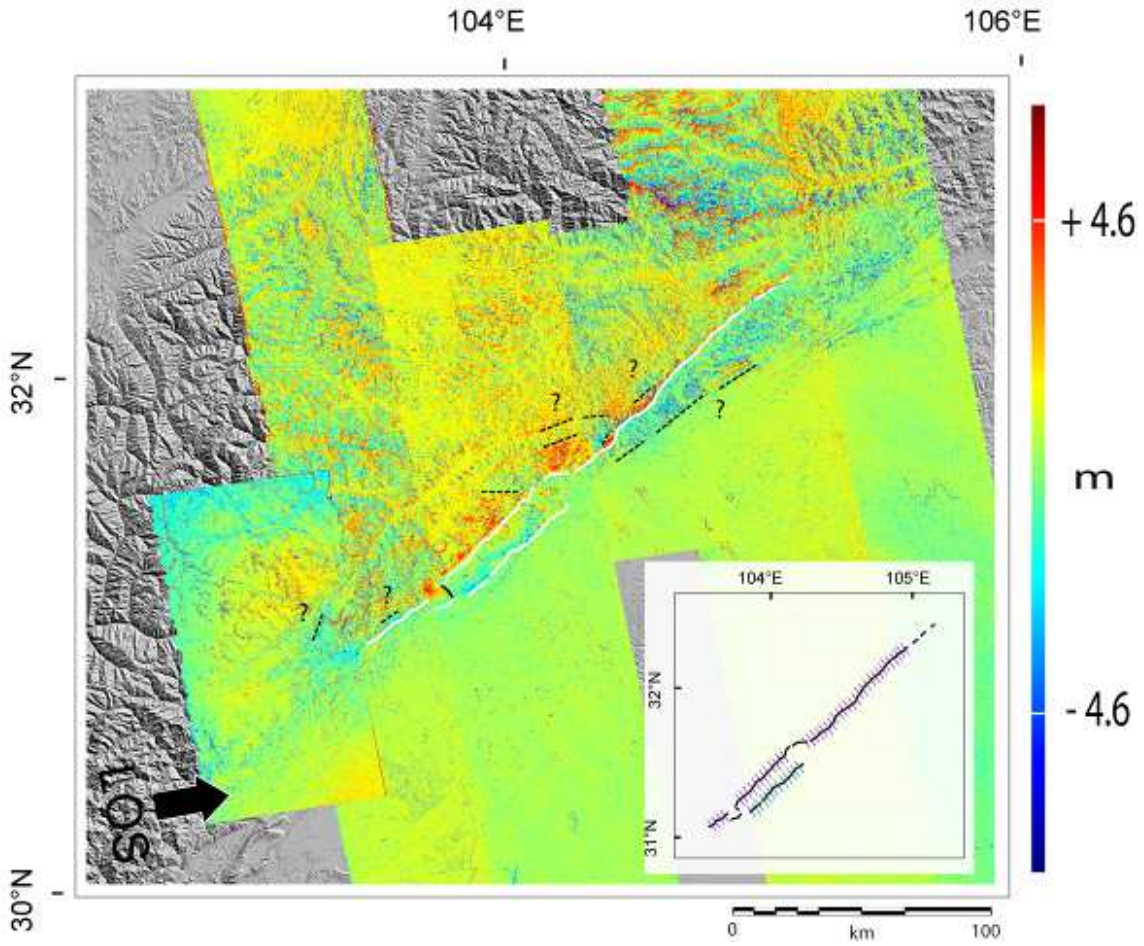

Figure 7.2. Offsets in the range direction. Our interpretation of the rupture is plotted in white. Dark dashed lines represent possible rupture segments not yet observed in the field. The ~10 km rupture segment striking NW-SE (perpendicular to BF and GF ruptures) is presented in bold black (here and in Figure 7.3). The inset represents the average location of profiles used in the stack to retrieve the offset plots in Figure 7.4. See the inset of Figure 7.3 for the satellite acquisition geometry.

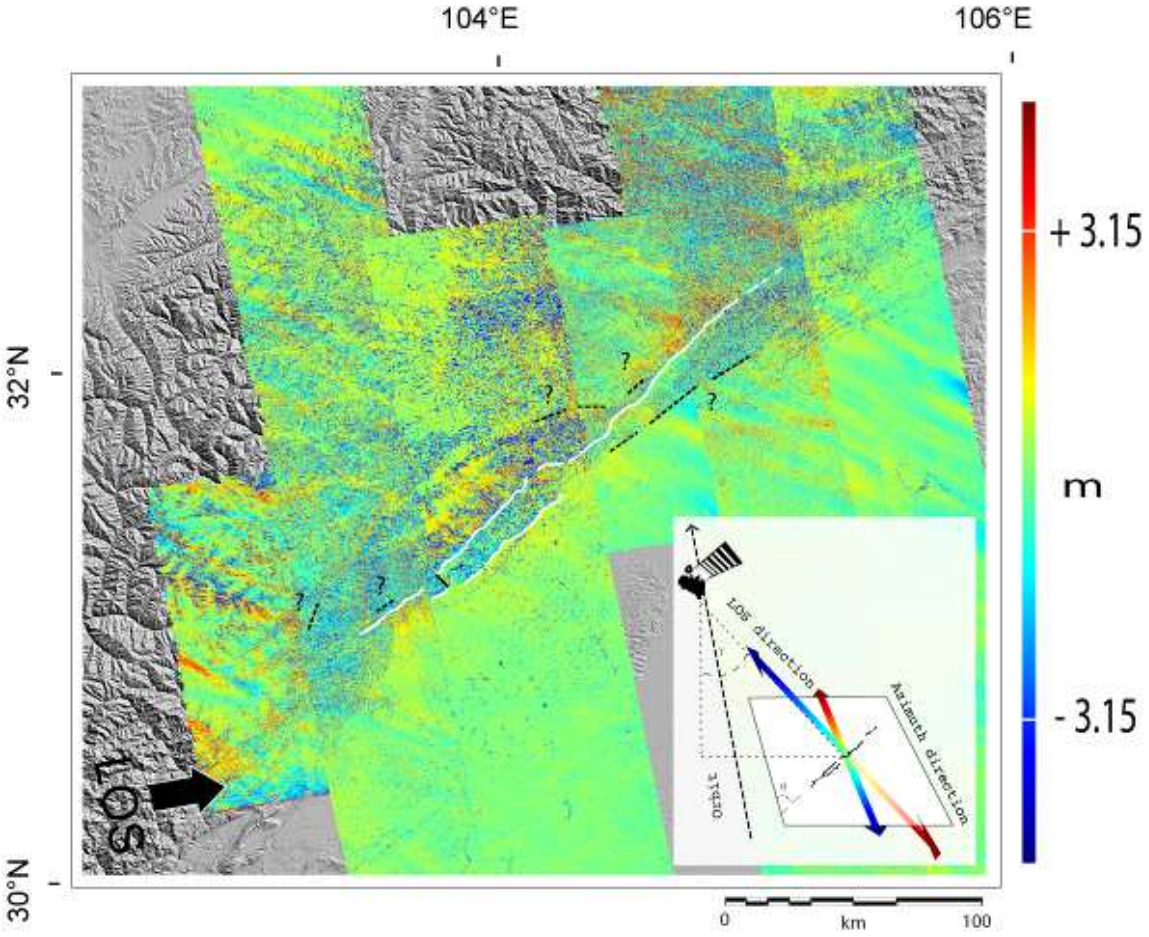

Figure 7.3. Offsets in the azimuth direction (azimuth streaks reduced). Our interpretation of the rupture is plotted in white. Dark dashed lines represent possible rupture segments not yet observed in the field. The inset represents the PALSAR acquisition geometry relative to our case study. Colour scaled arrows indicate the slant range and azimuth direction of the measured offset relative to the rupture position. This is a key to interpret the sense of displacement in Figures 2 and 5. γ = sight angle (34°), θ = angle between the rupture strike and azimuth direction (~65°).

direction. Taking into account the rupture strike, the satellite acquisition geometry (inset of Figure 7.4) and field observations we can try to constrain the interpretation of the fault slip direction during the Sichuan earthquake based on range and azimuth offset values of Figure 7.4. Assuming that the faults ruptured with a reverse dextral

mechanism (Dong et al. 2008; Xu et al. 2009), we can state that positive offsets in both range and azimuth represent dextral-dominant slip while negative values in both directions correspond to thrust-dominant slip. With this in mind, we can infer the spatial partitioning of reverse and strike-slip faulting along the Beichuan and Guanxian faults.

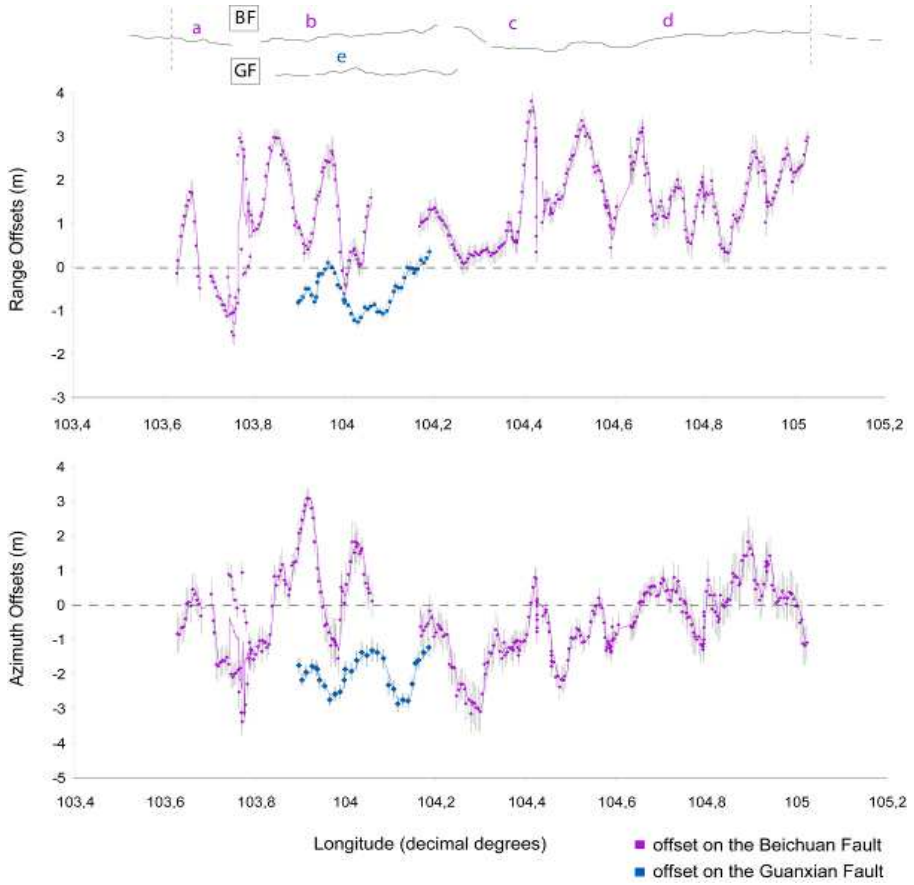

Figure 7.4. Plot of range and azimuth offsets measured along the strike of the Beishuan fault (BF) and Guanxian Fault (GF) ruptures (plotted on top as reference). Major components of slip are dextral or reverse when offsets are positive and negative, respectively (see text for details). Longitude values are sampled along the strike of the rupture.

We can argue that the Beichuan fault ruptured with a complex thrust-dextral mechanism while the Guanxian fault seems to have ruptured as an almost pure thrust. Dextral-reverse slip on segment *a* of the Beichuan fault becomes partitioned into a dextral dominant component on segment *b* of the Beichuan fault and thrust-dominant component on segment *e* of the Guanxian fault (Figure 7.4). From segments *c* to *d* of the Beichuan fault, slip seems to evolve from dextral-reverse to dextral-dominant. This is not totally in agreement with field data, which show mostly thrust on the Guanxian fault, though equivalent reverse and dextral motion on the Beichuan fault.

In conclusion, sub pixel correlation of ALOS PALSAR amplitude images allowed us to map and measure the coseismic rupture of the Sichuan earthquake. Our results complement field observations and thus allow a broader view of the rupture extension and segmentation.

Acknowledgement

The data used in this study were provided by the Japanese Space Agency (JAXA) through the CIEST agreement (Cellule d'Intervention et d'Expertise Scientifique et Technique) and the International Charter on Space and Major Disasters. M. de Michele and D. Raucoules are funded by the research programs of BRGM.

Chapter 8

Assessing ionospheric influence on L-band SAR data: Implications on co-seismic displacement measurements of the 2008 Sichuan Earthquake.

by Daniel Raucoules and Marcello de Michele

the authors are with the French Geological Survey (BRGM), Land Use Planning and Natural Risks Division, Orléans, France.

Foreword - The Sichuan earthquake brought the influence of the ionosphere on L-band radar data on the scene of the solid Earth geophysics community. This phenomenon was already known by a number of researchers that uses InSAR to study the ionosphere, though it was almost unknown or underestimated by space geodesists. This chapter resumes the work published as Raucoules and de Michele, 2010 in *IEEE Geoscience and Remote Sensing Letters* in which we describe our findings about the influence of the ionospheric delay on L-band radar data and the influences on the co-seismic displacement measurements both by InSAR and by correlation of radar amplitude images. This work has profited of a number of stimulating discussions with the CIEST members, we could say that the main idea has almost originated from these discussions, in particular with Marie Pierre Dion and Cecile Lasserre.

Summary

Ionospheric contributions to the phase of L-band Synthetic Aperture Radar (SAR) signals put severe limitations on ground displacement measurements retrieved by either differential SAR interferometry (DinSAR) or radar amplitude image offsets. Such contributions result in an ionospheric phase screen (IPS) on the differential interferogram and in directional fluctuations in the relative position of azimuth pixels on offsets maps. In this article, we propose a procedure for estimating and removing ionospheric contributions to surface displacement measurements derived from L-band SAR data. We test the procedure on SAR data from the 28 May 2008 Sichuan Earthquake.

The applied corrections allow both a clearer interpretation of the surface rupture and a more accurate measurement of the surface displacement, which has important implications in earthquake modeling based on L-band SAR data.

Introduction

Within the InSAR technique both the phase and the amplitude of the backscattered radar signals can be used for measuring earth surface displacements and deformations. While DinSAR is based on the signal phase difference between two radar acquisitions (e.g. Gabriel and Goldstein, 1989; Massonnet and Feigl, 1998) and provides surface displacement values in the Line-of-Sight direction of the satellite (LOS), the sub-pixel correlation technique measures the sub-pixel offsets between two radar amplitude images both in the azimuth and LOS directions of the satellite (e.g. Michel et al., 1999; Hu et al., 2008). The former technique is as accurate as a fraction of the employed radar wavelength and is sensitive to mm to dm surface displacement. The latter technique is generally sensitive to ground displacements larger than 0.1 pixels, which is about 50 cm in the azimuth direction for a space-borne radar sensor such as the Phase Array L-band Synthetic Aperture Radar (PALSAR). These two techniques are complementary, particularly when LOS deformation gradients

larger than one quarter of the wavelength per pixel cause interferometric signals to de-correlate. This might occur close to a seismic rupture, such as the ~270 km long Sichuan earthquake rupture where co-seismic slip reached up to 8 metres (Xiwei et al., 2009).

While L-band SAR signals are of particular interest in studying earthquakes as it is less affected by temporal canopy changes than C-band, it could be severely affected by ionospheric heterogeneities occurring during the synthetic aperture calculation (e.g. Quegan and Lamont, 1986; Mattar and Gray, 2002). Due to the "dispersive" nature of the medium, the ionosphere refractive index depends on the inverse of the square of the electromagnetic frequency employed. Therefore, L-band SAR data are more affected than C-band SAR.

The ionosphere influence on the SAR signal affects both azimuth sub-pixel offsets and differential interferograms. The first bias results from directional fluctuations in the relative sub-pixel position of azimuth pixels, already reported in literature as azimuthal "streaking" (Mattar and Gray, 2002). The second bias results from relative lengthening of the wave paths between two radar acquisitions affecting the interferometric signal. As reported by recent studies based on L-band InSAR on the Sichuan earthquake (de Michele et al., 2009; Kobayashi et al., 2008), ionospheric influences on the SAR signal appear to introduce several difficulties for the retrieval of surface deformation from both sub-pixel offset of radar amplitude images and differential interferometry. In this paper we focus on the ionospheric influences on the SAR signal, assess their impact in the presence of co-seismic surface displacement and try to propose a method to estimate and remove their contributions both to sub-pixel offset and to interferometric phase. We apply the method to the 2008 Sichuan earthquake surface displacement (figure 8.1).

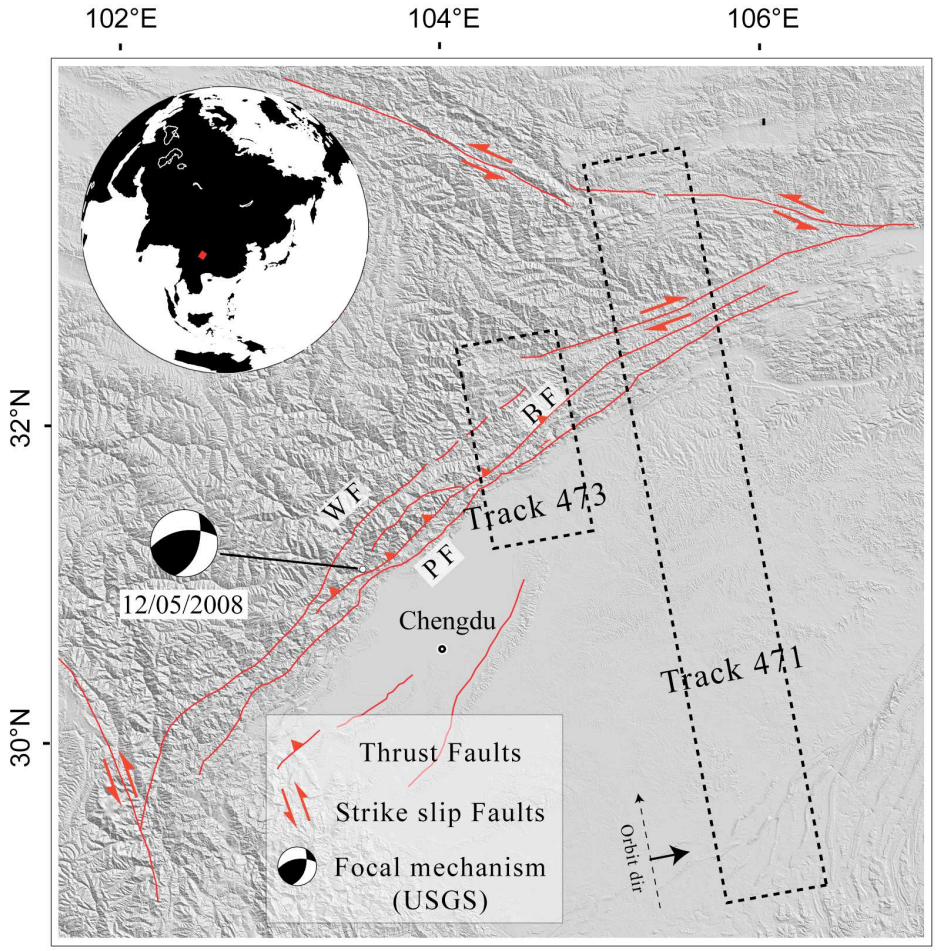

Figure 8.1: Area of interest. Locations of PALSAR acquisitions used are identified by the dotted rectangles. WF= Wenchuan Fault; BF= Beichuan Fault; PF= Guanxian-Pengguan Fault (modified from Tapponnier and Molnar, 1977).

TABLE 8.I
ALOS PALSAR ACQUISITIONS USED FOR THIS STUDY

Track	Date	Mode	Pixel size Range/ Azimuth (m)
471	29/02/2008 31/05/2008	Ascending	4.68 / 3.15
473	17/02/2008 19/05/2008	Ascending	4.68 / 3.15

TABLE 8.II
STANDARD DEVIATION OF THE PHASE DERIVATIVE AND THE AZIMUTHAL CORRECTION ON THE SOUTHERN AREA OF TRACK 473

	standard deviation	mean
InSAR Phase derivative	0.013 rad	0.0024 rad
Azimuth offset correction	0.37 pixels	0.06 pixels

Ionospheric effects on InSAR data

Interferometric phase

The impact of the ionosphere on the interferogram is caused by the relative variation of the refractive index of the medium between the two radar acquisitions. The resulting propagation lengthening produces an interferometric phase shift.

This phase shift is related to the electron density variation, *ne* at height *h* in eq. 1. For a nadir-looking radar (Meyer et al., 2006):

$$\Delta\Phi \approx -\frac{4\pi}{c_0}\frac{40.28}{f}\Delta TEC \qquad (1)$$

with

$$TEC = \int_{o}^{H} n_e(h)\,dh$$

where ΔTEC is the variation of the Total Electron Content (TEC), *c0* the speed of light, *f* the signal frequency (Hz).

Azimuth streaking

According to Mattar and Gray (2002) atmospheric impact on C-band and L-band In-SAR results from radar signal phase modulation due to spatial variation of the ionospheric propagation conditions during the aperture time.

Meyer et al. (2006) derived the relation between ionospheric contribution to the azimuth offset (Δx_{iono}) and the ionospheric contribution to the interferometric phase, which can be expressed as:

$$\Delta x_{iono} = \alpha \frac{\partial}{\partial x}(\Delta\Phi_{iono}) \quad (2)$$

Based on this relation we can estimate the interferometric phase correction, or IPS, starting from the azimuth offsets values (Mattar and Gray, 2002. We can then remove the IPS from the interferogram to enhance the coseismic deformation measure.

Azimuth correction

We observe that the azimuth streaks on the sub-pixel offset map show up with a preferential direction (figure 8.2a). Azimuth offsets are estimated on co-registred images

(co-registration based on the adjustment of a bilinear model) of the interferometric pairs and therefore with identical geometry. In such conditions possible residual topographic effects are very limited (that is not the case with slant range offsets for with stereoscopic effect is not negligible even with perpendicular baselines of some tens of metres).

Over the Sichuan earthquake area the azimuth streaks direction (but not their amplitude) is constant over a large spatial and temporal scale, at least during the concerned period (e.g. de Michele et al., 2009; Kobayashi et al., 2008). The direction of the streaks seems to be constant for a given geographical area across different radar tracks. However, Mattar and Gray (2002) who worked on polar areas noticed, in certain cases, along-track variation of this direction. The influence of the position respect to the magnetic poles has to be investigated for other test sites.

On the Sichuan area, the streaks strike ~N115E, while the earthquake ruptures strike ~N40E (Xu et al., 2009). According to Luhr et al. (2003), we can observe that South China is located in an area affected by a strip of high electron density (related to the location of the geomagnetic equator) which main orientation roughly corresponds to this orientation. That could explain the direction of the streaks and the high values of ionospheric effects on the area.

Based on this peculiarity we improve the methodology firstly proposed by Mattar and Gray (2002) by taking into account the spatial evolution of the azimuth streaks amplitude along their length over the entire radar image width.

In order to reduce the azimuth streaks, de Michele et al. (2009) proposed to cut the azimuth offset map into three sub-images within which the azimuth offset correction is approximated by a constant value along the streaks direction (i.e. the correction is constant by segments corresponding to the subimages). This method provides a satisfactory correction to highlight the surface trace of the earthquake rupture and does not affect coseismic offset values in the near field. However, this approximation yields residual discontinuities at the sub-images boundaries.

Among the 1D low pass filters that could be used for this purpose, we propose to use single polynomial fits. In this paper, we approximate the azimuth streaks amplitudes by a third degree polynomial along the streak direction. After rotation of the image in order to align horizontally the streaks, each line is replaced by its third degree fit. This approximation fits the trend well enough to remove most of the azimuth streaks without affecting high-frequency small-scale offsets, such as near field offsets due to the earthquake rupture. We test the methodology on two different ALOS PALSAR tracks (table 8.I) acquired over the Sichuan area (figure 8.1). We first test the methodology on a radar track less affected by co-seismic deformation (figure 8.2a) then we apply it to enhance the coseismic rupture on a different track (figure 8.3a/b). We assume that the computation of the α coefficient (supposed the same for both frames as only dependent on sensor parameters) on the track less affected by deformation is more reliable as the offset and phases are mainly related to ionosphere and not deformation.

In both cases, we compute sub-pixel offsets maps on full resolution amplitude images by using the GAMMA routines (http://www.gamma-rs.ch/), from which we subtract a linear offset ramp (figure 8.2a). As the images are co-registered before correlation, the result can be tilted; this ramp is therefore not significant in terms of deformation but can be considered as a bias. In addition, residual effects (uncompensated orbits) are also expressed as ramps. On the other hand, the objective of removing a ramp is to obtain a deformation result comparable to InSAR that is also biased on scales larger than the image coverage (in fact, we cannot distinguish a linear trend on deformation affecting all the image from residual orbital errors or large scale atmospheric effects). Such effects systematically affect InSAR results. For instance one of the fringe 2007 symposium (ESA, 2007) recommendations on InSAR results (in fact Persistent Scaterrers Interferometry) was to systematically subtract ramps on the results.

Figure 8.3a) and 8.3b) show an example of correction applied to the azimuth offset map on track 473, concerned by the seismic slip with values of up to 5m. We can notice that the deformation was initially masked by the ionospheric contributions to azimuth offset (figure 8.3a). After correction, the coseismic rupture is enhanced and it

can be mapped. Also we can retrieve the azimuth component of the near field coseismic offset (about 1 pixel in the azimuth direction, i.e. 3.6 metres), which is crucial for inverse modelling of the earthquake

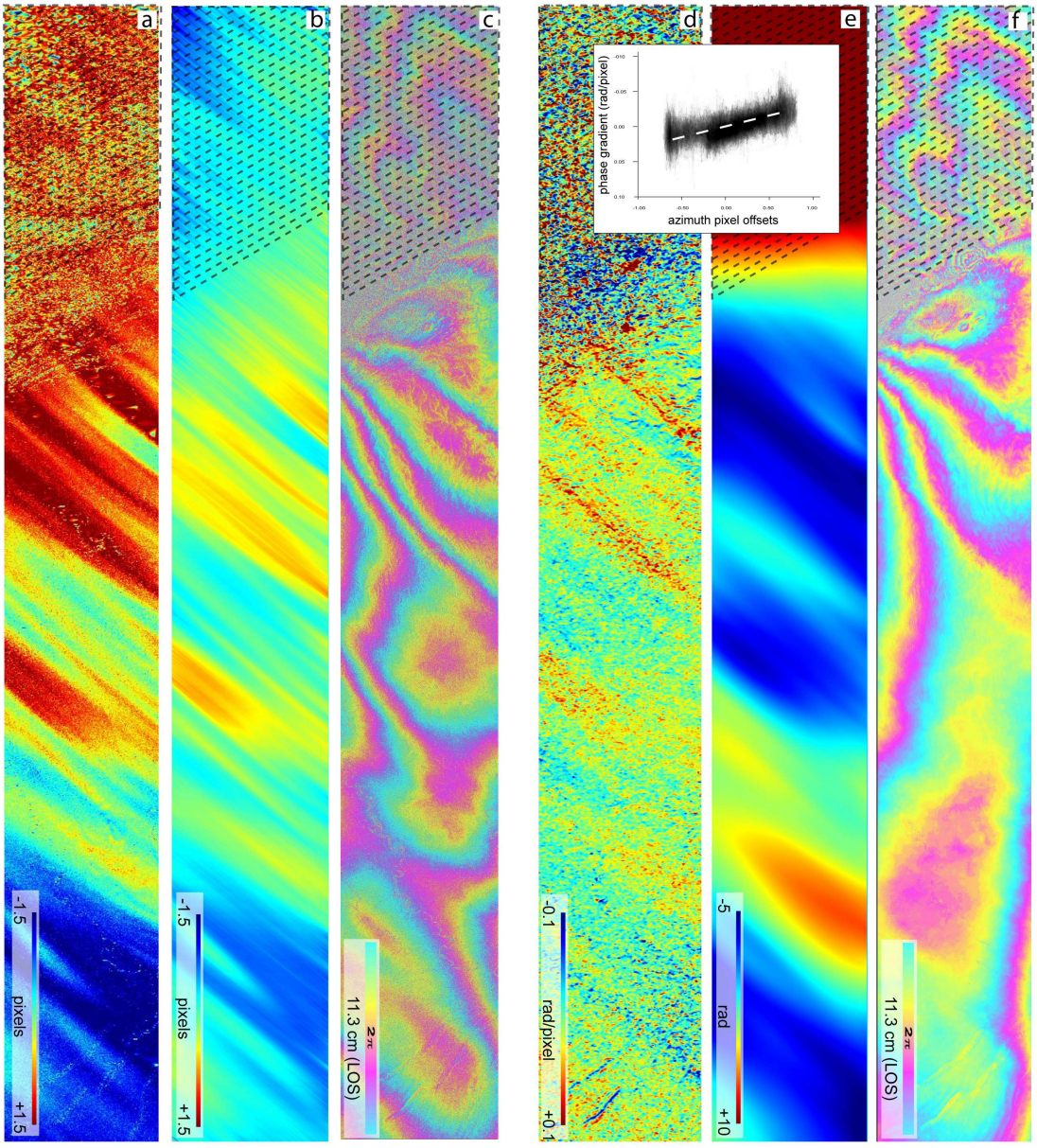

Figure 8.2 a) azimuth sub-pixel offset map (track 471). Azimuth streaks are clearly visible. b) Ionospheric contribution to the azimuth offsets after directional polynomial fitting and linear trend removal c) Interferogram (track 471). Patterns with several fringes orientated in the 'streaks' direction are visible d) Along-orbit phase derivative (track 471). We observe the similarity with the azi-

muth streaks. The scatterogram between b) and d) data is plotted. It is consistent with a β coefficient of 0.032 rad/pixel (white line). e) IPS for track 471. f) corrected interferogram

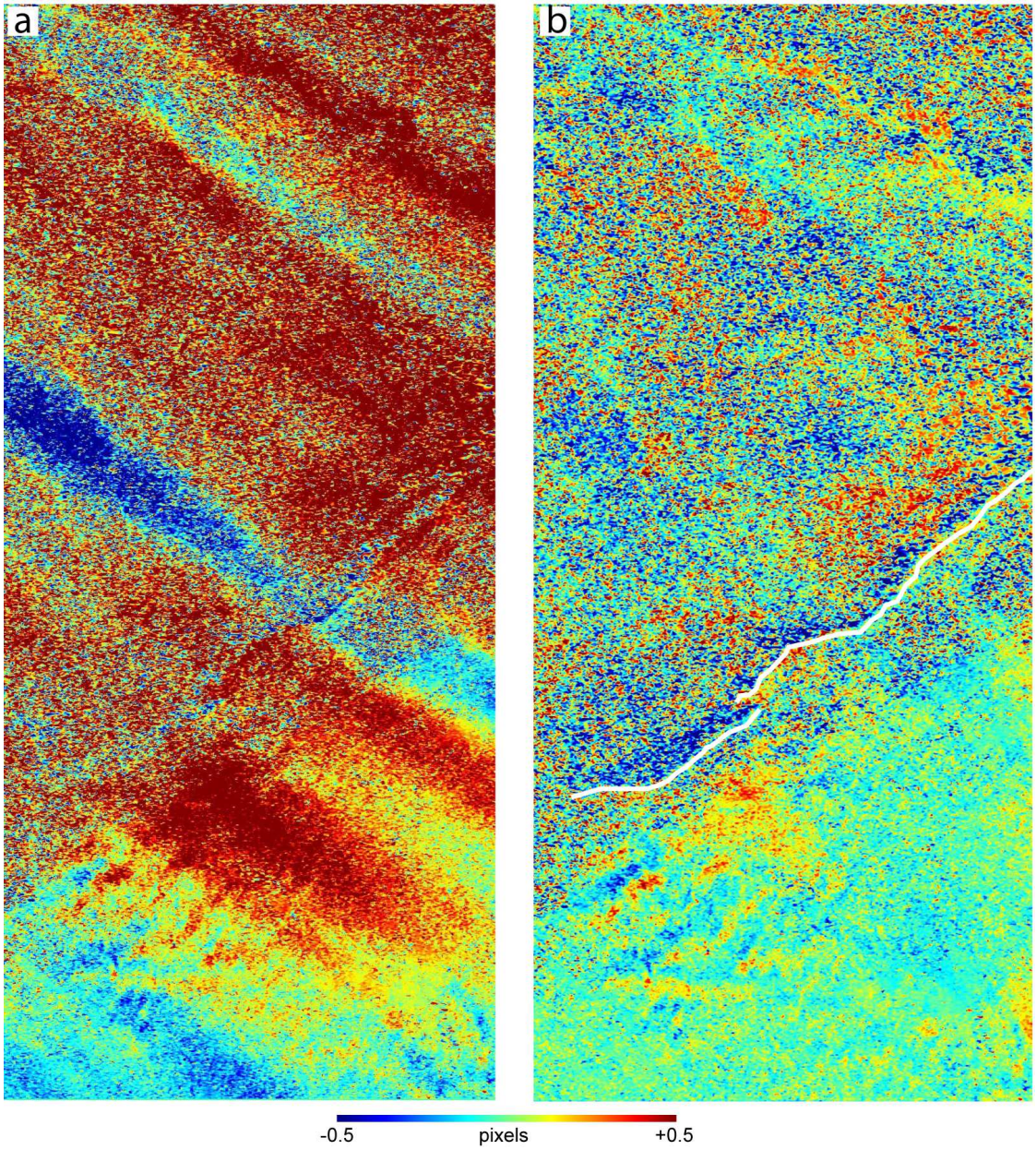

Figure 8.3 a) azimuth offset map for track 473. b) Azimuth offsets map corrected for the ionosphere. The white line is the Sichuan earthquake surface rupture measure on the field (modified from Xiwei et al., 2009).

Computation of the phase derivative

As pointed out in section 1, the contribution of the ionosphere to the azimuth offset can be associated to the along-track derivative of the interferometric phase. We will use this information to calculate the IPS and remove it from the coseismic interferogram.

As a prior processing step to estimate the phase correction, we compute the phase derivative on an extended area of track 471 where we infer no major surface deformation has occurred. In order to reduce noise, we applied a 20 pixel mean filter in the columns direction. Then, we compute the derivative by using eq. 3. With this formulation, the derivative respect to the line index i for a given pixel (i,j) can be estimated on the complex interferogram without unwrapping.

$$\frac{\partial}{\partial i}\left(\Phi_{i,j}\right) = W(W(\Phi_{i+1,j}) - W(\Phi_{i,j}))$$

with $W(x)=x \ [2\pi]$ and $W(x) \in [-\pi \text{ rad}, +\pi \text{ rad}]$ (3)

The benefits of the phase derivative image are twofold. Firstly, it allows us to confirm the validity of the azimuth offset correction estimation. In fact, similarities between the pattern of azimuth offset correction estimation (figure 8.2b) and the pattern of the phase derivative (figure 8.2d) confirms the validity of the former, as stated in eq. 2. On the other hand, the comparison of both results, allows us to estimate the proportionality coefficient α (eq. 2) necessary for IPS estimation. We examine both the standard deviations (table 8.I) and the scatter plot on a selected area of track 471 (figure 8.2d).

Considering the linear relation between the two datasets, the α value can be estimated as:

$$\alpha = \frac{std(\Delta x_i)}{std(\frac{\partial}{\partial i}\phi)} = 30.8 \text{ pixels/radian} \quad (4)$$

$\beta = 1/\alpha = 0.032$ rad/pixel

These parameters depend on geometric characteristics of a given sensor in a given mode (Meyer et al., 2006). Therefore, once α and β are estimated on a given radar track/frame, one can use them for correcting other radar frames acquired by the same sensor. This point is of particular importance as we should not compare the interferometric phase derivative with the azimuth offset correction over an area that is affected by a high surface deformation gradient since, in this case, the phase derivative would be affected by surface deformation and the estimation of α would be biased.

Integration of the azimuth correction: the IPS

Now, we calculate the IPS and we correct the differential interferogram on track 473. The IPS is the results of along-orbit integration of the ionospheric contribution to the azimuth offsets (obtained in section III), converted into the phase screen. The conversion from azimuth offsets to the phase screen is obtained by dividing offset values by coefficient α.

$$I_{i,j} = \sum_i \Delta x_{i,j} \quad (5)$$

$$\Delta\Phi_{iono\,i,j} = \frac{1}{\alpha} I_{i,j}$$

Where the I are the results of the integration, x is the ionospheric contribution to azimuth offsets, i and j are line and column indices respectively.

Figure 8.4a shows the extracted ionospheric contribution to the interferometric phase for track 473. In this case study, we can notice that the total ionospheric contribution to the interferometric phase corresponds to ~3.5 radians, which makes ~0.5 interferometric fringes or ~7 cm apparent surface displacement in the LOS direction for PALSAR. For track 471 (figure 8.2e and 8.2f) the IPS undulation is up to ~18 radians (i.e ~3 fringes) equivalent to 34 cm displacement in LOS. Such a phase contribution can severely affect physical interpretations of the earthquake surface deformation based on L-Band interferograms over the mid-to-large scale deformation field, more precisely for wavelengths equal or larger than about 25 km-1. A more detailed study should be carried out to investigate the consequences of the ionosphere on shorter wavelengths.

Figures 2b-2f and 4b-4c compares the differential interferograms before and after correction. We can notice that the total deformation pattern is different. For track 471 we can observe a clear improvement of the interferogram: decreasing of the fringe number and regularisation of the fringe pattern. That would help in the interpretation of the result. However it still remains a large wavelength bias (about 1 fringe) affecting the corrected interferogram (probably due to uncompensated orbital/troposphere errors on the initial interferogram). At this stage, a quantitative validation is difficult to carry out as a dense ground measure network is required on the mapped area (the result being obtained “modulo” a linear ramp, an adjustment of the data has to be carried out prior to the comparison, needing several – more than 4 - points). The GPS coverage on the area is insufficient (Zhang et al., 2008).

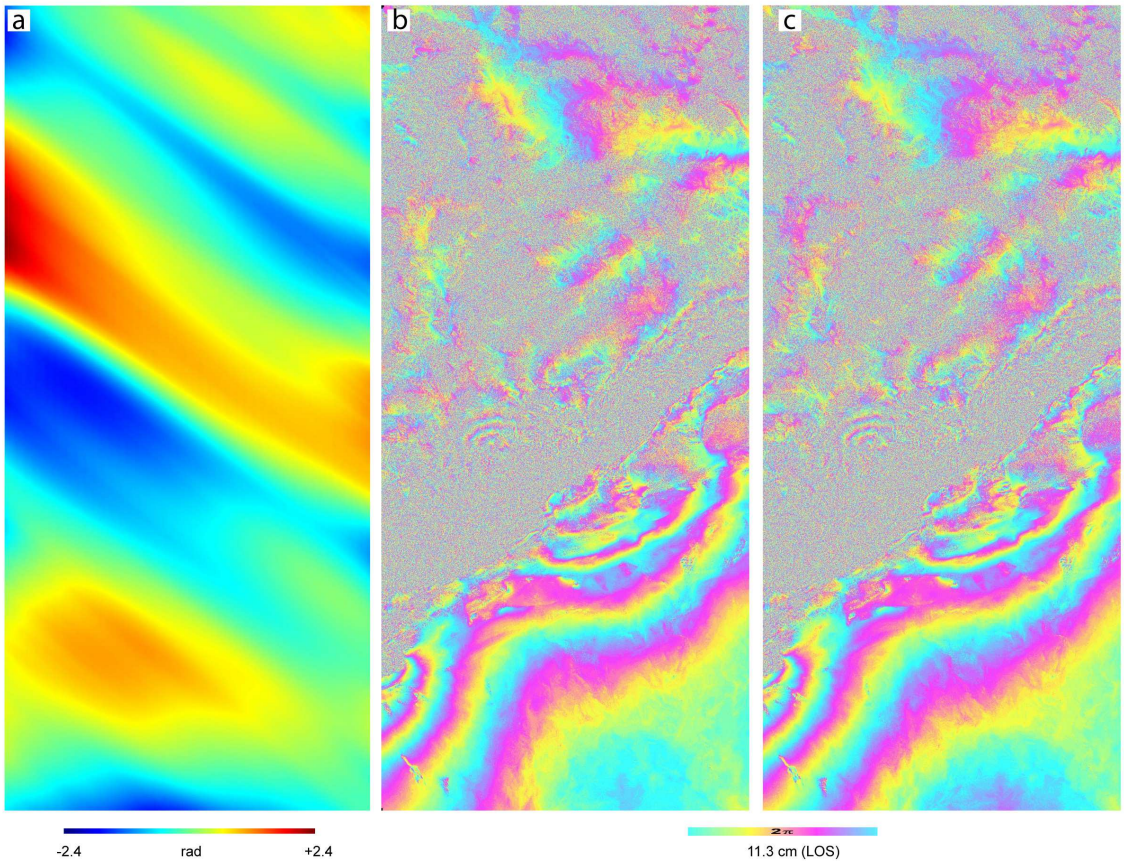

Figure 8.4 a) Ionospheric phase screen for track 473. b) Differential interferogram for Track 473 c) Corrected differential interferogram for track 473.

Discussion

In this case study, the highest co-seismic slip (up to 8 metres) is located within ~15 km of the rupture. Thus we assume that the third-order polynomial used to calculate the ionospheric contribution to the azimuth offsets has a minor influence on the near-field co-seismic displacement values measured by offsets (i.e. close to the rupture).

On the other hand, far-field deformations are usually smaller and of longer wave-lengths. In this case, the ionospheric contribution to the interferometric phase should not be neglected for a correct interpretation of the surface deformation.

Moreover, we have to notice that in another case where deformation field produces long wavelength offsets in the same direction as the azimuth streaks, our methodology might result in an underestimation of the surface displacement as deformation signals would be more difficult to separate from the ionospheric contribution. On the other hand, given the nature of the ionospheric influence on the SAR signal, i.e. it concerns the derivative of the interferometric phase, independent TEC measures (such as by GPS, for instance) might not be adequately dense to resolve the mid wavelength ionospheric derivative and thus they would not be helpful in modelling and removing the ionospheric contribution to the azimuth offsets.

Conclusions

In this paper, we proposed a procedure for extracting ionospheric contributions to the SAR signal and we apply it to improve earthquake measurements based on PALSAR L-band SAR data over the Sichuan earthquake area. We used both sub-pixel correlation of radar amplitude images and radar interferometry. Based on the directionality of the azimuth streaking we defined an adaptive directional filtering method and approximated the ionospheric contribution to the azimuth offset. We then used this estimate to assess and remove the ionospheric contribution to the interferometric phase. The two following observations resulted from the presented study. Firstly, although they were initially severely affected, the azimuth sub-pixel offsets can be used both to precisely map the earthquake rupture and to measure the coseismic displacement in the near field.

Secondly, the ionospheric contribution to the interferometric phase (i.e. the IPS) can reach up to ~15 radians, equivalent to ~28 cm apparent LOS displacement for ALOS PALSAR. This has important implications when using L-band interferometry to model the earthquake cycle. In further works we plan to process all the Sichuan event taking advantage of the inter-track adjustment to correct some residual ramps in order

to produce comprehensive deformation maps (both for near field from image correlation and far field form InSAR) more adapted to such modelling.

Acknowledgement

The authors wish to thank Marie-Pierre Dion (ENS, Paris) for discussions and J. Douglas for helping to improve the document. The data used in this study were provided by the Centre National d'Etudes Spatiales (CNES) through the Cellule d'Intervention et d'Expertise Scientifique et Technique (CIEST) agreement and the International Charter on Space and Major Disasters.

Chapter 9

Three-dimensional surface displacement of the 12 May 2008 Sichuan earthquake (China) derived from Synthetic Aperture Radar: evidence for rupture on a blind thrust.

Marcello de Michele[1], Daniel Raucoules[1], Julia de Sigoyer[2], Manuel Pubellier[2], Nicolas Chamot-Rooke[2]

[1] Bureau de Recherches Géologiques et Minières, Natural Risks Division, Orléans, France.

[2] Ecole Normale Supérieure, Laboratoire de Géologie, Paris, France.

Foreword - The content of this chapter is presently the object of a manuscript accepted for publication to *Geophysical Journal International.* I had the idea to couple data from the ascending orbits L-band PALSAR radar with the descending orbits C-band ASAR radar data along with the radar amplitude correlation technique and Daniel Raucoules actually wrote the inversion program that allowed us to retrieve the 3D displacement field of the Sichuan earthquake. This is a world first on this earthquake and the results are very rich. The colleagues from the *Laboratoire de Géologie* of the *Ecole Normale Supérieure de Paris* helped me with interpretation of the results in terms of tectonics and slip partitioning that led us to the hypothesis of the rupture on a blind thrust. This inter-

pretation benefited from continuous discussions with the CIEST colleagues, particularly Yann Klinger and Jerome van der Woerd. I have to acknowledge the precious help of Pierre Briole with the elastic dislocation modeling.

Summary

The Sichuan earthquake, Mw 7.9, struck the Longmen Shan (LMS) range front, China, on 12 May 2008, affecting an area of moderate historical seismicity where little active shortening has been previously reported. Recent studies based on space geodesy have succeeded in retrieving the far field surface displacements caused by the earthquake, but the near field (± 25 km from the faults) coseismic surface displacement is still poorly constrained. Thus, shallow fault geometry and shallow co-seismic slip are still poorly resolved. Here, for the first time for this earthquake, we combine C and L-band Synthetic Aperture Radar (SAR) offsets data from ascending and descending tracks to invert for the three dimensional surface displacement in the near co-seismic field of the Sichuan earthquake. Our data, coupled with a simple elastic dislocation model, provide new results strongly suggesting the presence of a blind thrust striking along the range front and being active at depth during the earthquake. The presence of a rupture on a blind thrust brings new evidence for an out-of-sequence thrusting event and new elements for interpreting the tectonic strain partitioning in the LMS, which has important implications both for seismic hazard assessment and long-term evolution of the mountain belt.

Introduction

The Longmen Shan (LMS) thrust system bounds the eastern margin of the Tibetan plateau and is considered to be a Triassic transpressive zone that was reactivated during the course of the India-Asia collision (Tapponnier and Molnar, 1977; Chen and Wilson, 1996; Arne et al., 1997; Densmore et al., 2007; Godard et al., 2009). The

LMS front is characterised by a steep topographic gradient displaying a relief of over 5 km within a distance of less than 50 km. Tectonically, the LMS front is a thrust system dominated by three major faults that strike SW-NE (for clarity, we will use nomenclature proposed by Chen and Wilson, 1996); from the inner to the outer range respectively, these are the Wenchuan Fault (WF), the Beichuan Fault (BF) and the Guanxian-Anxian Fault (GF) (Fig. 9.1). The range front displays three principal tectonic units (e.g. Burchfiel et al., 2008; Robert et al., 2010): a crystalline massif composed of Proterozoic basement and Neoproterozoic cover, a narrow foothills area composed of deformed Paleozoic and Mesozoic sediments, and the weakly deformed Sichuan Basin sediments. Recent studies based on thermochronometry across the belt and balanced cross sections indicate that crustal shortening along a thrust system is responsible for the high topography of the region (Godard et al., 2009; Hubbard and Shaw, 2009). This process has mainly affected the BF since 10-8 Ma, without substantial activation of the WF.

The Sichuan earthquake ruptured two parallel thrust faults along the LMS front, generating one of the largest seismic ruptures ever documented in a continental thrust event (Dong et al., 2008). Field campaigns integrated with seismic profiles indicate that at least two imbricate structures (BF, GF) ruptured during the earthquake (e.g. Xu et al., 2009; Liu-Zeng et al., 2009). As corroborated by further data interpretation based on synthetic aperture radar (SAR) amplitude images (Hashimoto et al., 2009; de Michele et al., 2009; Kobayashi et al., 2009), BF ruptured over an ~230 km long segment while GF ruptured over a ~70 km long segment. Field observations indicate that the slip mechanism was a variable combination of thrust and right lateral displacement. However, the three-dimensional rupture geometry and the associated surface motion are difficult to measure in the field due to both the inaccessibility of most of the damaged areas and the rapid erosion of the fault scarps.

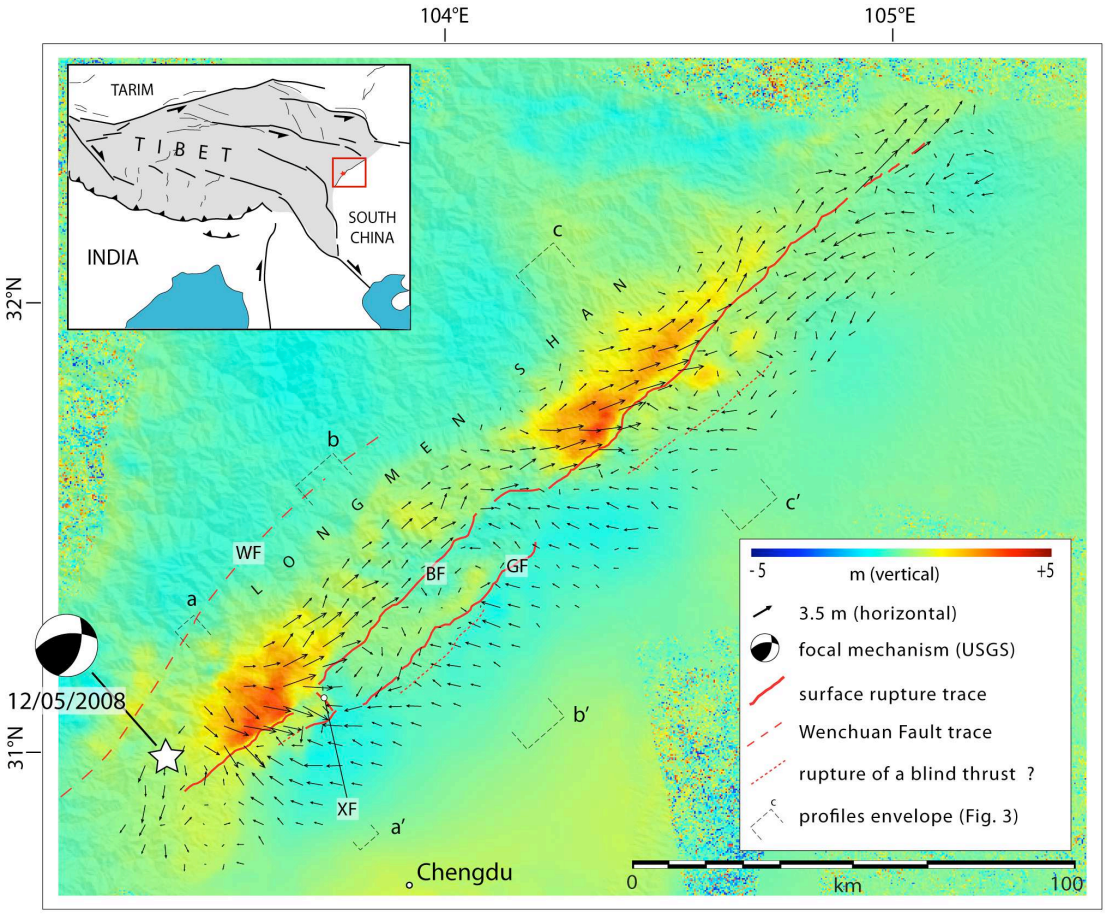

Figure 9.1. Surface displacement distribution of the Sichuan Earthquake, obtained by SPC of radar amplitude images. Vectors: horizontal displacement components. Colours: vertical displacement components. Surface rupture trace (in plain red) after de Michele et al. (2009) and Xu et al. (2009). BF = Beichuan Fault; GF = Guanxian-Anxian Fault; WF = Wenchuan Fault.; XF = Xiaoyudong Tear Fault. The background topography (semi-transparent) is the Digital Elevation Model from the Shuttle Radar Topography Mission. Transect locations are shown; aa', bb', cc' represent the stacked profiles envelope.

A number of teams worldwide, for instance Hashimoto et al. (2009), Shen et al., (2009), Hao et al. (2009), Kobayashi et al. (2009) and Feng et al. (2010), have worked with SAR data to partially overcome the difficulties associated with field data collection. As proposed by Shen et al. (2009), Feng et al. (2009) and Hao et al. (2010), con-

ventional L-band Differential SAR Interferometry (DInSAR) partly overcomes these difficulties by being able to retrieve the surface displacement field from space, in the line-of-sight (LOS) direction of the satellite. Shen et al. (2009) used DInSAR and GPS data to retrieve the longer wavelength surface displacement field, and used it to constrain a model of coseismic slip distribution on the fault plane at depth. The interferometric phase signals decorrelate quickly close to the seismic rupture, mainly due to the high displacement gradient exceeding the theoretical limit of 1/4 of the wavelength per pixel, and the GPS network is too sparse to capture short wavelength surface displacement. Therefore, coseismic surface displacement in the near field is not well resolved. Moreover, ionospheric-related phase delay on the L-band interferograms hampers a unique interpretation of the surface displacement field (Raucoules and de Michele, 2009). Feng et al. (2010) overcame this problem by carefully choosing SAR couples that are less affected by ionospheric-related phase delay (acquired between 68 and 499 days after the quake). This approach does improve the data quality, but the problem of near field interferometric phase signal decorrelation still holds.

Methodology

A SAR system sends radar pulses to the ground and measures both the amplitude and the phase of the backscattered signal. Here we use the radar amplitude data to construct ascending and descending correlograms following the sub-pixel correlation methodology (hereafter named SPC for short) described in Michel et al. (1999), which is today a widely used technique for retrieving co-seismic surface displacements (e.g. Peltzer et al., 2002; Fialko et al., 2005). SPC has already been applied to L-band SAR data over the Sichuan earthquake (Hashimoto et al., 2009; de Michele et al., 2009; Kobayashi et al., 2009), but only with ascending data, therefore yielding a non-unique interpretation of the sense of displacement if one does not have *a priori* information on dip angles and slip mechanisms. Here, we use ascending and descending data. To retrieve the 3D surface displacement in the near field of the earthquake

rupture, we use both L-band SAR data from the Japanese Space Agency Phase Array L-band SAR sensor (PALSAR) onboard the ALOS satellite and C-band SAR data from the European Space Agency Advanced-SAR (ASAR) sensor onboard the ENVISAT satellite (Tables 9.1 and 9.2).

We have used the following approach; we run the sub pixel correlation analysis on the Single Look Complex radar images (SLC) using the correlator implemented in the GAMMA processor (Wegmueller and Werner, 1997). Firstly, we compute the correlograms by using a 64x128 correlation window size. This provides us with a measurement of the surface displacement that is homogeneous over a cell of ~300x400 m for PALSAR and ~500x500 m for ASAR. We arrange the correlator sampling frequency in order to provide an independent measurement every ~64 pixels in the range direction and 128 pixels in the azimuth direction. Secondly, we use the satellite ancillary information to put the correlograms in the original SLC geometry, as specified by the GAMMA correlation procedure (called "offset tracking"). Thirdly, the correlograms are projected in the DEM geometry (orthorectification).

SPC is less precise than conventional DInSAR interferometry but presents several advantages. C and L-band correlograms are negligibly sensitive to tropospheric phase delay and are not limited by high surface displacement gradients. Further, we carefully estimated and reduced the ionospheric contribution to the sub-pixel offset in L-band correlograms using the method described in Raucoules and de Michele (2009).

Each ascending and descending correlogram provides two components of the co-seismic offset field, one in the azimuth direction and one in the LOS direction of the satellite, with a precision of up $1/20^{th}$ of the radar image pixel size (Fig. SM-9.1). Thus, we have 4 non-colinear independent radar observations that we invert to retrieve the east, north and up components of the near field co-seismic surface displacement.

We proceed as follows; let be the unitary vectors associated with the LOS ($u_{r(k)}$) and ($u_{az(k)}$) azimuth directions for each of the 2 acquisitions (ASAR descending and PAL-

SAR ascending). We use the following rule: the LOS values are positive when we move away from the sensor, azimuth value are positive when acquisition time increases. u_r and u_{az} can be easily defined using the incidence angles and the angles between the orbits and the local meridian. We therefore obtain a 4-components data vector:

$$\mathbf{d} = \begin{pmatrix} az_{(1)} \\ az_{(2)} \\ los_{(1)} \\ los_{(2)} \end{pmatrix}$$

az represents the two azimuth offsets and *los* represents the LOS offsets. Subscripts *(1)* and *(2)* refer to the 2 acquisitions.

From the unitary vectors, we can define a matrix A:

$$\mathbf{A} = \begin{pmatrix} \mathbf{u}_{az_1}^t \\ \mathbf{u}_{az_2}^t \\ \mathbf{u}_{r_1}^t \\ \mathbf{u}_{r_2}^t \end{pmatrix}$$

The relation between the obtained 4-components data and the 3-components displacement vector is provided by:

$$\mathbf{d} = \mathbf{A}\,\mathbf{v} \qquad (1)$$

where

$\mathbf{v} = \begin{pmatrix} \mathbf{dx} \\ \mathbf{dy} \\ \mathbf{dz} \end{pmatrix}$ is the displacement vector in north, east, up coordinates.

We therefore use a weighted least squares formulation (e.g. Björk., 1996) to derive the displacement vector from the data.

$$\mathbf{V} = (\mathbf{A}^t \Omega \mathbf{A}) \mathbf{A}^t \Omega \mathbf{d} \qquad (2)$$

Ω is the weight matrix, the weights are the signal-to-noise ratio (SNR) values that we estimate during the correlation procedure. For simplicity, we use a diagonal matrix which elements are the SNR correlation values associated to the offset measurement, which allows taking into account the inhomogeneous quality of the measurement.

PALSAR Track	Date	Mode FBS (LOS 34°)	Pixel size Range/ Azimuth (m)
471	29/02/2008	Ascending	4.68 / 3.15
472	31/05/2008 31/01/2008	Ascending	4.68 / 3.15
473	17/06/2008 17/02/2008	Ascending	4.68 / 3.15
474	19/05/2008 05/04/2008	Ascending	4.68 / 3.15
475	05/06/2008 21/12/2007	Ascending	4.68 / 3.15
476	22/06/2008 08/04/2008 24/05/2008	Ascending	4.68 / 3.15

Table 9.1 PALSAR data acquisition characteristics.

ASAR Track	Date	Mode IS2 (LOS 23°)	Pixel size Range/ Azimuth (m)
18	2006/11/15 2008/05/28	Descending	7.9 / 3.9
247	2007/11/16 2008/08/22	Descending	7.9 / 3.9
290	2008/03/03 2008/06/16	Descending	7.9 / 3.9

Table 9.2. ASAR data acquisition characteristics.

The results are shown in Figure 9.1. We validated our results against field measurements from Xu et al. (2009), finding differences with mean ~0.1 m and standard deviation 0.4 m (Fig. 9.2), thus showing that SAR provides a reliable estimate of the displacement field from space. The 3D surface displacement measurements provide us with a unique data set for this earthquake. In particular, we have overcome the need for a direct reliable measurement of the thrust displacement component at the surface – a parameter that is generally difficult to measure in the field.

Results

We observed that co-seismic displacement along the GF occurred mainly as a thrust movement, whereas the BF underwent more complex motion involving thrusting and

dextral displacement, in agreement with previous field observations (Dong et al., 2008; Xu et al., 2009; Liu-Zeng et al., 2009). Three major trends were clearly identified in the displacement field, highlighting a complex strain partitioning. Firstly, in the epicentral area (S-1), surface displacement on BF was accommodated mostly by an oblique thrust mechanism. Average motion on this segment reached ~3.5 metres vertical, ~3.5 metres horizontal-parallel to the fault strike with the dextral slip mechanism, and ~4.8 metres horizontal-perpendicular to the fault strike (Fig. 9.2). No rupture was observed in the field along the SW segment of GF. Nevertheless, transect profiles aa' (Fig. 9.3) reveal a small but significant thrust movement close to the southwestern prolongation of GF. Secondly, in the area 30 km northeast of the epicentre (S-2), strain is fully partitioned between BF and GF. Here, surface displacement on BF shows an almost purely dextral strike-slip motion reaching up to ~3 m. On GF, surface displacement occurs with an almost pure thrust motion, reaching ~2 m of average vertical displacement and ~2.3 m of average horizontal displacement. This drastic lateral change in the style of motion reflects differential shortening of the thrust sheets. The differential shortening is associated with the reactivation of the Xiaoyudong tear fault (XF, Fig. 9.1), a ~6 km long left-lateral strike-slip boundary between the BF and GF segments. This observation is corroborated by field measurements (Xu et al., 2009; Liu-Zeng et al., 2009). Thirdly, in the NE segments on the BF (S-3, S-3a), surface displacement gradually evolves from oblique thrust motion along S-3, with an average displacement of ~4 m in the vertical and ~3 m in the horizontal, to almost pure dextral strike-slip motion displaying up to ~5 m displacement along S-3a, suggesting an evolution from oblique thrust to almost purely dextral strike slip, consistent with seismological data (Wang et al., 2009).

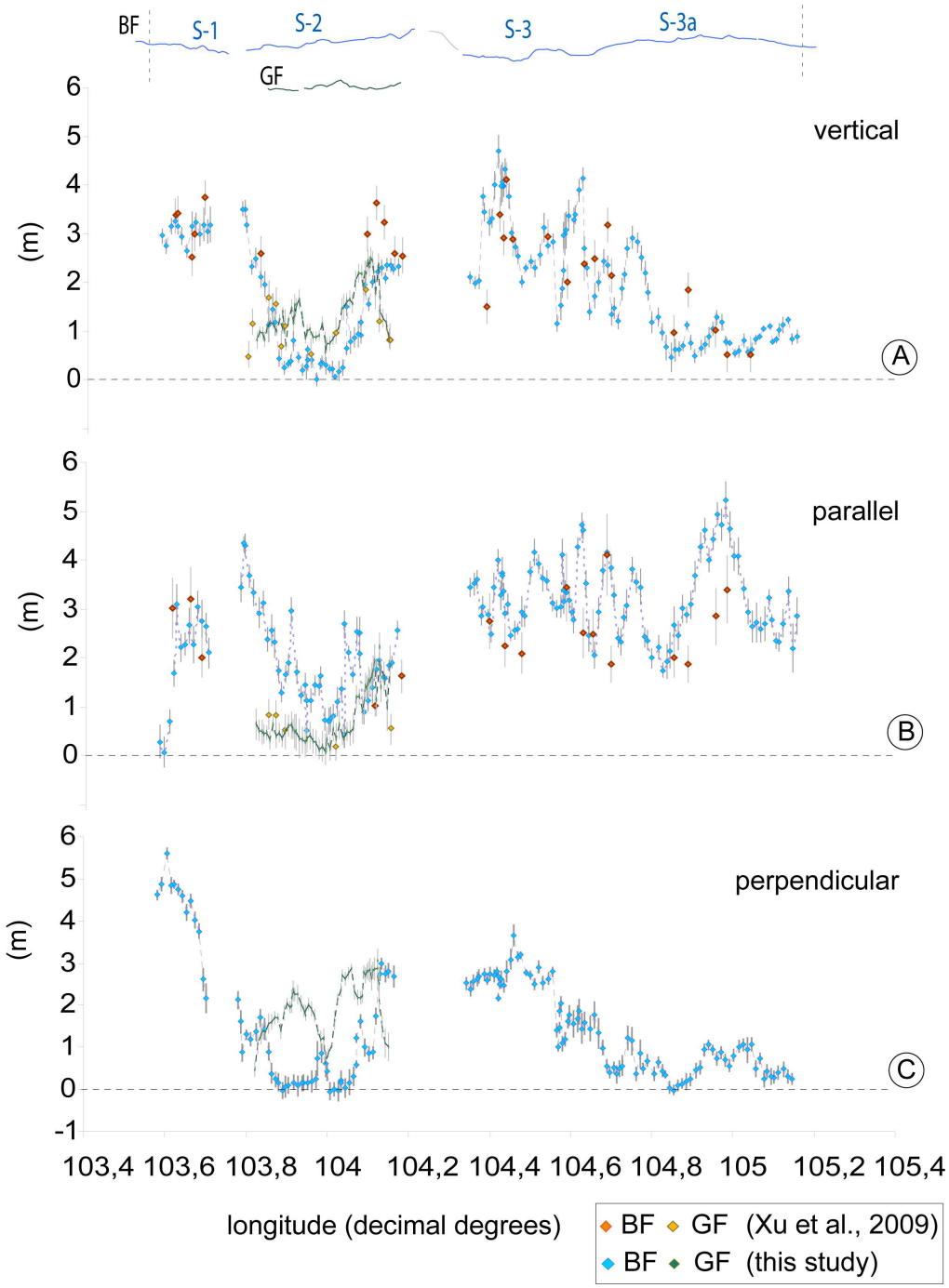

Figure 9.2. Along-fault-strike evolution of the offset on the BF and GF ruptures as measured by SPC, assuming a ~N50E fault strike. Data are sampled every 1 km. a) vertical offset; b) offset parallel to the fault strike; c) offset perpendicular to the fault strike. The latter is often extremely difficult to measure in the field. Orange dots: ground measurements from Xu et al. (2009) that we averaged over 1 km in order to perform a validation of our radar results.

Interpretation and modelling

Firstly, we ask why strain in the LMS system is partitioned between BF and GF in its south-western section and not in its north-eastern section.

While no surface rupture was directly observed in the displacement field along the frontal GF at locations 103°7' and 104°6' (Dong et al., 2008; Xu et al., 2009; Liu-Zeng et al., 2009), our transects in Fig. 3 suggest that a small but significant amount of slip at these locations might have occurred at depth on a structure that was activated by the earthquake. As post-seismic displacement can be substantially ruled-out over the period of observation (Shen et al., 2009), the pattern of displacement in Fig. 3 would be expected for a co-seismic rupture on a blind thrust, possibly at the northern continuation of the GF (Fig. 9.1) and locally on the SE marginal fault (Chen and Wilson, 1996). We verify this hypothesis by comparing the observed data with an elastic dislocation model (Okada, 1985) at the locations of transects aa', bb', cc'. As our SAR results represent near field surface displacement measurements (± 25 km from the faults), we can resolve the upper crust fault slips and geometry (down to ~12 km depth). The aim of the modelling is to answer the question of how the newly acquired data modify our previous knowledge. In other words, we wish to show that slip at depth on the BF and GF only can not fully explain the set of observations. We therefore start the modelling procedure with a forward approach. We used the physical theory of Okada (1985), implemented in the code described by Briole et al. (1986), for predicting the results of observations. We started with a set of *a priori* information on the geometry and slip of the BF and GF. BF and GF geometry was inferred from the structural models of Jia et al. (2009) and Hubbard and Shaw (2009). These models are based on seismic reflection profiles. We also used the mean slip at depth on the BF and GF, as derived in previous works by Hashimoto et al. (2009), Shen et al., (2009), Hao et al. (2009) and Feng et al. (2010) who inverted InSAR, GPS and field measurements. In the second step, we used a trial and error approach to explore the model parameters space and slightly adjust the model parameters to ame-

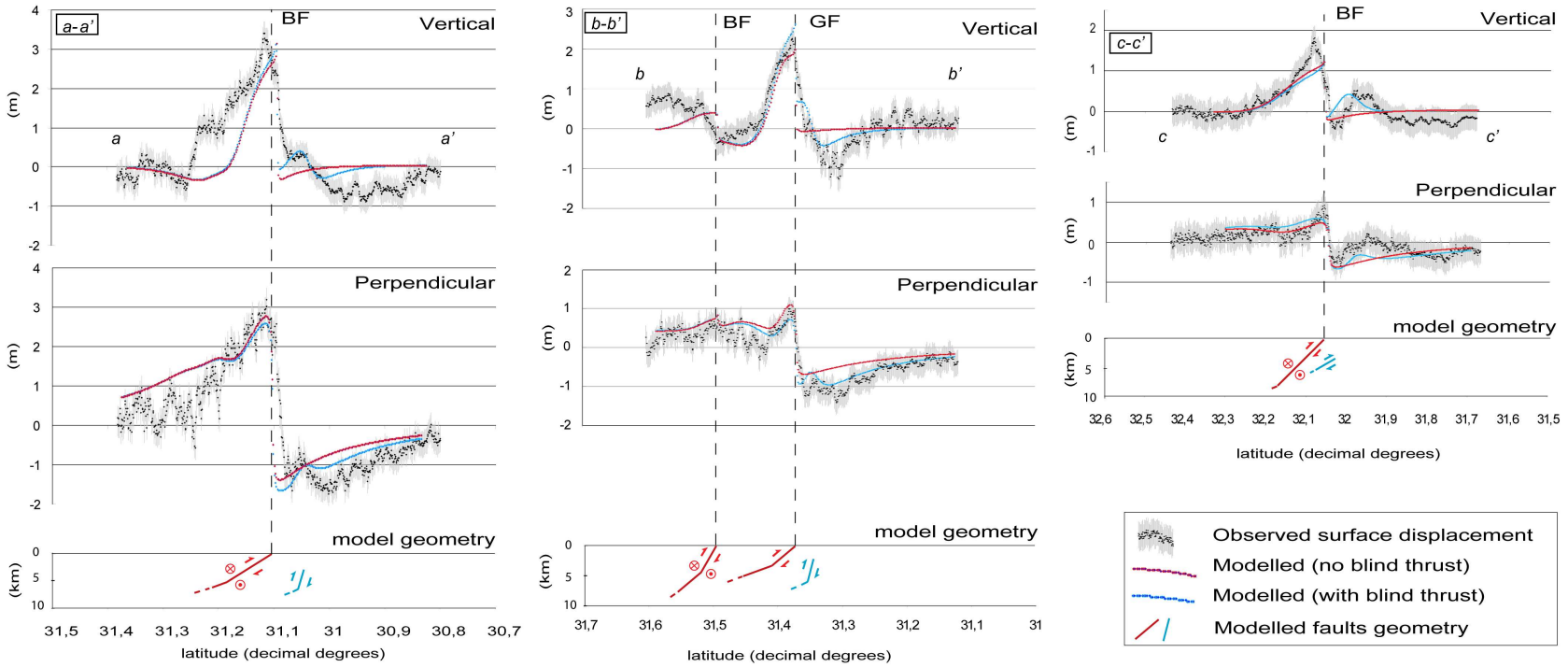

Figure 9.3. Vertical and perpendicular components across-the-strike of the coseismic surface displacement measured at transect locations aa', bb', cc', versus model results from elastic dislocation modelling. Black dots: radar measurements (with uncertainties); red profile: predicted surface displacement without rupture on a blind thrust; blue profile: predicted surface displacement with rupture on a blind thrust. For each transect, we show the model geometry (refer to the text for the model configuration).

liorate the fit to the measurements (Table 9.3). At the end of this step, we noticed that the fit to the data in terms of the basic shape of the profile was unsatisfactory. Therefore, we progressed by falsification (e. g. Tarantola, 2006). We considered the BF and GF geometry to be fixed and introduced a new fault in the model, representing a rupture on a blind thrust. We tested a number of blind fault geometries. For each model, we compared the predictions to actual observations and rejected models with the highest root-mean-square error (RMSE). Generally, we looked for a model configuration whose prediction jointly best-fit both vertical and horizontal surface displacement observations at transect locations (Table 9.3, figure 9.3). The blind thrust model parameter space was sampled following Ellis and Densmore (2006) who used elastic dislocation theory to study the evolution of first order topography in the presence of blind thrusts, and their relation to different parameters such as fault dip, fault depth and amount of slip. Once we were satisfied with the forward model configuration, we considered it fixed and inverted for slip only. The inversion is based on the Tarantola-Valette method (Tarantola and Valette, 1982) implemented in the code inverse5 described by Briole et al. (1986). The inversion was run against two end-member models, with and without blind thrust. We estimated the discrepancy between the model results and the observations by defining an error percentage calculated using the formula described by Battaglia et al. (2005), and also by calculating the RMSE. By adding a buried fault in the dislocation model, the percentage error decreased from 53.8 to 41.7, corresponding to an improvement in the RMSE from 0.43 m to 0.29 m.

Discussion and conclusions

The most striking result is that without adding an additional rupture on a blind thrust on the range front, the observed surface displacement cannot be satisfactorily reproduced (Fig. 9.3). This activated blind structure in the range front in the north-eastern sector possibly coincides with previously mapped Quaternary structures (Chen and Wilson, 1996; Robert et al., 2009; Jia et al., 2009) and may be a north-eastern con-

tinuation of the GF. Modelled slip on the blind thrust reaches 2.7 metres, which is close to the amount of slip found on the GF. Hence, we suggest that where surface displacement evolves from oblique thrust motion to almost pure strike slip on the BF, crustal shortening is accommodated both on the GF in the southwestern sector and on the blind structure at depth in the north-eastern sector. This structural configuration might give rise to the two push-up like structures found in both the epicentral area as well as in the area northeast of Beichuan Town, where vertical displacement reaches a maximum (the two red patches in figure 9.1). In these two areas, strain is not fully partitioned between the BF and the GF. Therefore, transpressional shortening might be accompanied by vertical thickening. Partitioning of transpressional strain can occur when stress is applied oblique to pre-existing structures (e.g. Jones and Tunner, 1995). On a larger picture, we observe that the displacement field recorded during the Sichuan earthquake is compatible with oblique stress applied to inherited ~N50° oriented thrust faults within an overall ENE-WSW compression, as also suggested by the maximum horizontal stress derived from nearby drilling observations in the Sichuan basin (Heidbach et al., 1988) and the work of Liu-Zeng et al. (2009). Although there are certainly blind structures in the Sichuan basin, very little is known about them (e.g. Jia et al., 2009). A good statistical fit does not guarantee a good, or even a reasonable, description of reality. Our model rather represents one solution that can not be disregarded. This solution strengthens the hypothesis of a blind rupture at depth on the range front and provides a new argument in favour of an out-of-sequence thrusting event (Morley, 1988), as first proposed by Liu-Zeng et al. (2009), for the LMS. This result calls for further investigation of the seismic activity on hinterland to marginal thrusts, which have a twofold importance: for understanding the long-term evolution of the mountain belt, and for reassessing seismic hazard in the area.

Segments (aa')	*Dip*	*Length;width (km)*	*Depth of the fault top edge (km) (a)*	*E – N (km) (b)*	*Slip (mm)*
BF (1)	32°	50; 10	0.1	369.437;3441.742	6120 r
BF (2)	20°	50; 3	5.29	361.437;3449.742	2300 r
Bt	70 °	40; 4	2.8	373.837;3437.342	2430 r

Segments (bb')	*Dip*	*Length;width (km)*	*Depth of the fault top edge (km) (a)*	*E – N (km) (b)*	*Slip (mm)*
BF (1)	60°	64; 5	0.2	403.275;3480.488	820 r; 3120 ds
BF (2)	40°	64; 5	4.33	401.507;3482.255	800 r; 3000 ds
GF (1)	40°	40; 5	0.1	411.689;3470.074	2900 r
GF (2)	20°	40; 5	3.21	410.981;3472.781	2500 r
Bt	70°	30; 4	2	414.475;3469.288	2700 r

Segments (cc')	*Dip*	*Length;width (km)*	*Depth of the fault top edge (km) (a)*	*E – N (km) (b)*	*Slip (mm)*
BF (1)	45°	70; 19	0.1	461.566;3543.533	2100 r;2100ds
Bt	30°	50; 6	5.	464.204;3536.441	2300 r

Table 9.3. Elastic dislocation model parameters. (a) vertical depth of the segment top edge; (b) East and North coordinates are in UTM zone 48, and refer to the middle point of the top edge of the fault segment; Bt = Blind thrust; r = reverse motion; ds = dextral strike slip motion.

Acknowledgements

SAR data were provided by JAXA and ESA through the French CIEST agreement (Cellule d'Intervention et d'Expertise Scientifique et Technique) and the International

Charter on Space and Major Disasters. We are thankful to Cecile Lasserre, Yann Klinger and Jerome van der Woerd for constructive comments.

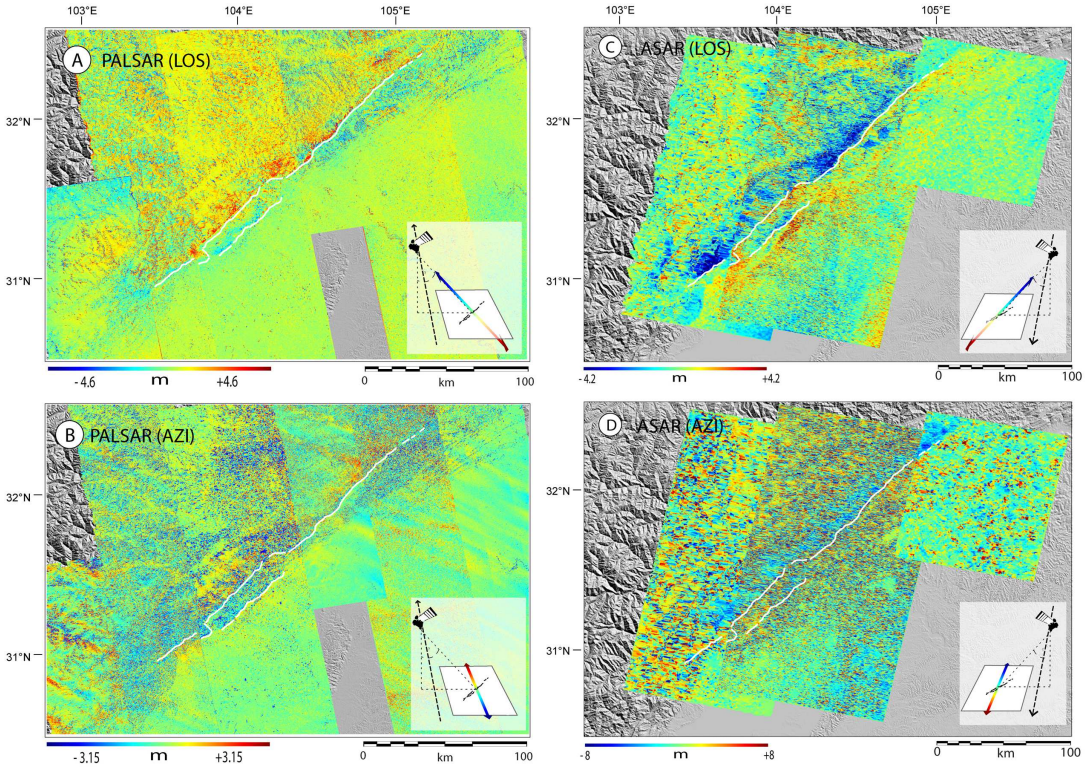

Figure SM-9.1. Correlograms used in the inversion. A) PALSAR LOS SPC offsets, B) PALSAR azimuth offset (after de Michele et al., 2009); C) ASAR LOS offsets, D) ASAR azimuth offset (for the acquisition dates, please refer to Tables 1 and 2 in the text).

Chapter 10

Surface displacement of the Mw 7 Machaze earthquake (Mozambique): Complementary use of 2 multiband InSAR and radar amplitude image correlation with elastic modelling.

Daniel Raucoules[1], Baptiste Ristori[1], Marcello de Michele[1], Pierre Briole[2]

[1] BRGM, 3 avenue Claude Guillemin, 45060 Orléans, cedex 2, France

[2] ENS, Laboratoire de Géologie, 24 Rue Lhomond, 75005 Paris

Foreword - This chapter mainly resumes the work published as Raucoules et al., 2010 on *Remote Sensing of the Environment.* Interestingly, the Machaze earthquake has not been studied a lot before, despite the intriguing seismotectonic context. This is mainly due to the lack of ground instrumentation and the presence of land mines in the region affected by the earthquake, which put into even more evidence the interest of satellite remote sensing techniques for seismotectonic studies in this region. The latter was one of the main motivations of our study. Besides, very soon we discovered the existence of satellite radar data before, during and after the quake, so with this paper it is the first time that an earthquake is studied by different satellite radars, with different wavelength, both in the interseismic, co-seismic and post seismic phase of the earthquake cycle. Daniel Raucoules and me started working on this earthquake with radar data and SPOT5 data (mede available through the CNES ISIS research pro-

gram) in 2007/2008. Then the Sichuan earthquake occurred and I chose to concentrate on it. Daniel Raucoules and Baptiste Ristori carried on the data analysis on the Machaze earthquake, Pierre Briole helped with the elastic dislocation modeling and I manly helped with the tectonic interpretation, in particular with the interpretation and characterization of the post seismic phenomenon.

Summary

In this paper we investigate the surface displacement related to the 2006 Machaze earthquake using Synthetic Aperture Radar Interferometry (InSAR) and sub-pixel correlation (SPC) of radar amplitude images. We focus on surface displacement measurement during three stages of the seismic cycle. First, we examined the co-seismic stage, using an Advanced SAR (ASAR) sensor onboard the Envisat satellite. Then we investigated the post-seismic stage using the Phase Array L-band SAR sensor (PALSAR) onboard the ALOS satellite. Lastly, we focussed on the inter-seismic stage, prior to the earthquake by analysing the L-band JERS-1 SAR data. The high degree of signal decorrelation in the C-band co-seismic interferogram hinders a correct positioning of the surface rupture and correct phase unwrapping. The post-seismic L-band interferograms reveal a time-constant surface displacement, causing subsidence of the surface at a ~ 5 cm/yr rate. This phenomenon continued to affect the close rupture field for at least two years following the earthquake and intrinsically reveals a candidate seismogenic fault trace that we use as a proxy for an inversion against an elastic dislocation model. Prior to the earthquake, the JERS interferograms do not indicate any traces of pre-seismic slip on the sismogenic fault. Therefore, slip after the earthquake is post-seismic, and it was triggered by the Machaze earthquake. This feature represents a prominent post-seismic slip event rarely observed in such a geodynamic context.

Introduction

On February 22, 2006, a Mw 7.0 earthquake occurred in Machaze, Manica Province, Mozambique (Figure 10.1) affecting an area characterised by low-level historical seismicity. This earthquake inflicted little damage on property and individuals, mainly because of the typology and density of housing in the area (i.e. scattered villages with light-weight structures). During the 20th century, three earthquakes with magnitudes larger than 5.0 concerned this area: the first in 1951 and the two others in 1957. They were characterised by shallow slip at depths of less than 20 km (Fenton & Bommer, 2006). The fault system associated with these earthquakes can be related to the southern portion of the East African Rift and belongs to a divergent plate-boundary geodynamic context. The 2006 Machaze earthquake occurred at a depth of 12 km and produced a north-south oriented surface rupture about 30-40 km long with a co-seismic surface slip of up to 2 metres (Fenton & Bommer, 2006). The fault ruptured with a normal mechanism with a 70° west dipping fault plane. Fenton & Bommer (2006) stated that the surface rupture, although visible in the field, could not be followed along its entire length due to the danger posed by buried land mines in the area. Moreover, extensive liquefaction phenomena were associated to this event (Lopez-Querol et al., 2007).

In this paper, we called on remote-sensing satellite data to complement data acquired on the ground to help understand the Machaze earthquake. In particular, we used InSAR (e.g. Massonnet & Feigl, 1998) and SPC (e.g. Michel & Avouac, 2002) techniques along with Envisat-ASAR, JERS-1 and ALOS-PALSAR data to measure the ground surface displacement produced by the Machaze earthquake at different stages of the seismic cycle, i.e. before, during and after the earthquake. Then, we used the co-seismic displacement field to constrain the seismogenic fault geometry at depth by inverting the surface displacement field against a simple elastic dislocation model (Briole et al., 1986).

We proceeded as follow. First, we used the ALOS PALSAR data to produce a post-seismic interferogram revealing the position and surface geometry of the seismogenic

fault (not observable on the co-seismic interferograms because of high deformation rates). Then we looked at the inter-seismic interferograms to detect possible creep or pre-seismic slip on this previously unmapped fault. Finally, we built a co-seismic interferogram and used the retrieved fault surface geometry parameters to constrain the fault's co-seismic slip and geometry at depth by means of an inversion procedure.

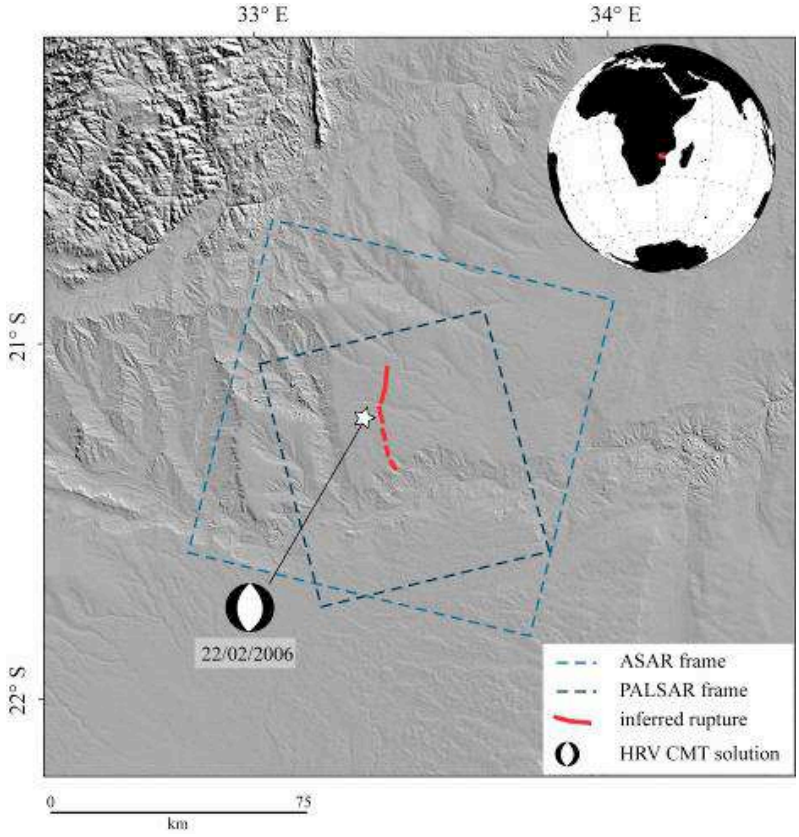

Figure 10.1 : Location of the Machaze Earthquake

Data

In this study, we made a complementary use of C and L band radar from different sensors. Due to the dense vegetation covering the terrain in the area of interest and the large size of surface deformation expected (~2 meters), we decided to use ALOS-

PALSAR and JERS-1 L-band radar data. Moreover, the measurements obtained from radar data at longer wavelengths (23 cm as opposed to 5.6 cm for C-band) would be less affected by fringe aliasing as there would be fewer fringes for given deformation values. Therefore, interferometric phases could be unwrapped over larger areas (e.g. Raucoules et al., 2007). Unfortunately, ALOS and JERS-1 data were not available during the co-seismic phase of the Machaze earthquake. We accordingly called on Envisat/ASAR C-band data to retrieve co-seismic surface displacement while using ALOS-PALSAR and JERS-1 to investigate possible post-seismic and pre-seismic surface displacement respectively. In this study we used six PALSAR images (Dec. 2006- Dec. 2008, ascending mode), seven ASAR images (Nov. 2003, Feb. 2007, descending mode) and three JERS-1 images (Apr. 1993 – Oct. 1996, ascending mode). Tables 10.1 to 10.3 describe the characteristics of the PALSAR, ASAR and JERS-1 interferograms that we built using the GAMMA software (Wegmuller et al., 1998).

Interferogram	Image1 (date)	Image2 (date)	*Perpendicular baseline (m)*	*Time span (days)*
1	20061226	20070210	725	46
2	20061226	20071229	-881	368
3	20061226	20080213	-632	414
4	20061226	20080330	-1191	460
5	20061226	20081231	1512	736
6	20070210	20071229	-1607	322
7	20070210	20080213	-1357	368
8	20070210	20080330	-1916	414
9	20070210	20081231	787	690
10	20071229	20080213	249	46
12	20071229	20081231	2394	368
13	20080213	20080330	-558	46
14	20080213	20081231	2145	322
15	20080330	20081231	2704	276

Table 10.1: Interferograms produced using ALOS PALSAR SAR images. Post-seismic period.

Interferogram	*Image1*	*Image2*	Perpendicular baseline *(m)*	Time span (days)
1	20031109	20060507	720	910
2	20031109	20060611	230	945
3	20031109	20070211	432	1190
4	20040118	20060507	1114	840
5	20040118	20060611	623	875
6	20040118	20070211	826	1120
7	20040328	20060507	-131	770
8	20040328	20060611	-622	805
9	20040328	20070211	-420	1050
10	**20040606**	**20060507**	**-198**	**700**
11	20040606	20060611	-689	735
12	20040606	20070211	-486	980

Table 10.2: Interferograms produced using ASAR Envisat SAR images. Co-seismic period.

Interferogram	Image1	Image2	*Perpendicular baseline (m)*	Time span (days)
1	19930406	19950311	-68	704
2	19930406	19960820	110	1232
3	19950311	19960820	179	528

Table 10.3: Interferograms produced using JER-1 SAR images. Pre-seismic period.

Data Processing

Post-seismic Slip

For each of the three observation periods, we apply different processing strategies.

- Hashimoto et al. (2007) detected and provided a preliminary estimate of the post-seismic deformation phenomenon based on a single ALOS/PALSAR pair prior to December 2006 and examined an Envisat/ASAR pair. Our objective here has therefore been to obtain a precise location of the displacement field and to derive the post-seismic displacement rate over a longer period. We further would be interested in ascertaining whether post seismic displacement is decelerating. In this perspec-

tive, we built a stack of 15 unwrapped interferograms according to the methodology proposed by Le Mouelic et al. (2005):

[eq 1] $$V = \frac{(\Delta\Phi)\frac{\lambda}{2}}{(\Delta T)2\pi}$$

Brackets in eq. 1 indicate the average value on the data set. $\Delta\Phi$ is the interferometric phase, ΔT is the time span associated with an interferogram and λ is the wavelength.

Under such conditions, averaging a series of interferograms reduces the relative importance of the atmospheric component of the interferometric phase as compared with the displacement signal. Considering the characteristics of the studied phenomenon (slow deformation with respect to the sensor wavelength) and the good coherence of the interferograms, unwrapping errors will be reduced and should not impact the velocity map.

Then, based on an optimization procedure, we estimated the velocity by linear regression (Gamma, 2008). The result of this procedure was observed to be equivalent to that obtained by averaging. However, the linear regression procedure allows an image to be achieved of the discrepancy with respect to the linear regression (standard deviation) which provides quality control for the velocity estimation (in particular including temporal fluctuation due to atmospheric effects), and useful information to identify possible non-linear-with-time slip evolution during the observation period. The process accordingly yields a displacement rate map and a map showing discrepancy with respect to linearity (Figures 10.2a, 10.2b).

Inter-seismic Slip

- Our objective for the inter-seismic period was to detect inter-seismic deformation. We therefore constructed interferograms covering long time spans and examined them

near the location of the earthquake rupture. We should mention that the JERS-1 provides poor coverage for this study area (only three images acquired).

Co-seismic Slip

- In order to map the co-seismic surface displacement, we built 12 differential interferograms. After visual comparison of all the interferometric series produced (Table 2), we selected interferograms having the least noise. In view of the high displacement rate (tens of interferometric fringes), the atmospheric component of the interferometric phase is negligible with respect to the displacement component. The results are shown in Figure 10.4.

As direct unwrapping is not relevant (areas with major deformation are not amenable because of the high fringe rate), visible fringes were digitised manually in order to perform an inversion of a dislocation model (Okada, 1985; Briole, 1986). Considering such a model as a direct source of information about the phenomenon, we proposed to re-inject the inverted parameters so as to produce a simulated interferogram. Once the simulated interferogram was subtracted from the initial interferogram, we obtained a residual, which is easier to unwrap. The unwrapped residual was added to the simulated interferograms and provided an improved unwrapped differential interferogram.

It should be stated that the global unwrapping method used by Gamma tends to underestimate phase gradient value where the residual image is noisy. The simulation can therefore help correct these errors. To simplify the principle behind the proposed method, where the phase is noisy, the final result will correspond to the model and where the initial interferogram signal is reliable, the result will correspond to the interferometric data. In a certain way, this procedure interpolates the interferogram on the noisy areas (and in particular in the near-field deformation area) by taking into account a physical model based on the far-field deformation obtained by InSAR and ancillary knowledge about the earthquake.

Results

Post-seismic Slip

Figure 10.2a shows the displacement map derived from PALSAR interferometry. The most prominent feature in the post-seismic displacement map is the constant-with-time subsidence affecting the area formerly ruptured. The RMSE to linearity (Figure 10.2b) shows no correlation between the position of the rupture and the discrepancy with respect to linearity. That suggests that surface displacement is characterised by a constant rate over the 2-year observation period. In fact, the deformation along the rupture appears as linear as on stable areas (where deformation is obviously linear), far from the rupture. We measured a post-seismic surface displacement up to 3.5 cm/year, assuming a mainly vertical displacement phenomenon consistent with a 70°-dip normal fault. This phenomenon affected the study area for at least two years after the earthquake. According to our observations, post-seismic displacement did not decrease with time, though this might be due to the relatively short window of observation. Assuming that the post-seismic displacement occurred on the initial seismic rupture location, we can clearly locate (and digitize) a candidate for the co-seismic surface rupture. At this stage of the processing, one might think that the seismogenic fault underwent pre-seismic slip or creeping. We subsequently assessed the pre-seismic displacement field in the near-fault field and tried to discriminate between post-seismic relaxations and a possible pre-seismic slip component, which in principle should affect the area before the event as well.

Another prominent feature in the post-seismic displacement map is a 5 cm/yr vertical displacement feature located NNW of Figure 10.2. At first sight, this phenomenon is difficult to correlate with the 2006 Machaze earthquake as it is located 10 km west of the main rupture. Although not addressed in detail here, this phenomenon certainly does merit further investigation.

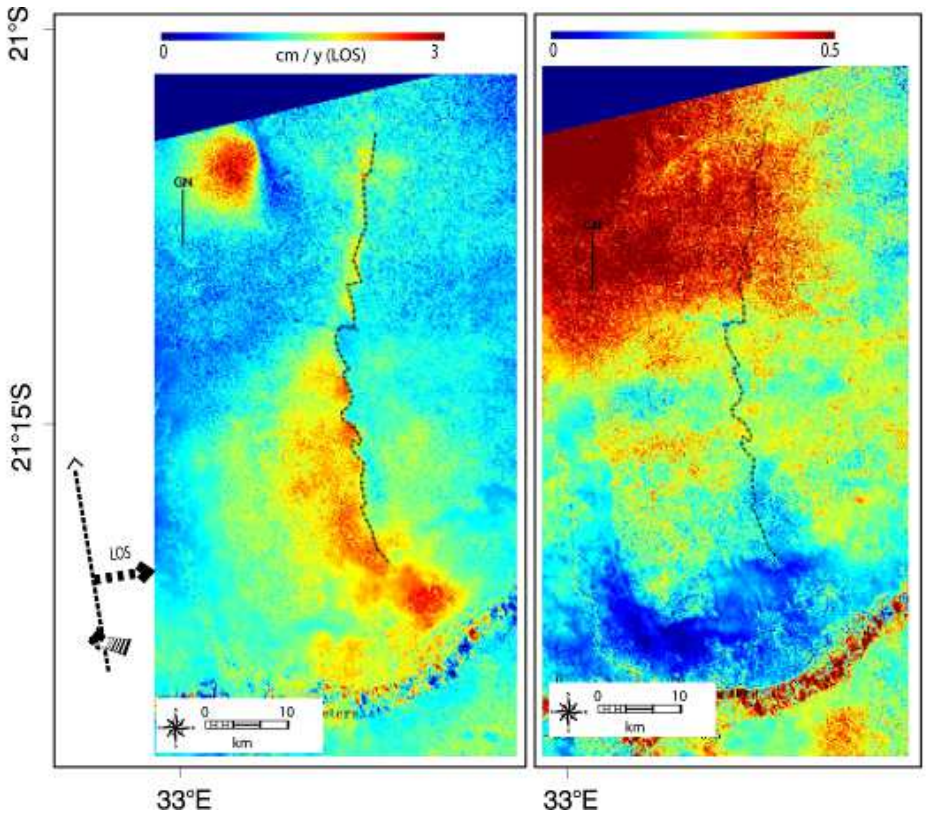

Figure 10.2 a): Average deformation (2006-2008) in Line of sight (cm/year). The surface rupture (dashed line) has been digitised on the image. b): RMSE (rad) of the re-ordered phase screens with respect to linear deformation (root-mean-square residual to the estimated constant rate LOS displacement). No correlation with the rupture position is observable.

Inter-seismic Displacement

Figure 10.3 shows interferograms for the inter-seismic periods 1993-1995 and 1993-1996. No surface displacement phenomena are identified in the vicinity of the seismogenic fault prior to the earthquake. This observation leads us to rule out the presence of measurable pre-seismic slip or creep on this segment of the fault.

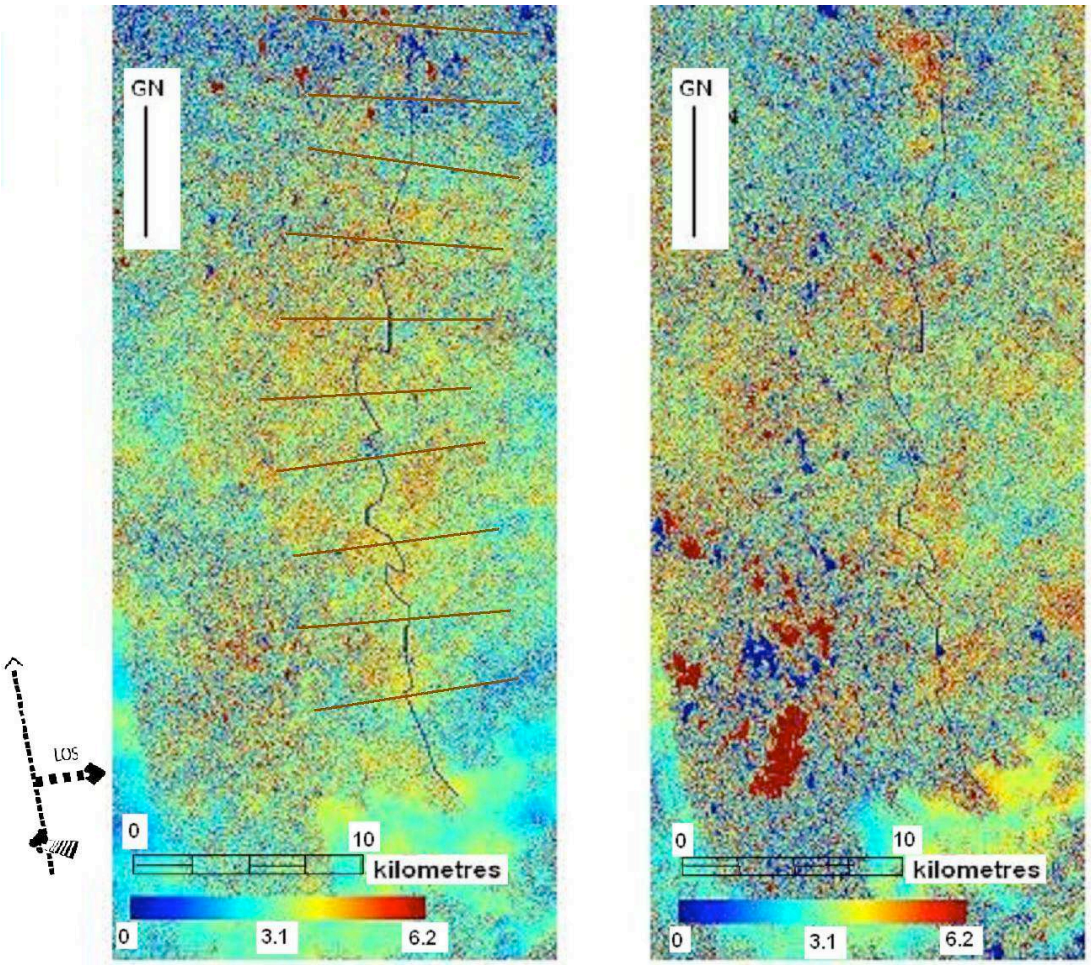

Figure 10.3: a) 1993-1995 JERS-1 interferogram. Black line: the seismogenic fault trace derived from the post-seismic displacement map. b) 1993-1996 JERS-1 interferogram. Values are given in radians. Positions of the ten 10-km profiles used for offset computation (Table 4) have been plotted.

In order to confirm the observation, using a profile tool from the cosi-corr software (Leprince and Ayoub, 2007) designed to estimate deformation-value differences on either side of a fault by comparing linear regressions, we derived the phase values. Table 4 presents the averages of estimations on ten profiles (from north to south) perpendicular to the fault location.

Interferogram 1993-1995		*Interferogram 1993-1996*	
Offset (rad)	Sigma (rad)	Offset (rad)	Sigma (rad)
0.053	0.072	0.100	0.149

Table 4: offset (in rad) on either side of the fault estimated from the interferograms for ten profiles. Sigma corresponds to the standard deviations on the linear regressions on either side of the digitised fault computed by Cosi-corr.

From Table 4 we can conclude:

- For the period 1993-1995, the mean deformation value equals approximately 0.05 rad (i.e. 0.09 cm), with a mean sigma of 0.07 rad (i.e. 0.12 cm)

- For the period 1993-1996, the mean deformation value equals 0.10 rad (i.e 0.2 cm), with a mean sigma of 0.15 (i.e. 0.3 cm)

The values obtained (about 1-3 mm) are very small in terms of the method sensitivity. There is accordingly no pre-seismic motion on the fault that is high enough to be observed with conventional INSAR.

Co-Seismic Deformation

Interferogram 2004/04/06 – 2006/05/07 (Figure 10.4) was selected as the most relevant for interpretation in terms of deformation. This interferogram provides information on the far-field deformation except on the northern area where the coherence is poor (probably because of vegetation). We will note that the deformation phenomenon observed in the post-seismic deformation map is located in the incoherent area. We thus cannot confirm, based on this interferogram, that a rupture did indeed occur at this location.

The near-field deformation is, of course, not measurable because the deformation gradients (metres of displacement on short distances) are far beyond what InSAR is capable of measuring.

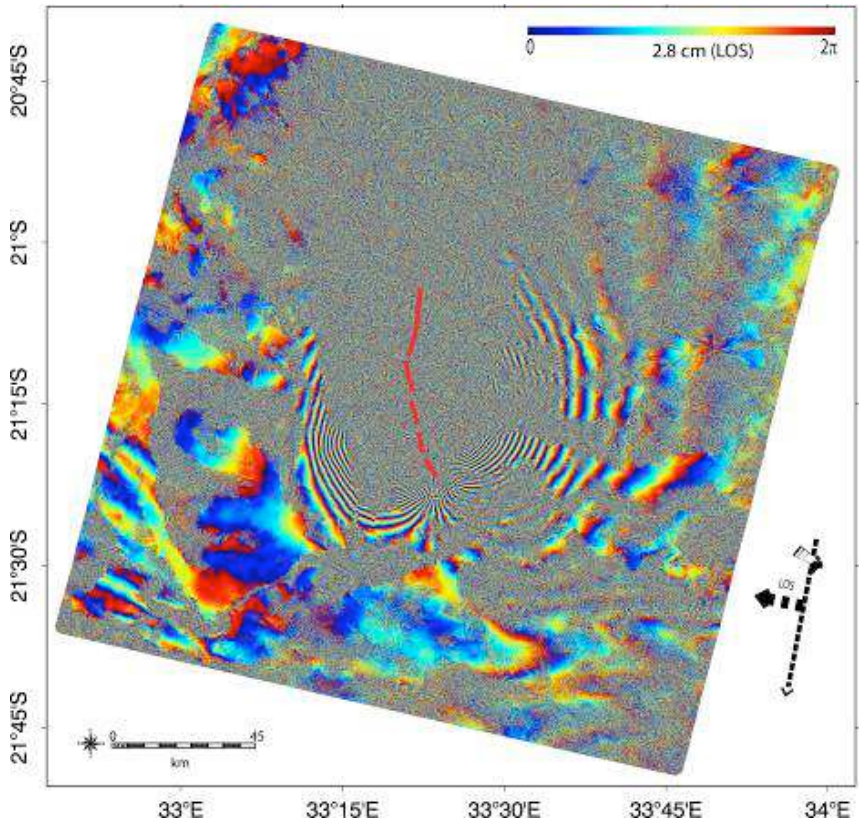

Figure 10.4 geocoded interferogram 2004/04/06 – 2006/05/07. One fringe corresponds to 2.8 cm of displacement in Line of sight. The position of the fault trace at the surface estimated from post-seismic deformation is shown.

Although the precision of image correlation applied to the radar amplitude images (with a slant range resolution of about 7 m) is much poorer than with interferometry, we tested the methodology in order to obtain an estimate of the deformation profile along the fault trace. This information could complement the radar interferometry information where surface displacement is too high (i.e. close to the rupture). Figures

10.5 and 10.6 show the results (offset image and deformation profile) of the correlation. The displacement values on the rupture are determined from linear least square fit to displacement profiles drawn perpendicularly to the rupture. Based on the a priori knowledge of the fault position, this procedure (Avouac et al., 2006; Leprince et al., 2007) fits the deformation profile perpendicularly to the fault by 2 half strait lines on either side of the fault (the profiles are limited by the same point on the fault); the deformation estimate is then provided by the difference between the two fitted values at the fault point location.

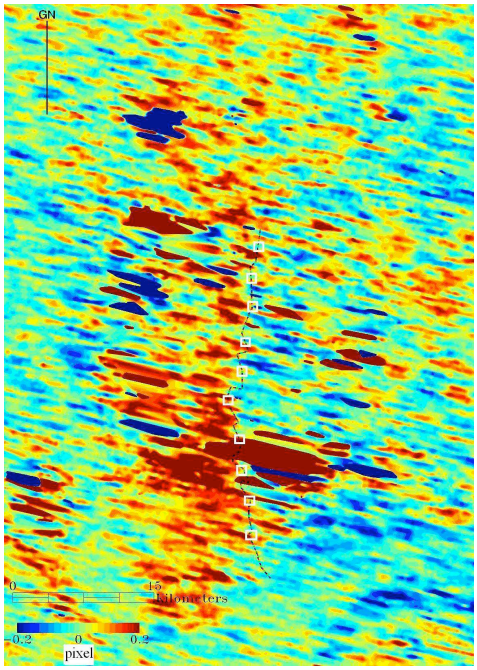

Figure 10.5: Slant range offset (in pixels of about 7 m) between images 2004/04/06 and 2006/05/07. The location of the rupture trace is shown. Squares indicate the location of the points on Figure 6, where offsets have been estimated. Although the result is noisy, the position of the rupture is consistent with the derived displacement variation.

The observed displacement ranges from 1.5 to 2 m in the southern part of the rupture, consistent with Fenton & Bommer (2006) -if we assume that in view of the geometries of the fault (dip >70°) and the sensor (incidence angle ~23°), we are mainly measuring vertical deformation- and 0.7 m to 1.3 m in the northern section, consistent with Hashimoto et al. (2007) who proposed a smaller displacement on the northern segment.

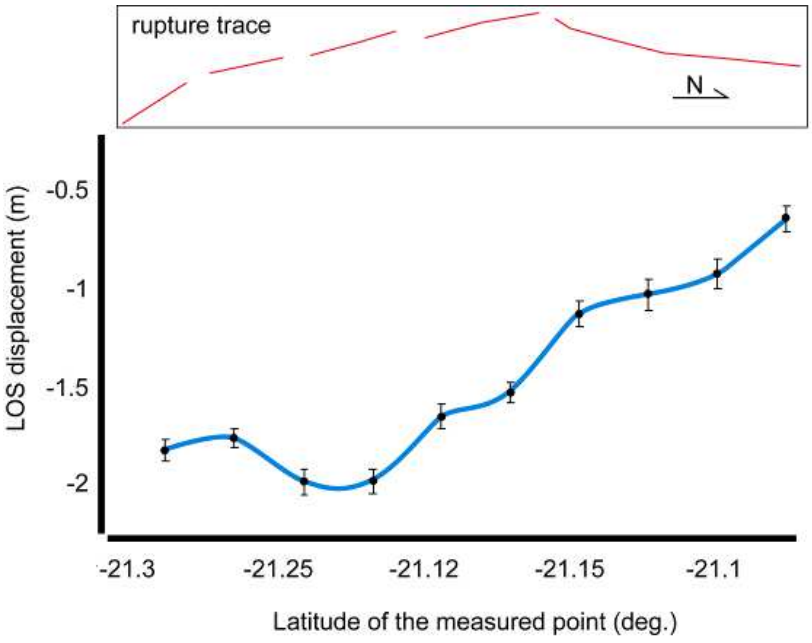

Figure 10.6: LOS displacement on the fault (in metres, east side with respect to west side) versus latitude obtained using the cosi-corr (Leprince and Ayoub, 2007) profile/stacking tool. The error bars correspond to the standard deviation in the linear regressions to either side of the fault.

Azimuth offsets were not used as they are not relevant to our study. Because the deformation is mainly oriented east-west, there are no measurable offsets in the azimuth direction (~ south-north displacements) taking into account the sensitivity of this technique if applied on ENVISAT ASAR data (1/10th of the pixel size, i.e. ~ 40 cm).

Co-seismic deformation modelling

We propose an inversion based on an elastic dislocation model (Okada, 1985; Briole, 1986). Because of the large number of parameters (location, dip, depth, size, displacement for the two fault segments) to be inverted using only one component (Line of sight) of the deformation, we had to use pre-existing information (estimates of the parameters from Feitio, 2008) and trial-and-error adjustments to correct several of the parameters before inverting the slip values. For convenience, we used a rake angle of -90° for both segments (Feitio, 2008, used -80°).

As in Hashimoto et al., (2007) we propose a model with two contiguous fault segments implied in the deformation. However, the position and orientation of the segments are derived from the trace obtained from the post-seismic deformation. Thus, the orientation of the northern segment differs from that proposed by Hashimoto et al., (2007). Table 5 summarizes the resulting parameters. The slip values are consistent with Hashimoto et al., (2007).

Parameter	*Southern segment*	*Northern segment*
UTM 36 S east (km) of the centre of the segment	537	537
UTM 36 S north (km) of the centre of the segment	7647	7667
Segment azimuth (deg)	170	-172
Depth of the top of the segment (km)	5	3
Half length of the segment (km)	10	10
Width of the segment (km)	11	9
Dip (deg)	70	70
Slip (mm)	3400	2660

Table 5: Inverted model parameters.

As described above, the model obtained is suitable for inclusion in a procedure for improving the unwrapping process and interpolating where the interferogram's coherence is inadequate. Figure 10.7 shows the modified interferogram. We should state

that improvement can be expected to be better in the far-field deformation areas (where the model is more reliable, being derived from interferometric data unavailable in the rupture zone). Near the rupture, the result still appears underestimated. For instance, the maximum relative deformation is about 115 cm in LOS (i.e., about 125 cm in vertical) as opposed to 2 m observed by Fenton & Bommer (2006) and Figure 10.7. However, the underestimation is much less than with a direct unwrapping of the interferogram. We think that such interferogram unwrapping (once the area along the rupture has been masked) could be used for inverting a more complex deformation model provided it was combined with additional data. As only one component of deformation is available, if we intend to consider inhomogeneous slips on the fault planes, we would need additional information in order to cope with the non-uniqueness of the solution, in particular other components of deformation and a better description of fault geometry. In fact, in the case of our simple model based on constant slip on two large surfaces combined with basic assumptions on the geometry, we do not believe that re-using these results to improve the model could provide better results than those based on data derived from displacement data obtained by fringe digitizing. To test such a possible "iterative" method (improve the previous model using the corrected interferograms), at least two components of deformation would be required. In the present test case, the available data set does not allow us to go further. Let us note that an additional advantage for such interferogram improvement would be to facilitate interferogram stacking. Indeed, if we had several interferograms for the same event, we would plan to average them in order to reduce noise or atmosphere or compensate for residual biases (not fully compensated). For such stacking procedures, prior unwrapping is needed. Because of the limitations of standard unwrapping with a high deformation gradient and areas of low coherence, such stacking could fail. In this perspective, the described procedure could prove helpful, but unfortunately in our test case only one reliable interferogram was actually produced.

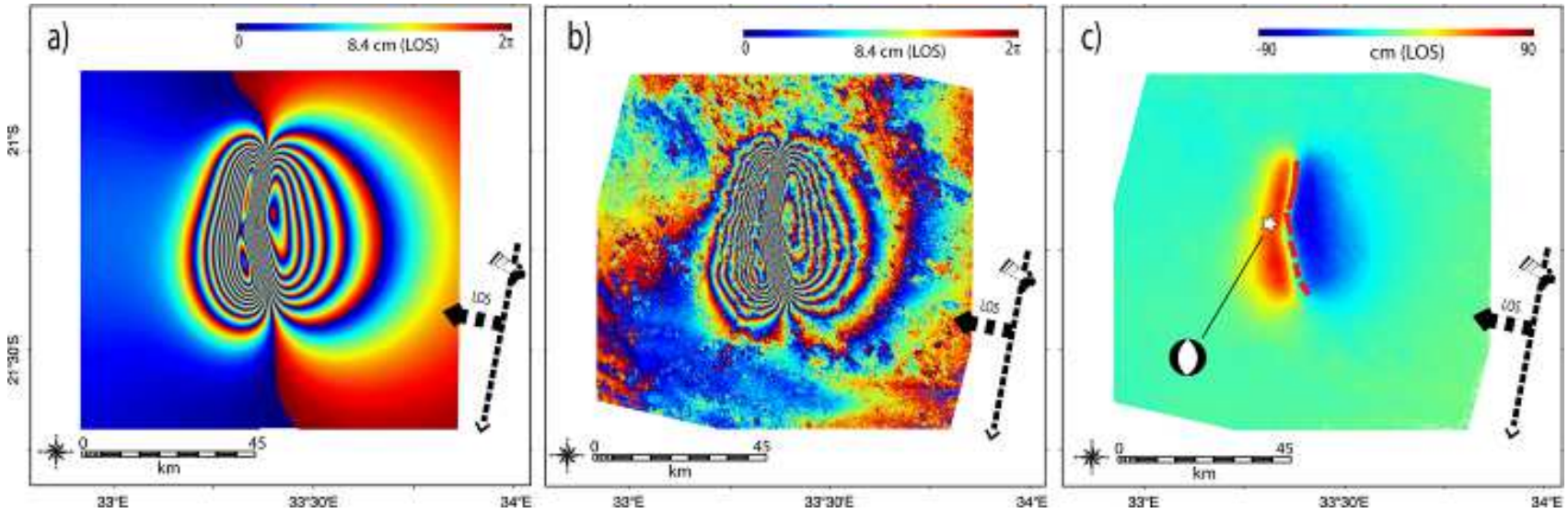

Figure 10.7: a) Interferogram simulation obtained using the inverted parameters. One fringe corresponds to 8.4 cm in LOS. The approximate locations of the modelled fault surfaces are shown. b) Interferogram 2004/04/06 – 2006/05/07 unwrapped taking into account the simulation and rewrapped for visualisation purposes (one fringe corresponds to 8.4 cm in LOS) c) Interferogram 2004/04/06 – 2006/05/07 geocoded and unwrapped taking into account the simulation. Values in rad. The fault trace derived from post-seismic deformation is shown.

Discussion and Conclusion

The results presented in this paper provide new information for understanding surface displacement of the Machaze earthquake in a broad sense.

We have used Satellite-based Radar Interferometry to map surface displacement during three phases (inter, co and post-seismic) of the seismic cycle associated with the 2006 Machaze earthquake. The area affected by the Machaze earthquake is not instrumented on the ground and it is only partially accessible in the field due to the presence of land mines. This makes satellite remote sensing techniques the only tools available to make broad-scale measurements in the area allowing the whole earthquake-induced surface displacement to be observed. We have made use of archive data from both L-band and C-band sensors on board JERS-1, ALOS-PALSAR and ENVISAT-ASAR respectively. The use of J-ERS data drawn from archives to try to enhance possible inter-seismic surface displacements is an interesting aspect of the InSAR technique for such a posteriori studies.

As the surface displacement characteristics during the three phases of the seismic cycle differ in terms of linearity, deformations gradients and localization, we adapted ad hoc processing strategies to the data appertaining to each observation period. In particular, our study started by identifying the location of a candidate surface rupture based on the post-seismic surface displacement location, which completes and complements the surface rupture field observations made by Fenton & Bommer (2006). Interferogram stacking (by averaging) was needed for the post-seismic regime, while for the co-seismic phase we proceeded by visual selection of reliable interferograms from an extensive interferogram series and used a simulation (from an elastic dislocation model) for improving phase unwrapping. Finally, we proposed a new inversion of the earthquake parameters taking into account the identified rupture location.

The post-seismic deformation seems to be constant with time, about 3.5 cm/year for at least the two years after the earthquake. Such a post-seismic phenomenon is intriguing and begs further dedicated investigation. As far as this study is concerned, we

tried to discriminate broadly among different possible known source phenomena such as viscoelastic relaxation (e.g. Thatcher, 1983; Freed, 2007), poroelastic rebound (e.g. Jonsson et al., 2003), afterslip (e.g. Marone et al., 1991) and dilatancy recovery (e.g. Fielding et al., 2009). Although these phenomena might have occurred, we could reasonably rule out substantial contribution from viscoelastic relaxation and poroelastic rebound, as these phenomena would yield a post-seismic signal opposite in direction to the co-seismic signal, which was not the case here. The dilatancy recovery phenomenon was observed geodetically on the BAM strike-slip fault system in Iran (Fielding et al., 2009). Although this phenomenon in not well understood for normal faulting and certainly would deserve more attention for the Machaze case, we might argue that dilatancy recovery would affect a broad zone in the fault area, one not particularly limited by the fault plane, which is not our case. Afterslip occurs when coseismic stress changes drive aseismic slip which is the best candidate in the Machaze area, as afterslip direction is the same as that of the coseismic slip, a fact observed elsewhere (e.g. Freed, 2007).

In further work, we intend to address the following issues about this earthquake that deserve investigation. The post-seismic deformation over a longer period has to be monitored with the objective of detecting deformation slowing (or termination) in order to be able to model for this evolution.

Finally, the deformation observed north-north-west of the epicentre after the earthquake is still unexplained and should be investigated.

Acknowledgements

The study was conducted with the support of the Research Division of BRGM. Parts of the presented study were carried out in the framework of the MSc work of B. Ristori presented at École Nationale des Sciences Géographiques in June 2009. We wish to thank the reviewers for their help in improving the manuscript.

Chapter 11

Conclusions and perspectives

One of the objectives of this PhD thesis is the investigation of potential, limitations, and complementarities of Earth Observation data in addressing some scientific issues related to seismotectonics. We have concentrated our investigations in a limited number of areas of interest such as the San Andreas Fault and the Longmen Shan. We have used ad hoc data processing according to both the aim of each study and to data availability. The data processing that we have performed is mainly based on L-band, C-band Interferometric Synthetic Aperture Radar, subpixel correlation of radar amplitude images and sub-pixel correlation of High Resolution Visible (HRV) satellite images. In most of the cases, we have made use of conventional, commercial or freeware, software packages such as MEDICIS, GAMMA, ENVI-IDL, and COSI-CORR. Although that, in our researches we have tried to involve the development of original approaches to data processing.

Each of the chapters of this manuscript could be seen as an independent study as most of the results presented here have been published independently in international reviews. Each of the studies presented in this manuscript draws its own conclusions. We try here to accomplish the difficult task of making an overall conclusion for this dissertation. We should not talk about "conclusions", but rather "perspectives" as some of our results open more questions than they answer to.

In the present dissertation, mainly two broad topics are discussed;

1) Scientific advances in terms of new approach for data processing and methodological developments;

2) Scientific advances in terms of understanding of neotectonic processes: the surface deformation/displacement field, accommodation and strain partitioning during the interseismic and co-seismic phase of the earthquake cycle on major faults at plate boundaries (i. e. San Andreas Fault) or intra-plate (e. g. the Longmen Shan).

In terms of original methods of data processing, we were among the first teams to think about using airborne pictures to retrieve surface displacement fields. At that time, this technical field was little unexplored. Now, both thanks to the work of Michel and Avouac (2006) and the COSI-corr development team at Caltech (i. e. Ayoub et al., 2009), this method is widely used. We also started addressing the technical question of how to use HRV optical data to retrieve the coseismic displacement field both when a very high resolution DEM does not exist on the study area and when the sensor camera parameters are not provided, which is often the case for Quickbird and IKONOS data distributed free of charge in the frame of the International Charter on Space and Major Disasters. The methodology that we proposed in Chapter 4, based on PCA, need certainly to be further validated and improved. We are planning to go further with this methodology and plan a validation that we will perform in areas where ground truth exists. At the present time, colleagues at the CEA (Commissariat pour l'Energie Atomique, France) are working on a method based on epipolar images to avoid the contribution of topography when calculating the offset field from optical imagery (Renaud Binet, personal communication). We also applied the PCA method to reduce the influence of topography on radar range offsets field on the Sichuan earthquake (Chapter 7). Although of primarily importance, the influence of parallax on radar amplitude offsets is an issue that is not yet clearly addressed in scientific literature. We are planning to go further with this method, identifying limits and sources of noises.

Our best contribution to technical development of InSAR methodology comes from Chapter 8, where we address the question of the ionospheric influence on the L-Band

SAR interferometric phase –referred to as ionospheric delay or ionospheric phase screen. We observed that ionospheric delay affects the measures of the coseismic displacement field in the Sichuan area as high as ~3 PALSAR fringes (~30 cm). This has an impact when trying to model fault displacement and fault geometry at depth starting from InSAR surface displacement field. In Chapter 8, complementing the work of Mattar and Gray (2002), we propose a method (still under development) to reduce the ionospheric influence on the interferometric signal.

The contribution of this dissertation in terms of understanding of neotectonic processes comes mainly from the satellite measurements of surface displacements due to the seismic cycle. Besides, we partly focused on volcanic phenomena that are not related to the seismic cycle (at Piton de la Fournaise, for instance) and on the coupling between high photosynthetic activity and the presence of volcanic vents, which might be a precursory signal for dykes intrusions (Chapter 2). The latter observation should be investigated in further details as it puts into evidence a possible coupling between the solid Earth processes and the biosphere, potentially detectable and measurable by remote sensing. Vegetation response to dykes intrusions by remote sensing should be investigated in volcanic areas related to in immature branches of the East African Rift, for instance during the wet seasons. In addition to volcanic risks assessment, these kinds of analyses have potential for detecting areas of hydrothermal activity and natural resources. The routine monitoring or these processes depends mostly on the data availability in terms of their spatial and temporal resolution.

In terms of contribution to understanding the behaviour of active faults, we provide some results at the end of each related chapter. We concentrated our investigations in different tectonic regimes and in different geographic areas. Therefore, starting from our results, it is not easy to construct a coherent, unique picture of the whole process. I rather try to put in evidence some of our findings.

The work on the SAF is still not yet fully interpreted. Nevertheless, we could try to draw some conclusions. We put into evidence that the Parkfield segment of the SAFZ experienced time-variable creeping phenomena in the period 1993-2004, from epi-

sodic to steady-state creep. We notice that seismic activity at depth is well correlated in space with creep activity at the surface; we do not observe any first order relationship between seismic moment released at depth and the triggering of episodic creep at the surface. An intriguing observation that we put into evidence is a weak signal of episodic creep on the Cholame segment of the SAFZ south of Parkfield, which may trigger debates since it is in contrast with previous published interpretations of GPS and trilateration data. This phenomenon merits to be studied and monitored in more details as this segment of the SAF has been the nucleation point for the great Fort Tejon earthquake in 1857. Besides, have these creeping observations an impact on the recurrence interval of the characteristic Mw 6 Parkfield earthquakes?

On the Bam area, Iran, we put into evidence coseismic slip on a secondary fault (i.e. the Bam-Baravat segment of the Bam Fault), which has not been observed (or given attention to) by conventional InSAR. Apart from the contribution to seismic risk evaluation (as the fault passes in the vicinity of Bam town), our findings contribute to address the question of the shallow slip deficit. We show that coseismic displacement is not only accommodated on the main seismogenic fault but it is also distributed on smaller (probably shallower) fault segments. Even if in a completely different tectonic setting, we find the same scenario in the Longmen Shan: shallow coseismic slip is accommodated on a complex network of fault segments. These shallow fault branches might or might not reach the surface. In the latter case, they give birth to active blind structures as we suggest for the Longmen Shan range front. In the LMS, the active frontal thrust does not propagate deep and far in the foreland basin. This configuration is somehow peculiar for a thrust belt. This is why we join the hypothesis of an “out of sequence thrust” for the LMS and we provide some quantitative elements to support it. The most important clue is the evidence for coseismic rupture on a blind thrust in the range front. It is important to mention that our results on the Sichuan Earthquake contribute to bring quantitative evidences against the previously widely diffused theory of mountain building in the LMS (Royden et al. (1997). This theory referred to as «channel flow» claimed for dynamical sustained topography in

the LMS and diminished the role of earthquakes in mountain building. Despite this, more work need to be done in order to understand the role of catastrophic events such as the the Sichuan earthquake in the process of topography build-up in the LMS.

Orleans, 11 September 2010

Cited Bibliography

Aki, K., Characterization of Barriers on an Earthquake Fault, *J. Geophys. Res.* 84, 6140-6148, 1979.

Allard, J., P. Carbonnelle, D. Dajlevic, J. Le Bronec, P. Morel, M. Robe, J. Marenas, R. Faivre-Pierret, D. Martin, J. Sabroux, P. Zettwoog, Eruptive and diffuse emissions of CO2 from Mount Etna, *Nature*, 351, 387–391, 1991.

Allard, P., Endogenous magma degassing and storage at Mount Etna, *Geophys. Res. Lett*. 24, 2219–2222, 1997.

Allard, P., P. Baxter, M. Halbwachs, J.-C. Komorowski, *Bulletin of the Global Volcanism Network*, Smithsonian Institution, vol. 27, Smithsonian Institution, 2–7, 2002.

Allen, C.R., The tectonic environment of seismically active and inactive areas along the San Andreas fault system, in Dickinson, W. R., and Grantz, Arthur, eds., Proceedings of conference on geologic problems of San Andreas fault system: Stanford, Calif., Stanford University Publications in the Geological Sciences, v. 11, p. 79-80, 1968.

Ambraseys, N., C., Melville, A History of Persian Earthquakes, Cambridge University Press, Cambridge, 1982.

Arne D., B. Worley, C. Wilson, S. F. Chen, D. Foster, Z. L. Luo, S. G. Liu, P. Dirks, Differential exhumation in response to episodic thrusting along the eastern margin of the Tibetan Plateau, *Tectonophysics*, 280, 239-256, 1997.

Ashtiany, M. G., E. Mousavi, History, Geography and Economy of Bam, *Earthquake Spectra*, 21(S1), S3–S11, 2005.

Avallone, A., P. Briole, A. M. Agatz-Balodimou, H. Billiris, O. Charade, C. Mitsakaki, A. Nercessian, K. Papazissi, D. Paradissis G. Veis, Analyses of eleven years of deformation measured by GPS in the Corinth Rift Laboratory area, special issue of *C.R. Acad. Sci*, 336, 301−311, 2004.

Avouac J. P., F. Ayoub, S. Leprince, O. Konca, D. V. Helmberger, The 2005, Mw 7.6 Kashmir earthquake: Sub-pixel correlation of ASTER images and seismic waveforms analysis, *Earth. Planet. Sc.i Lett.*, 249, 514–528, 2006.

Avouac, J.P., P. Tapponnier, Kinematic model of active deformation in central Asia, *Geophys. Res. Let., 20,* 895-898, 1993.

Azzaro, R., M. Mattia, G. Puglisi, Fault creep and kinematics of the eastern segment of the Pernicana fault (Mt. Etna, Italy) derived from geodetic observations and their tectonic significance, *Tectonophysics* 333 (3–4), 401–415, 2001.

Azzaro, R., S. Barbano, M., R. Rigano, S. Vinciguerra, Time seismicity patterns affecting local and regional fault systems in the Etna region; preliminary results for the period 1874–1913, *J. Geol. Soc. Lond.,* 158,561–572, 2001.

Azzaro, R., S. Branca, S. Giammanco, S. Gurrieri, R. Rasà, M. Valenza, New evidence for the form and extent of the Pernicana fault system (Mt. Etna) from structural and soil–gas surveying, *J. Volcanol. Geotherm. Res.,* 84, 143–152, 1998.

Bakun W. H., T. V. McEvilly, Recurrence models and Parkfield, California, Earthquake, *J. Geophys. Res.* 89, B5, 3051-3058, 1984.

Bakun, W. H., Aagaard, B., Dost, B., Ellsworth, W. L., Hardebeck, J. L., Harris, R. A., Ji, C., Johnston, M. J. S., Langbein, J., Lienkaemper, J., J., Michael, A. J., Murray, J. R., Nadeau, R. M., Reasenberg, P. A., Reichle, M. S., Roeloffs, E. A., Shakal, A., Simpson, R. W., Waldhauser, F., Implications for prediction and hazard assessment from the 2004 Parkfield earthquake, *Nature* 437, 969-974, 2005.

Barbot, S., Y. Hamiel, Y. Fialko, Space geodetic investigation of the coseismic and postseismic deformation due to the 2003 M_w7.2 Altai earthquake: Implications for the local lithospheric rheology, *J. Geophys. Res.*, 113, B03403, doi:10.1029/2007JB005063, 2008.

Battaglia, J., K. Aki, V. Ferrazzini, Location of tremor sources and estimation of lava output using tremor source amplitude on the Piton de la Fournaise volcano: 1.

location of tremor sources, *Journal of Volcanology and Geothermal Research*, 147, v. 3-4, p. 268-290, 2005.

Bennett J. H., Fault Creep measurements, *California Geology*, 32, 5, 98-105, 1979.

Berardino, P., G. Fornaro, R. Lanari, E. Sansosti, A new algorithm for surface deformation monitoring based on small baseline differential SAR interferograms. *IEEE Transactions on Geoscience and Remote Sensing*, 40, pp. 2375-2383, 2002.

Berthier, E., H., Vadon, D. Baratoux , A. Arnaud, C. Vincent, K.L. Feigl, F. Rémi, B. Legrésy, Surface motion of mountain glaciers derived from satellite optical imagery, *Remote Sensing of Environment*, 95, 14-28, 2005..

Biggs, J., T. Wright, Z. Lu, B. Parsons. *Geophys. J. Int.* 170, 1165-1179, 2007.

Billi, A., V. Acocella, R. Funiciello, G. Giordano, G. Lanzafame, M. Neri, Mechanisms for ground-surface fracturing and incipient slope failure associated with the 2001 eruption of Mt. Etna, Italy: analysis of ephemeral field data, *J. Volcanol. Geo therm. Res.* 122 (1–2), 281–294, 2003.

Binet, R., Bollinger, L., Horizontal coseismic deformation of the 2003 Bam (Iran) earthquake measured from SPOT-5 THR satellite imagery, *Geophys. Res. Lett.*, 32(2), doi:10.1029/2004GL021897, 2005.

Björck, Å., Numerical methods for least squares problems. SIAM, Philadelphia, 1996.

Branca, S., D. Carbone, F. Greco, Intrusive mechanism of the 2002 Nerift eruption at Mt. Etna (Italy) inferred through continuous microgravity data and volcanological evidences, *Geophys. Res. Lett.* 30 (20), 2077, 2003.

Branca, S., P. Del Carlo, Eruptions of Mt. Etna during the past 3,200 years: a revised compilation integrating the historical and stratigraphic records, Mt. Etna: Volcano Observatory, Geophysical Monograph Series, vol. 143, pp. 1–27, 2004.

Brink, J. L., Patzek, T. W., Silin, D. B., Fielding, E. J., 2002. Lost Hills Field Trial – Incorporating new technology for reservoir management. Paper presented at the SPE Annual Technical Conference and Exhibition, S. Antonio, Texas, 29

September-2 October 2002. Available at http://petroleum.berkeley.edu/papers/patzek/spe77646.pdf.

Briole, P., 1998, SVO (Space Volcanoes Observatory) a proposal in response to ESA AO for Earth Explorer Opportunity Mission, http://pcsgen4.ipgp.jussieu.fr/pb/pro_esa99_svo9.pdf, 2005.

Briole, P., P. Bachelery, B. Mc Guire, J. Moss, J.C. Ruegg, P. Sabourault, 1998. Deformation of Piton de la Fournaise: evolution of the monitoring techniques and knowledge acquired in the last five years, *The European laboratory volcanoes, Proceedings of the second workshop Santorini, Greece 2 to 4 May 1996*, 467-474.

Briole, P., G. De Natale, R. Gaulon, F. Pingue, R. Scarpa, Inversion of geodetic data and seismicity associated with the Friuli earthquake sequence (1976-1977) Italy, *Annales Geophysicae*, 4 B, 481-492, 1986.

Burchfiel, B. C., Z. Chen, Y. Liu, L. H. Royden, Tectonics of the Longmen Shan and adjacent regions, *Int. Geol. Rev.*, 37, 661 – 735, 1995.

Burchfiel, B.C., L. H. Royden, R.D. van der Hilst, B.H. Hager, Z. Chen, R.W. King, C. Li, J. Lü, H. Yao, E. Kirby, A geological and geophysical context for the Wenchuan earthquake of 12 May 2008, Sichuan, People's Republic of China: *GSA Today*, v. 18, p. 4-11, 2008.

Burford, R. O., P. W. Harsh, Slip on the San Andreas Fault in central California from alinement array surveys, *Bull. Seismol. Soc. Am.* 70, 4, 1233-1261, 1980.

Casadevall, T., J. Lockwood, Active volcanoes near Goma, Zaire: hazards to residents and refugees, *Bull. Volcanol.* 57, 275–277, 1995.

Centre National d'Etude Spatiales, 2003. Manuel Utilisateur Medicis, guide book, 56, CNES, Tolouse, France.

Chen, S., C. J. L.Wilson, Q. Deng, X. Zhao, Z. Luo. Active faulting and block movement associated with large earthquakes in the Min Shan and Longmen Mountains, northeastern Tibetan Plateau, *J. Geophys. Res.*, 99, 24,025 – 24,038, 1994.

Chen, S.F., C.J.L. Wilson, Emplacement of the Longmen Shan Thrust-Nappe Belt along the eastern margin of the Tibetan Plateau, *J. Struct. Geol.*, 18, 413-430, 1996.

Costantini M., P. A. Rosen, A generalized phase unwrapping approach for sparse data, Proceedings of IGARSS'99, Hamburg, 28 June-2 July, pp. 267-269, 1999.

Crippen, R. E., Measurements of sub resolution terrain displacements using Spot panchromatic imagery, *Episodes,* 15, 56-61, 1992.

Curtis, P., X. Wang, A meta-analysis of elevated CO2 effects on woody plant mass, form, and physiology, *Oecologia*, 113, 299–313, 1998.

de Michele M., D. Raucoules, H. Aochi, N. Baghdadi, C. Carnec, Measuring coseismic deformation on the northern segment of the Bam-Baravat escarpment associated with the 2003 Bam (Iran) earthquake, by correlation of very-high-resolution satellite imagery, *Geophy. J. Int.*, 173, 2, 459-464, 2008.

de Michele, M., P. Briole, Deformation between 1989 and 1997 at Piton de la Fournaise volcano retrieved from correlation of panchromatic airborne images, Geophys. J. Int., 169, 357–364, doi: 10.1111/j.1365-246X.2006.03307.x, 2007.

de Michele, M., D. Raucoules, C. Lasserre, E. Pathier, Y. Klinger, J. Van Der Woerd, J. de Sigoyer, X. Xu, The Mw 7.9, 12 May 2008 Sichuan earthquake rupture measured by sub-pixel correlation of ALOS PALSAR amplitude images, Earth Planets Space*,* doi:10.5047/eps.2009.05.002, in press (2010).

Delacourt, C., P. Allemand, E. Berthier, D. Raucoules, B. Casson, G. Grandjean, C. Pambrun, E. Varel, Remote-sensing techniques for analysing landslide kinematics: A review; Bull. Soc. Geol. Fr., 178(2), 89-100, 2007.

Delacourt, C., P. Allemand, B. Casson, H. Vadon, Velocity field of « La Clapiere » landslide measured by correlation of aerial and Quickbird satellite images, *Geophys. Res. Lett*, 31, L15619, 2004.

DeMets, C., R.G. Gordon, D.F. Argus, S. Stein, Effect of Recent Revisions to the Geomagnetic Reversal Time Scale on Estimates of Current Plate Motions, *Geophys. Res. Lett*. 21, 2191-2194, 1994.

Densmore, A. L., M. A. Ellis, Y. Li, R. Zhou, G. S. Hancock, N. Richardson, Active tectonics of the Beichuan and Guanxian faults at the eastern margin of the Tibetan Plateau, *Tectonics*, 26, TC4005, doi:10.1029/2006TC001987, 2007.

Doin, M.-P., C. Lasserre, G. Peltzer, O. Cavalié, C. Doubre, Corrections of stratified tropospheric delays in SAR interferometry: Validation with global atmospheric models, Journal of Applied Geophysics, 69, 1, 35-50, 2009.

Dominguez, S., J.P. Avouac, R. Michel, Horizontal coseismic deformation of the 1999 Chi-Chi earthquake measured from SPOT satellite images: implications for the seismic cycle along the western foothills of central Taiwan, *J. Geophys. Res.*, 108, B2 2083 doi:10.1029/2001JB000951, 2003.

Dong, S., Y. Zhang, Z. W.Y. Ma, W. Shi, Z. Chen, C. Long, M. An, Surface rupture and co-seismic displacement produced by the Ms 8.0 Wenchuan earthquake of May 12th, 2008, Sichuan, China: Eastward growth of the Qinghai-Tibet plateau, *Acta Geologica Sinica (English Version)*, 82, 5, 938-948, 2008.

Elliot, J. R., J. Biggs, B. Parsons, T.J. Wright, InSAR slip rate determination on the Altyn Tagh Fault, northern Tibet, in the presence of topographically correlated atmospheric delays, Geophys. Res. Lett. 35, L12309 doi:10.1029/2008GL033659, 2008.

Ellis, M.A., A.L. Densmore, First order topography over blind thrusts, GSA Special Papers January 2006, v. 398, p. 251-266, doi: 10.1130/2006.2398(15), 2006.

Engdahl, E. R., J.A. Jackson, S.C. Myers, E.A. Bergman, K. Priestley, Relocation and assessment of seismicity in the Iran region, Geophys. J. Int. 167, 761–778 doi: 10.1111/j.1365-246X.2006.03127.x, 2006.

ESA, *Recommendations of the Fringe 2007*, Frascati, Italy, 2007, 30/11/2009–4/121/2009. [Online]. Available: http://earth.esa.int/workshops/fringe09/Fringr07_Summaries_Recommendations.pdf

Farr, T. G., E. Caro, R. Crippen, R. Duren, S. Hensley, M. Kobrick, M. Paller, E. Rodriguez, P. Rosen, L. Roth, D. Seal, S. Shaffer, J. Shimada, J. Umland, M.

Werner, M. Oskin, D. Burbank, D. Alsdorf, The Shuttle Radar Topography Mission, v. 45, *Reviews of Geophysics* 45, doi: 1029/2005RG000183, 2004.

Feitio P., Relocation of the Machaze and Lacerda earthquakes in Mozambique and the rupture process of the 2006 M_w 7.0 Machaze earthquake, Master Paper, IISEE, Tsubuka, Japon, (http://iisee.kenken.go.jp), 2008.

Feng, G., E. Hetland, A., Ding, X., Li, Z., Zhang, L., Coseismic fault slip of the 2008 Mw 7.9 Wenchuan earthquake estimated from InSAR and GPS measurements, *Geophys. Res. Lett.*, 37, L01302, doi:10.1029/2009GL041213, 2010.

Femton C., J. Bommer, The M_w 7 Machaze, Mozambique, Earthquake of 23 February 2006, Seismological Research Letters, 77, 426-432, 2006.

Ferretti A., C. Prati, F. Rocca, Permanent scatterers in SAR interferometry, *IEEE Trans. On Geoscience and Remote Sensing*, 39, 1, 8-20, 2001.

Fialko Y., D. Sandwell, M. Simons, P. Rosen, Three dimensional deformation caused bu the Bam, Iran, earthquake and the origin of shallow slip deficit, *Nature*, 435/19, 295-299, 2005.

Fialko, Y., Inter-seismic strain accumulation and the earthquake potential on the southern San Andreas fault system, *Nature,* 44, 968-971, 2006.

Fielding, E. J., R. G. Bloom, R. M. Goldstain, Rapid subsidence over oil fields measured by SAR interferometry, *Geophys. Res. Lett.* 25, 3215-3218, 1998.

Fielding, E.J., P.R. Lundgren, R. Bürgmann, G.J. Funning, Shallow fault-zone dilatancy recovery after the 2003 Bam earthquake in Iran, *Nature*, 458, 64-68, 2009.

Freed, A.M., Afterslip (and only afterslip) following the 2004 Parkfield, California, earthquake, *Geophysical Research Letters*, 34, art. no. L06312, 2007.

Froger, J-L., Y. Fukushima, P. Briole, T. Staudacher, T. Suriot, Villeneuve, N.,. The deformation field of the August 2003 eruption at Piton de la Fournaise, Reunion Island, mapped by ASAR interferometry, *Geophys. Res. Lett.*, 31, L14601, 2004.

Fu, B., X. Lei, K. Hessami , Y. Ninomiya, T. Azuma, H. Kondo, A new fault rupture scenario for the 2003 Mw 6.6 Bam earthquake, SE Iran: Insights from the high-

resolution QuickBird imagery and field observations, Journal of Geodynamics, doi:10.1016/j.jog.2007.02.002, 2007.

Fukushima, Y., V .Cayol, P. Durand, Finding realistic dike models from interferometric synthetic aperture radar data: The February 2000 eruption at Piton de la Fournaise, *J. Geophys. Res.,* 110, B0, 03206, doi: 10.1029/2004JB003268, 2005.

Funning, G.J., B. Parsons, T. J. Wright, E. J. Fielding, J. A. Jackson, Surface displacements and source parameters of the 2003 Bam (Iran) earthquake from Envisat ASAR imagery, *J. Geophys. Res.*, 110(B9), doi:B0940610.1029/2004JB003338, 2005.

Gabriel, A. K., R. M. Goldstein, H. A. Zebker, "Mapping small elevation changes over a large area: Differential radar interferometry,"*J. Geophys. Res.*, vol. 7, no. 2, pp. 183–191, 1989.

Gamma RS, (2008), "IPTA Reference Manual", Gamma RS, Gumligen.

Gan, W., P. Zhang, Z.-K. Shen, Z. Niu, M. Wang, Y. Wan, D. Zhou, J. Cheng, Present-day crustal motion within the Tibetan Plateau inferred from GPS measurements, *J. Geophys. Res.*, 112, B08416, doi:10.1029/2005JB004120, 2007.

Godard V. R. Pik, J. Lavé, R. Cattin, B. Tibari, J. de Sigoyer, M. Pubellier, J. Zhu, Late Cenozoic evolution of the central Longmen Shan, eastern Tibet: Insight from (U-Th)/He thermochronometry, *Tectonics*, v. 28,TC5009, doi:10.1029/2008TC002407, 2009.

Goward, S.N., C. Tucker, D. Dye, North American vegetation patterns observed with the NOAA-7 advanced very high resolution radiometer, *Vegetation,* 64, 3–14, 1985.

Gray, A. L., K. E. Mattar, G. Sofko, Influence of ionospheric electron density fluctuations on satellite radar interferometry, *Geophys. Res. Lett*., 27, 10, 1451-1454, 2000.

Gu, G., T. Lin., Z. Shi, Catalogue of Chinese Earthquakes (1831 B.C. - 1969 A.D.), Science Press, Beijing, China, 1989.

Gudmundsson, A., Emplacement and arrest of sheets and dykes in central volcanoes, *J. Volcanol. Geotherm. Res.* 116, 279–298, 2002.

Gudmundsson, A., I. Ingrid, F. Loetveit, Dyke emplacement in a layered and faulted rift zone, *J. Volcanol. Geotherm. Res.*, Corrected Proof 144, 311–327, 2005.

Gudmundsson, A., Infrastructure and mechanics of volcanic systems in Iceland, *J. Volcanol. Geotherm. Res*. 64, 1–22, 1995.

Hanssen, R. F., Radar Interferometry Data Interpretation and Error Analysis, Remote Sensing and Digital Image Processing Series, Volume 2, Kluwer Academic Publishers, The Netherlands, ISBN 0-7923-6945-9, 2001.

Hao, K.X., H. Si, H. Fujiwara, T. Ozawa, Coseismic surface-ruptures and crustal deformations of the 2008 Wenchuan earthquake Mw7.9, China, *Geophys. Res. Lett.*, 36, L11303, doi:10.1029/2009GL037971, 2009.

Harris R. A., R.J. Archuleta, Slip budget and potential for M7 earthquake in central California, Geophys. Res. Lett., 15, 11, 1215-1218, 1988.

Hashimoto M., Y. Fukushima, T. Ozawa, co-seismic and post-seismic displacements from the Mozambique earthquake of 22 February 2006 detected by InSAR, Fringe07, Frascati, Italy, 26th-30th November 2007, 2007.

Hashimoto, M., M. Enomoto, Y. Fukushima, Coseismic Deformation from the 2008 Wenchuan, China, Earthquake Derived from ALOS/PALSAR Images, Tectonophysics, doi:10.1016/j.tecto.2009.08.034, 2009.

Heidbach, O., K. Fuchs, B. Müller, J. Renecker, B. Sperner, M. Tingay, F. Wenzel, 2005, World stress map, 1/50.000.000, *in* World, C.o.t.G.M.o.t., ed.

Hessami, K., H. Tabassi, K. Okumura, M.R. Abbassi, T. Azuma, Surface Deformation and the Fault Responsible for the 2003 Bam, Iran, Earthquake, *Earthquake Spectra*, 21(S1), S113–S123, 2005.

Hoffman, J., Mapping damage during the Bam (Iran) earthquake using Interferometric coherence, *International Journal of Remote Sensing*, 28(6), 1199-1216, doi:10.1080/01431160600928567, 2007.

Hooper, A. J., Persister Scatterers Radar Interferometry for crustal deformation studies and modeling of volcanic deformation, Ph.D dissertation of the Stanford University (USA), 124 pages, AAT 3219289, ISBN 9780542706905, Nov 2006.

Houlié, N., P. Briole, G. Puglisi, A. Bonforte, Large scale ground deformation of Etna observed by GPS between 1994 and 2001, *Geophys. Res. Lett.* 33 (2), L02309, 2006.

Hu, J., Z. Li, X. Ding, J. Zhu, Two-dimensional co-seismic surface displacements field of the chi–chi earthquake inferred from SAR image matching, *Sensors*, vol. 8, no. 10, pp. 6484–6495, 2008.

Hubbard, J., J.H. Shaw, Uplift of the Longmen Shan and Tibetan plateau and the 2008 Wenchuan (M=7.9) earthquake: Nature, v. 458, p. 194-197, 2009.

INGV, Multidisciplinary approach yields insights into Mt. Etna eruption, *Eos Trans.-Am. Geophys. Union* 82, 653 654, 2001.

Jackson, J., M. Bouchon, E. Fielding, G. Funning, M. Ghorashi, D. Hatzfeld, H. Nazari, B. Parsons, K. Priestley, M. Talebian, M. Tatar, R. Walker, T.J. Wright, Seismotectonic, rupture-process, and earthquake hazard aspects of the 2003 December 26 Bam, Iran, earthquake, Geophys. J. Int., 166, 1270–1292, 2006.

Jia, D., Y.Q. Li, A.M. Lin, M.M. Wang, W. Chen, X.J. Wu, Z.K. Ren, Y. Zhao, L. Luo, 2009, Structural model of 2008 Mw 7.9 Wenchuan earthquake in the rejuvenated Longmen Shan thrust belt, China, *Tectonophysics*, 491, 1-4, 174-184, 2010 .

Johanson, I. A., R. Bürgmann, Creep and quakes on the northern transition zone of the San Andreas fault from GPS and InSAR data, *Geophys. Res. Lett.* 32, L14306, doi:10.1029/2005GL023150, 2005.

Jones R., P.W.G Tunner, Strain partitioning in transpression zones, *Journal of Structural Geology*, v.17, 6, p. 793-802, 1995.

Jónsson, S., P. Segall, R. Pedersen, G. Björnsson, Post-earthquake ground movements correlated to pore-pressure transients, *Nature*, 424 (6945), 179-183, 2003.

Kanamori, H., The energy release in great earthquakes, Journal of Geophysical Research, v. 82, p. 2981-2987, 1977.

King, G. C., J. Nabelek, The role of fault bends in faults in the initiation and termination of earthquake rupture, *Science* **283**, 984-987, 1985.

Klinger Y., R. Michel, G. C. P. King, Evidences for an earthquake barrier model from Mw ~7.8 Kokoxili (Tibet) earthquake slip distribution, *Earth and Planetary Science Letters*, 242 (2006) 354-364, 2006.

Kobayashi, T., Y. Takada, M. Furuya, M. Murakami, Locations and types of ruptures involved in the 2008 Sichuan earthquake inferred from SAR image matching, Geophysical Research Letters, v. 36, 2009.

Kobayashi, T., Y. Takada, M. Furuya, M. Murakami, Ground deformation associated with the 2008 Sichuan earthquake in China, estimated using a SAR offset-tracking method, in *Proc. AGU Fall Meeting*, San Francisco, CA, Dec. 15–19, 2008.

Komorowski, J.-C. , D. Tedesco, M. Kasereka, P. Allard, P. Papale, O. Vaselli, J. Durieux, P. Baxter, M. Halbwachs, M. Akumbe, B. Baluku, P. Briole, M. Ciraba, J.-C. Dupin, O. Etoy, D. Garcin, H. Hamaguchi, N. Houlié, K. Kavotha, A. Lema chand, J. Lockwood, N. Lukaya, G. Mavonga, M. de Michele, S. Mpore, K. Mukambilwa, F. Munyololo, C. Newhall, J. Ruch, M. Yalire, M. Wafula, The January 2002 flank eruption of Nyiragongo Volcano (Democratic Republic of Congo): chronology, evidence for a tectonic rift trigger, and impact of lava flows on the city of Goma, *Acta Volcanol*. Spec. Vol. 14–15, 27–61, 2004.

Komorowski, J.-C., M. Kasereka, M. Ciraba, K. Mukambilwa, F. Munyololo, the Goma Volcano Observatory Research Team, Propagation of lava emissive fractures during the January 2002 Nyiragongo eruption: implications for future activity, IAVCEI International Conference Cities on Volcanoes 3, Hilo, Hawaii, USA, July 14–18, 2003, Abstract Volume, p. 72, 2003.

Komorowski, J.-C., M. Kasereka, M. Ciraba, K. Mukambilwa, M. De Michele, I. Badryo, F. Munyololo, P. Briole, Role of regional tectonics and structural constraints on eruptive style at Nyiragongo Volcano (Democratic Republic of Congo): perm nent lava lake versus flank-fissure eruptions, IAVCEI General Assembly, Pucon Chili, Nov. 14–19, 2004, Abstract Volume, 2004.

Körner, C., R. Asshoff, O. Bignucolo, S. Hättenschwiller, S. Keel, S. Peláez-Riedl, Pepin, R. Siewolf, G. Zotz, Carbon flux and growth in mature deciduous forest trees exposed to elevated CO2, *Science* 309 1360–1362, 2005.

LaDeau, S., J. Clark, Rising CO2 levels and the fecundity of forest trees, *Science*, 292 , 2001.

Lawlor, W., Impact of Global Climatic Changes on Photosynthesis and Plant Productivity, Oxford & IBB Publishing, New Delhi, India, p. 431, 1991.

Le Mouélic S., D. Raucoules, C. Carnec, C. King, A Least-squares adjustment of multitemporal InSAR data – Application to the ground deformation of Paris, *Photogrammetric Engineering and Remote Sensing*, 2, 197-204, 2005.

Le Pichon, X., C. Kreemer, N. Chamot-Rooke, Asymmetry in elastic properties and the evolution of large continental strike-slip faults, *J. Geophys. Res* 110, doi:10.1029/2004JB003343, 2005.

Lenat, J. F., B. G. Malengreau, A. Galdeano, A new model for the evolution of the volcanic island of Reunion (Indian Ocean), *J. Geophys. Res.*, 106, B5 pp. 8645-8663, 2001.

Leprince S., F. Ayoub, Cor-registration of Optically Sensed Images and Correlation, User's Guide to COSI-CORR, California Institute of Technology, Pasadena, 2007.

Leprince, S., S. Barbot, F. Ayoub, J. P. Avouac, Automatic and precise orthorectification, coregistration, and subpixel correlation of satellite images, application to ground deformation measurements, *IEEE Trans. Geosci. Remote Sens.*, *45*, 1529-1558, 2007.

Lienkaemper, J. J., W.H. Prescott, Historic Surface Slip Along the San Andreas Fault Near Parkfield, California, J. Geophys Res. 94, B12, 17,647–17,670, 1989.

Lisowski M., W.H. Prescott, Short range distance measurements along the San Andreas Fault system in central Califirnia, 1975 to 1979, *Bull. Seismol. Soc. Am.* 71, 5, 1607-1624, 1981.

Liu-Zeng, J., Z. Zhang, L. Wen, P. Tapponnier, J. Sun, X. Xing, G. Hu, Q. Xu, L. Zeng, L. Ding, C. Ji, K.W. Hudnut, J.Van der Woerd, Co-seismic ruptures of the 12 May 2008, Ms 8.0 Wenchuan earthquake, Sichuan: East-west crustal shortening on oblique, parallel thrusts along the eastern edge of Tibet, *Earth and Planetary Science Letters*, 286, 355-370, doi:10.1016/j.epsl.2009.07.017, 2009.

López-Querol, S., M. Coop, W.W. Sim, J.J. Bommer, C. Fenton, Back-analysis of liquefaction in the 2006 Mozambique earthquake. *Georisk* 1(2), 89-101, 2007.

Lu, Z., T.J. Wright, C. Wicks, Deformation of the 2002 Denali Fault ertahquakes, Alaska, mapped by Radarsat-1 interferometry, *EOS*, 2003.

Luhr, H., M. Rother, S. Maus, M. Mai, D. Cooke, The diamagnetic effect of the equatorial Appleton anomaly: Its characteristics and impact on geomagnetic field modeling, *Geophys. Res. Lett.*, vol. 30, no. 17, pp. 1906–1910, Sep. 2003.

Lundgren, P., E. A. Hetland, Z. Liu, E.J. Fielding, Southern San Andreas-San Jacinto fault system slip rates estimated from earthquake cycle models constrained by GPS and interferometric synthetic aperture radar observations, *J. Geophys. Res.*, 114, B02403, doi:10.1029/2008JB005996, 2009.

Lundgren, P., S. Usai, E. Sansosti, R. Lanari, M. Tesauro, G, Fornaro, Berardino, P., Modeling surface deformation observed with synthetic aperture radar interferometry at Campi Flegrei caldera, *J. Geophys. Res.*, 106, 19,355-19,366, 2001.

Lyon, S., D. Sandwell, Fault creep along the southern San Andreas from interferometric synthetic aperture radar, permanent scatterers, and stacking, *J. Geophys Res.* 108, B1, 2047, doi:10.1029/2002JB001831, 2003.

Marone, C.J., C.H. Scholtz, R. Bilham, On the mechanics of earthquake afterslip, *Journal of Geophysical Research*, 96 (B5), 8441-8452, 1991.

Massonnet D., P. Briole, A. Arnaud, New insight on Mount Etna from a 18 month radar interferometric monitoring, *Nature*, 375, 567-570, 1995.

Massonnet, D., K.L. Feigl, Radar interferometry and its application to changes in the earth's surface, *Reviews of Geophysics*, 4, 441-500, 1998.

Massonnet, D., M. Rossi, C. Carmona, F. Adragna, G. Peltzer, K. Feigl, T. Rabaute, The displacement field of the Landers earthquake mapped by radar interferometry, *Nature*, 364, 138-142, 1993.

Mattar, K. E., A. L. Gray, Reducing ionospheric electron density errors in satellite radar interferometry applications, *Can. J. Remote Sens.*, vol. 28, no. 4, pp. 593–600, Aug. 2002.

McEvilly T. V., W. H. Bakun, K. B. Casaday, The Parkfield, California, earthquake of 1966, *Bull. Seismol. Soc. Am.* 57, 6, 1221-1244, 1967.

McGee, K., T. Gerlach, R. Kessler, M. Douglas, Geochemical evidence for a magmatic CO2 degassing event at Mammot mountain, California, September–December 1997, *J. Geophys. Res.*, 8447–8456, 2000.

Menke, W., Geophysical Data Analysis: Discrete Inverse Theory, Revised ed, 289, Academic Press, San Diego, 1989.

Merle, O., J. F. Lenat, Hybrid collapse mechanism at Piton de La Fournaise volcano, Reunion Island, Indian Ocean, *J. Geophys. Res.*, 108, B3 2166, doi: 10.1029/2002JB002014, 2003.

Métrich, N., P. Allard, N. Spilliaert, D. Andronico, M. Burton, 2001 flank eruption of the alkali- and volatile-rich primitive basalt responsible for Mount Etna's evolution in the last three decades, Earth Planet. Sci. Lett. 228, 1–2, 2004.

Meyer, F., R. Bamler, N. Jakowski, T. Fritz, “Methods for small scale ionospheric TEC mapping from broadband L-band SAR data,” in *Proc. IGARSS*, Denver, CO, Jul. 31–Aug. 4 2006, pp. 3735–3738.

Michel R., J.P. Avouac, Deformation due to the 17 August 1999 Izmit, Turkey, earthquake measured from SPOT images, *Journal of Geophysical Research* B: Solid Earth, 4, 2-1, 2002.

Michel, R., E. Rignot, Flow of Glaciar Moreno, Argentina, from repeat-pass Shuttle Imaging Radar images: a comparison of the phase correlation method with radar interferometry. *J. Glaciol.* 45, 93-100, 1999.

Michel, R., J. P. Avouac, Coseismic surface deformation from air photos: The Kickapoo step over in the 1992 Landers rupture, *J. Geophys. Res*., 111, B03408, doi: 10.1029/2005JB003776, 2006.

Michel, R., J. P. Avouac, J. Taboury, Measuring ground displacements from SAR amplitude images: Application to the Landers earthquake, *Geophys. Res. Lett.*, vol. 26, no. 7, pp. 875–878, Apr. 1999.

Miller, M., T. Melbourne, D.J. Johnson, D.Q. Sumner, Periodic Slow Earthquakes from the Cascadia Subduction Zone, *Science*, 295, 5564, 2423, 2002

Morley, C.K., Out of Sequence Thrusts, *Tectonics*, v. 7, 3, p. 539–561, 1988.

Murray, J., J. Langbein, Slip on the San Andreas Fault at Parkfield, California, over two earthquake cycles, and the implications for seismic hazard, Bull. Seismol. Soc. Am. 96, 283-303, 2006.

Nakamura, T., S. Suzuki, H. Sadeghi, S.M.F. Aghda, T. Matsushima, Y. Ito, S.K. Hosseini, A.J. Gandomi, M. Maleki, Source fault structure of the 2003 Bam earthquake, southeastern Iran, inferred from the aftershock distribution and its relation to the heavily damaged area: existence of the Arg-e-Bam fault proposed. *Geophys. Res. Lett.*, 32, L09308, doi:10.1029/2005GRL22631, 2004.

Nercessian, A., A. Hirn, J.C. Lepine, M. Sapin, Internal structure of Piton de la Fournaise volcano from seismic wave propagation and earthquake distribution, *J. Volcanol. Geotherm. Res.*, 70, 123-143, 1995.

Okada, Y., Surface deformation due to shear and tensile faults in a half space, *Bull. Seism. Soc. Am.*, 75, 1135-1154, 1985.

Peltzer, G., F. Crampé, P. Rosen, The *Mw* 7.1, Hector Mine, California earthquake: surface rupture, surface displacement field, and fault slip solution from ERS SAR data, *C. R. Acad. Sci.* Paris, v. 333, p. 545–555, 2001.

Perski, Z., R. Hanssen, The interpretation of Bam fault kinematics using Envisat SAR Interferometric data, Proceedings of Fringe 2005 Workshop, ESA, Frascati, Italy, 28 November – 2 December 2005.

Poland, M., Z. Lu, C. Wicks, InSAR observations of surface deformation associated with the 2002 eruption of Nyiragongo Volcano, Africa, IAVCEI International Conference Cities on Volcanoes 3, Hilo, Hawaii, USA, July 14–18, 2003, Abstract Volume, 2003, p. 102.

Powell, R.E., 1993, Balanced palinspastic reconstruction of Pre-Late Cenozoic paleogeology, southern California, in Powell, R.E., Weldon, R.J.,II, and Matti, J.C., eds., in The San Andreas fault system: Displacement, palinspastic reconstruction, and geologic evolution, Geological Society of America, Memoir 178, Chapter 1, p. 1-106.

Puglisi, G., P. Briole, A. Bonforte, Twelve years of ground deformation studies on Mt. Etna volcano based on GPS surveys, in Etna Volcano Laboratory, Geophys. Monogr. Ser., vol. 143, AGU, 321-341, 2004.

Puysségur, B., R. Michel, J.P. Avouac, Tropospheric phase delay in interferometric synthetic aperture radar estimated from metereological model and multispectral imagery, J. Geophys Res. 112, B05419 doi:10.1029/2006JB004352, 2007.

Quegan, S., J. Lamont, Ionospheric and tropospheric effects on synthetic aperture radar performance, *Int. J. Remote Sens.*, vol. 7, no. 4, pp. 525–539, Apr. 1986.

Raucoules D., Colesanti C., Carnec C., Use of SAR interferometry for detecting and assessing ground subsidence, *Compte Rendus Geosciences*, 5, 289-302, 2007.

Raucoules D., M. de Michele, Assessing ionospheric influence on L-band SAR data: Implications on co-seismic displacement measurements of the 2008 Sichuan

Earthquake: *Geoscience and Remote Sensing Letters*,7 , 2, 287-291, DOI10.1109/LGRS.2009.2033317, 2009.

Raucoules, D., C. Maisons V. Carnec, S. Le Mouelic, C. King, S. Hosford, Monitoring of slow ground deformation by ERS radar interferometry on the Vauvert salt mine (France): comparison with ground based measurement, Remote. Sen. Environ., **88**, 468-478, 2003.

Richardson, A.J., C. Wiegand, Distinguishing vegetation from soil background information, *Photogramm. Eng. Remote Sensing* 43, 1541–1552, 1977.

Robert, A., M. Pubellier, J. de Sigoyer, A. Lahfid, R. Cattin, N. Findling, J. Zhu, Structural and thermal characters of the Longmen Shan (Sichuan, China), Tectonophysics, doi:10.1016/j.tecto.2010.03.018, 2010.

Robert, A., J. Zhu, J. Vergne, R. Cattin, G. Wittlinger, L. Chan, J. de Sigoyer, M. Pubellier, L.D. Zhu, Crustal structures in the area of the 2008 Sichuan earthquake from seismologic and gravimetric data, Tectonophysics, doi:10.1016/j.tecto.2009.11.010, 2009.

Robertson, B. C., Rigorous geometric modeling and correction of QuickBird imagery, Proceedings of Geoscience and Remote Sensing Symposium (IGARSS), IEEE International, Tolouse, France, 21-25 July, 2003.

Roeloffs, E., J. Langbein, The earthquake prediction experiment at Parkfield, California, *Rev. Geophys.* 32, 315-336, 1994.

Rosen, P., C. Werner, E. Fielding, S. Hensley, S. Buckley, P. Vincent, Aseismic creep along the San Andreas Fault northwest of Parkfield, CA measured by radar interferometry, *Geophys. Res. Lett.* 25, 825-828, 1988.

Royden, L. H., B. C. Burchfiel, R. W. King, E. Wang, Z. Chen, F. Shen, Y. Liu, Surface deformation and lower crustal flow in eastern Tibet, *Science*, 276, 788 – 790, 1997.

Ruegg, J. C., M. Olcay, D. Lazo, Co-, Post- and Pre-seismic Displacements Associated with the Mw 8.4 Southern Peru Earthquake of 23 June 2001 from Continuous GPS Measurements, *Seismological Research Letters*, 72, 6, 673-678, 2002.

Sarti, F., P. Briole, M. Pirri, Coseismic fault rupture detection and slip measurement by ASAR precise correlation using coherence maximisation. Application to a North-South blind fault in the vicinity of Bam (Iran), *IEEE Geosci. Remote Sens.* Let., doi:10.1109/LGRS.2005.852475, 2006.

Savage, J.C., Principal component analysis of geodetically measured deformation in Long Valley Caldera, eastern California, 1983–1987, *J. Geophys. Res.* 93, 13297–13305, 1988.

Scholz, C. H., *The Mechanics of Earthquakes and Faulting*, Cambridge University Press, London, second edition, 2002.

Schulz S. S., G.M. Mavko, R.O. Burford, W.D. Stuart, Long term fault creep Observations in central California, *J. Geophys. Res*. 87, B8, 6977-6982, 1982.

Shelly D. R, W.L. Ellsworth, T. Ryberg, C. Haberland, G.S. Fuis, J. Murphy, R.M. Nadeau, R. Burgmann, Precise location of San Andreas Fault tremors near Cholame, California using seismometer cluster: Slip on the deep extention of the fault?, *Geophys. Res. Lett.* 36, L01313, doi:10.1029/2008GL036367, 2009.

Shen, Z.-K., J. Sun, P. Zhang, Y. Wan, M. Wang, R. Bürgmann, Y. Zeng, W. Gan, H. Liao, Q. Wang, Slip maxima at fault junctions and rupturing of barriers during the 2008 Wenchuan earthquake, *Nature Geoscience*, doi: 10.1038/NGEO636, 2009.

Sieh K. E., Slip along the San Andreas fault associated with the great 1857 earthquake, *Bull. Seismol. Soc. Am*. 68, 5, 1421-1448, 1979.

Sieh, K. E., R.H. Jahns, Holocene activity of the San Andreas fault at Wallace Creek, California, *Geol. Soc. Am. Bull.*, 95, 883-896, 1984.

Sigmundsson, F., P.D. Durand, D. Massonnet, Opening of an eruptive fissure and seaward displacement at Piton de la Fournaise volcano measured by RADARSAT satellite radar interferometry, *Geophys. Res. Lett.*, 26, 533-536, 1999.

Smith, B. R., D. T. Sandwell, A model for the earthquake cycle along the San Andreas Fault system for the past 1000 years, *J. Geophys. Res.* **111**, Doi :10.1029/2005JB003703, 2006.

Sorey, M., C. Farrar, W. Evans, D. Hill, R. Bailey, I. Hendley, J.W., P. Stauffer, Invisible CO2 gas killing trees at Mammoth Mountain, 1996.

Sorey, W., L. Evans, B. Kennedy, C. Farrar, L. Hainsworth, B. Hausback, Carbon dioxide and helium emissions from a reservoir of magmatic gas beneath Mammoth Mountain, California, *J. Geophys. Res*. 15303–15323, 1998.

Steinbrugge K.V., E.G. Zacher, Creep on the San Andreas Fault, Fault creep and property damage, *Bull. Seismol. Soc. Am.*, 50, 3, 389-396, 1960.

Stone, E. M., L. B. Grant, J.R. Arrowsmith, Recent Rupture History of the San Andreas Fault Southeast of Cholame in the Northern Carrizo Plain, California, *Bulletin of the Seismological Society of America*, Vol. 92, No. 3, pp. 983–997, April 2002, 2002.

Strozzi, T., A. Luckman, T. Murray, U. Wegmuller, C.L. Werner, Glacier motion estimation using SAR offset-tracking procedures, *IEEE Transactions on Geoscience and Remote Sensing*, 40, 11, 2384 - 2391, 2002.

Talebian, M., E.J. Fielding, G.J. Funning, M. Ghorashi, J. Jackson, H. Nazari, B. Parsons, K. Priestley, P.A. Rosen, R. Walker, T.J. Wright, The 2003 Bam (Iran) earthquake rupture of a blind strike slip fault, *Geophys. Res. Lett*., 31(L11), 611 doi:10.1029/2004GL020,058, 2004.

Tapponnier, P., P. Molnar, Active faulting and tectonics in China, *J. Geophys. Res.*, 82, B20, 2905-2930, 1977.

Tarantola, A., Popper, Bayes and the inverse problem, *Nature Physics*, 2, 492-494, 2006.

Tarantola, A., B. Valette, Inverse problems=quest for information, *Journal of Geophysics*, v. 50, p. 159-170, 1982.

Tatar, M., D. Hatzfeld, A.S. Moradi, A. Paul, The 2003 December 26 Bam earthquake (Iran), Mw 6.6, aftershock sequence, *Geophys. J. Int*., 163, 90–105, 2005.

Tazieff, H., An exceptional eruption: Mt. Nyiragongo, January 10th, 1977, *Bull. Volcanol*. 40-3, 1–12, 1977.

Tedesco, D., P. Papale, O. Vaselli, J. Durieux, *Bulletin of the Global Volcanism Network*, Smithsonian Institution, vol. 27, Smithsonian Institution, pp. 2–5, 2002.

Thatcher W., Present-day crustal movements and the mechanics of cyclic deformation, in Wallace, R.E., The San Andreas fault system in California, United States Geological Survey, Professional Paper 1515, Chapter 7 p.189-205, 1990.

Thatcher, W., Nonlinear strain build-up and the earthquake cycle on the San Andreas fault, *Journal of Geophysical Research*, 88 (B7), 5893-5902, 1983.

Tibaldi, A., G. Groppelli, Volcano-tectonic activity along structures of the unstable NE flank of Mt. Etna (Italy) and their possible origin, *J. Volcanol. Geotherm. Res.* 115, 277–302, 2002.

Titus, S. J., C. De Mets, B. Tikoff, Thirty-five-year creep rates for the creeping segment of the San Andreas fault and the effects of the 2004 Parkfield earthquake: Constraints from alignment arrays, continuous global positioning system, and creepmeters, *Bull. Seismol. Soc. Am*. 96, 250-268, 2006.

Tobita, M., M. Murakami, H. Nakagava, H. Yarai, P.A. Rosen, 3-D surface deformation of the 2000 Usu eruption measured by matching of SAR images, *Geophys. Res. Lett.*, 28, 4291-4294, 2001.

Toké, N. A., J.A. Arrowsmith, Reassessment of a slip budget along the Parkfield segment of the San Andreas Fault, *Bull. Seismol. Soc. Am*. 96, 339-348, 2006.

Toutain, J. P., P. Bachelery, P.A. Blum, J.L. Cheminee, H. Delorme, L. Fontaine, P. Kowlawsky, P. Taochy, Real time monitoring of vertical ground deformation during eruptions at Piton de la Fournaise, *Geophys. Res. Lett.,* 20, 553-556, 1992b.

Toutain, J. P., P. Kowlawsky, P. Labazuy, P. Taochy, A. Tessier, A. Pham, J.L. Cheminee, P.A. Blum, J. Zlotnicky, A. Hirn, J. Lepine, Piton de la Fournaise, *Bull. Glob. Volcan. Netw. Smiths. Inst.*, 17, 09, 1992a.

Toutain, J. P., P. Taochy, P. Bachelery, J.L. Cheminee, P.A. Blum, A. Hirn, J. Le Pine, J. Zlotnicky, F. Garner, V. Appora, Piton de la Fournaise., *Bull. Glob. Volcan. Netw. Smiths. Inst.* 16, 07, 1991.

Toutain, J. P., P. Taochy, P. Bachelery, J.L. Cheminee, P. Kowlawsky, A. Mussard, P. Piquemal, P. Mairine, A. Talibart, Piton de la Fournaise, *Bull. Glob. Volcan. Netw. Smiths. Inst*., 15, 02, 1990.

Trembley, I., P. Briole, The 5 meters grid size Digital Elevation Model (DEM) of Piton de la Fournaise summit area; improving resolution and accuracy by image correlation technique and kinematic GPS, *IPGP internal report*, http://geodesie.ipgp.jussieu.fr, 2005.

Usai, S., A least squares database approach for SAR interferometric data. IEEE Transactions on Geoscience and Remote Sensing, 41, pp. 753-760, 2003.

Usai, S., C. Delgaudio, S. Borgstrom, D. Achilli, Monitoring terrain deformations at Phlegrean Fields with SAR interferometry, 2nd International Workshop on SAR Interferometry (FRINGE99), European Space Agency, Liege, Belgium, unpaginated CDROM, 1999.

USGS, http://earthquake.usgs.gov/eqcenter/recenteqsww/Quakes/us2008ryan.php, 2008.

Valentine, D. W., J. N. Densmore, D.L. Galloway, F. Amelung, Use of InSAR to identify land-surface displacement caused by acquifer-system compaction in the Paso Robles area, S. Louis Obispo County, California, March to August 1997 (USGS Open File Rept., 00-447), 2001.

Van Puymbroeck, N., R. Michel, R. Binet, J.P. Avouac, J. Taboury, Measuring earthquakes from optical satellite images, *Applied Optics*, 39, 20 3486-3494, 2000.

Vernant, P., M. Talebian, E.J. Fielding, G.J. Funning, M. Ghorashi, J. Jackson, H. Nazari, B. Parsons, K. Priestley, P.A. Rosen, R. Walker, T.J. Wright, Contemporary Crus-

tal Deformation and Plate Kinematics in Middle East constrained by GPS measurements in Iran and Northern Oman, *Geophys. J. Int.*, 157, 381–398, 2004.

Walker, G.P.L., "Coherent intrusion complexes" in large basaltic volcanoes a new structural model, *J. Volcanol. Geotherm. Res.,* 50 (1–2), 41–54, 1992.

Walker, G.P.L., Intrusive sheet swarms and the identity of crustal layer 3 in Iceland, J. Geol. Soc. (Lond.) 131, 143 161, 1975.

Walker, G.P.L., Volcanic rift zones and their intrusion swarms, J. Volcanol. Geotherm. Res. 94 (1–4), 21–34, 1999.

Walker, R., J. Jackson, Offset and evolution of the Gowk fault, S.E. Iran: a major intracontinental strike-slip system, J. Struct. Geol., 24, 1677–1698, 2002.

Wallace R. E., Extent and pattern of faulting, in Wallace, R.E., The San Andreas fault system in California, United States Geological Survey, Professional Paper 1515, Chapter 1, p. 4, 1990.

Wallace, R.E., Earthquake recurrence intervals on the San Andreas fault, *Bull. Seismol. Soc. Am*., 81, 10, 2875-3889, 1970.

Wang, Z., Y. Fukao, S. Pei, Structural control of rupturing of the Mw7.9 2008 Wenchuan Earthquake, China *Earth and Planetary Science Letters*, 279, 131–138 doi: 10.1016/j.epsl.2008.12.038, 2009.

Wegmuller, U., C. Werner, T. Strozzi, SAR interferometric and differential interferometric processing chain. International Geoscience and Remote Sensing Symposium (IGARSS), 2, 1106-1108, July 1998, Seattle, 1998.

Wegmüller, U., C. L. Werner, GAMMA SAR processor and interferometry Software, Proceedings 3rd ERS Scientific Symposium, Florence, Italy, 17-20 March 1997.

Wegmüller, U., C. L. Werner, M. Santoro, Motion monitoring for Etna using ALOS PALSAR time series, Proceedings of the ALOS PI Symposium, 9-13 Nov, Hawaii, 2009.

Weldon, R. J., T.E. Fumal, G.P. Biasi, K.M. Scharer, Geophysics - Past and future earthquakes on the San Andreas fault, *Science* 308, 966–967, 2005.

Werner, C.L., U. Wegmüller, T. Strozzi, Processing strategies for phase unwrapping for InSAR applications, Proceedings of EUSAR Conference, 04–06 June, Cologne, Germany, unpaginated CDROM, 2002.

Werner, C.,L. U. Wegmuller, T. Strozzi, A. Wiesmann, Precision estimation of local offsets between pairs of SAR SLCs and detected SAR images, Proceedings of the Geoscience and Remote Sensing Symposium (IGARSS), 25-29 July 2005, IEEE International Volume 7, 4803 – 4805, 2005.

Whiting, G.J., D. Bartlett, S. Fan, P. Barkwin, S.S.C. Wofsy, Biosphere/atmosphere CO2 exchange in tundra ecosystems: community characteristics and relationships with multispectral surface reflectance, *J. Geophys. Res.* 97, 16671–16680, 1991.

Whitten C. A., C.N. Claire, Creep on the San Andreas Fault, Analysis of geodetic measurements along the San Andreas Fault, *Bull. Seismol. Soc. Am*. 50, 6, 404-415, 1960.

Xu, X., X. Wen, G. Chen, Q. Tian, J. Chen, Y. Klinger, J. Hubbard, J. H. Shaw, Coseismic reverse- and oblique-slip surface faulting generated by the 2008 Mw 7.9 Wenchuan earthquake, China, *Geology*, 37, 6, 515-518, 2009.

Young, J. J., J.R. Arrowsmith, L. Colini, L.B. Grant, B. Gootee, Three-Dimensional Excavation and Recent Rupture History along the Cholame Segment of the San Andreas Fault, *Bulletin of the Seismological Society of America*, 92, 7, 2670–2688, 2002.

Zebker, H. A., P.A. Rosen, H. Hansley, Atmospheric effects in interferometric synthetic aperture radar surface deformation and topographic maps, J. Geophys. Res. 102, 7547-7563, 1997.

Zhang, Y., W. Gong, J. Zhang, Measuring co-seismic deformation of the Sichuan earthquake by satellite differential INSAR, *Proc. SPIE*, vol. 7285, pp. 728 54F-1–728 54F-8, 2008.